Thesis for The Degree of Doctor of Philosophy

Study of MgB_2 and $YBa_2Cu_3O_{7-x}$ Microbolometers for THz Sensing Applications

Stella Bevilacqua

Terahertz and Millimetre Wave Laboratory
Department of Microtechnology and Nanoscience - MC2
Chalmers University of Technology
Göteborg, Sweden, 2014

Study of MgB_2 and $YBa_2Cu_3O_{7-x}$ Microbolometers for THz Sensing Applications

Stella Bevilacqua

ISBN 978-91-7597-100-1

Doktorsavhandlingar vid Chalmers tekniska högskola
Ny serie nr 3781
ISSN 0346-718X

Technical report MC2-288
ISSN 1652-0769

Terahertz and Millimetre Wave Laboratory
Department of Microtechnology and Nanoscience - MC2
Chalmers University of Technology
SE-412 96 Göteborg, Sweden
Phone: +46 (0) 31 772 1000

Cover: A SEM picture of a bolometer integrated with a spiral antenna fabricated by electron beam lithography, a picture of the YBCO growth, a picture of the bolometer mounted in the detector block and pictures of the detector block and Si lens.

Printed by Chalmers Reproservice
Göteborg, Sweden, November 2014

A Giuseppe e alla mia famiglia

Abstract

In this thesis, two novel THz detectors based on magnesium diboride (MgB_2) and yttrium barium copper oxide ($YBa_2Cu_3O_{7-x}$) are presented. In particular, MgB_2 superconductor is used for the investigation of hot-electron bolometer (HEB) mixers, while $YBa_2Cu_3O_{7-x}$ is explored in microbolometers for room-temperature coherent and incoherent detection.

Superconducting NbN hot electron bolometer (HEB) mixers are widely used in terahertz radio astronomy. HEB mixers are the most sensitive mixers at frequency above 1 THz. However, their drawback is a limited IF bandwidth. Due to the short electron-phonon interaction time, MgB_2 is a promising superconductor for an improved gain bandwidth in HEB mixers.

MgB_2 HEBs integrated with spiral antenna were fabricated, characterised and studied. The gain bandwidth was investigated with respect to the thickness and the critical temperature of the film. A gain bandwidth of 1.3 GHz, 2.3 GHz and 3.4 GHz was measured in 30 nm, 15 nm and 10 nm MgB_2 films, respectively. Using the two temperature model the experimental gain bandwidths data were analysed and, the electron-phonon interaction time, τ_{e-ph} of 7 ps to 15 ps, the phonon escape time, τ_{esc} of 4.8 ps to 42 ps were extracted resulting on the first model for HEB mixers made of MgB_2 films. At 600 GHz and 1.6 THz, the lowest noise temperature was measured to be 800 K and 1150 K at a bath temperature of 4.2 K, respectively. A noise bandwidth as large as 6-7 GHz was measured for HEB mixers fabricated from 10 nm films with a critical temperature of 15 K.

$YBa_2Cu_3O_{7-x}$ microbolometers on bulk substrate integrated with planar antennas were investigated at room-temperature. The highest electrical and optical responsivity was measured to be 230 V/W and 45 V/W at 1 mA bias current while the minimum noise equivalent power was 50 pW/$Hz^{0.5}$. A large variety of bolometers with different areas, geometries, resistances and volumes were studied showing that the noise voltage normalised to the voltage drop over the bolometers was constant and equal to $(V_N/V)^2 = 6\times10^{-11}\times 1/f\times Hz^{-1}$. It is expected that this value can be used as a rule of thumb for the noise estimation of any $YBa_2Cu_3O_{7-x}$ bolometers in the limit of 1/f noise. Heterodyne mixer measurements of $YBa_2Cu_3O_{7-x}$ bolometers showed a response time of 2.5 ns which is the lowest reported among room-temperature bolometers.

Keywords: THz Detectors, HEB, bolometers, Terahertz frequency, MgB_2, $YBa_2Cu_3O_{7-x}$, superconductors, IF bandwidth, noise.

List of publications

Appended papers

This thesis is based on the following papers:

[A] **S. Bevilacqua**, S. Cherednichenko, V. Drakinskiy, J. Stake, H. Shibata and Y.Tokura "Low Noise MgB_2 Terahertz Hot-Electron Bolometer Mixers", in *Applied Physics Letter*, vol.100, no.3, pp.033504, January 2012.

[B] **S. Bevilacqua**, S. Cherednichenko, V. Drakinskiy, H. Shibata, A. Hammar and J. Stake "Investigation of MgB_2 HEB Mixer Gain bandwidth", in *36^{th} IEEE International Conference on Infrared, Millimeter and Terahertz Waves*, Houston, Texas, October 2011.

[C] **S. Bevilacqua**, S. Cherednichenko, V. Drakinskiy, H. Shibata, Y.Tokura and J. Stake "Study of IF Bandwidth of MgB_2 Phonon-Cooled Hot-Electron Bolometer Mixers", in *IEEE Transactions on Terahertz Science and Technology*, vol.3, no.4, pp.409-415, July 2013.

[D] **S. Bevilacqua**, E. Novoselov, S. Cherednichenko, H. Shibata, and Y. Tokura "MgB_2 Hot-Electron Bolometer Mixers at Terahertz Frequencies", accepted for publication in *IEEE Transactions on Applied Superconductivity*, 2014.

[E] S. Cherednichenko, A. Hammar, **S. Bevilacqua**, V. Drakinskiy, J. Stake and Alexey Kalabukhov, "A Room Temperature Bolometer for Terahertz Coherent and Incoherent Detection", *IEEE Transactions on Terahertz Science and Technology*, vol.1, no.2, pp.395-402, November 2011.

[F] **S. Bevilacqua** and S. Cherednichenko, "Fast Room Temperature THz Bolometers", *38^{th} IEEE International Conference on Infrared, Millimeter and Terahertz Waves*, Mainz, Germany, September 2013.

[G] **S. Bevilacqua** and S. Cherednichenko, "Low Noise Nanometer Scale Room-Temperature $YBa_2Cu_3O_{7-x}$ Bolometers for THz Direct Detection", *IEEE Transactions on Terahertz Science and Technology*, vol.4, no.6, pp. 653-660, November 2014.

Other papers and publications

The following papers and publications are not appended to the thesis, either due to contents overlapping with appended papers, or due to contents not related to the thesis.

[a] **S. Bevilacqua** and S. Cherednichenko "High Sensitivity Terahertz Bolometers as Room Temperature Detectors", *39th IEEE International Conference on Infrared, Millimeter and Terahertz Waves*, Tucson, Arizona, 2014.

[b] S. Cherednichenko **S. Bevilacqua** and E. Novoselov "THz Hot Electron Bolometer Mixers", *39th IEEE International Conference on Infrared, Millimeter and Terahertz Waves*, Tucson, Arizona, 2014.

[c] **S. Bevilacqua** and S. Cherednichenko "Room Temperature THz Detectors with Fast Response Rate", *GHz Symposium*, Goteborg, Sweden, 2014.

[d] **S. Bevilacqua**, S. Cherednichenko, V. Drakinskiy, H. Shibata and J. Stake "Submicrometer MgB_2 Hot Electron Bolometer Mixers", *24th International Symposium on Space Terahertz Technology*, Groningen, Netherlands, 2013.

[e] **S. Bevilacqua**, S. Cherednichenko, V. Drakinskiy, H. Shibata and J. Stake "MgB_2 Hot Electron Bolometers for THz radio astronomy", *23th International Symposium on Space Terahertz Technology*, Tokyo, Japan, 2012.

[f] **S. Bevilacqua**, S. Cherednichenko, V. Drakinskiy, H. Shibata and J. Stake "Hot electron bolometer mixers made of MgB_2 films", *GHz Symposium*, Stockholm, Sweden, 2012.

[g] S. Cherednichenko, A. Hammar, **S. Bevilacqua**, V. Drakinskiy and J. Stake "Wideband THz detectors based on YBCO thin films", *6th ESA Workshop on Millimetre-Wave Technology and Applications*, Finland, 2011.

[h] A. Hammar, S. Cherednichenko and **S. Bevilacqua** "YBCO HEB THz mixers," *22th International Symposium on Space Terahertz technology*, Tucson, Arizona, 2011.

[i] A. Hammar, S. Cherednichenko and **S. Bevilacqua** "Terahertz response of YBCO HEB homodyne Detectors", *22th International Symposium on Space Terahertz technology*, Tucson, Arizona, 2011.

[j] A. Hammar, S. Cherednichenko, **S. Bevilacqua**, V. Drakinskiy, and J. Stake "Terahertz Direct Detection in $YBa_2Cu_3O_7$ Microbolometers,", *IEEE Transactions on Terahertz Science and Technology*, vol. 1, no. 2, pp. 390-394, November, 2011.

[k] **S. Bevilacqua**, P. A. Nilsson, K. Andersson, N. Rorsman, J. Grahn and H.Zirath "Characterization of graphene-based field effect transistors," *GHz Symposium*, Lund, Sweden, 2010.

Notations and abbreviations

Notations

A	Area
B	Bandwidth
β	Acoustic phonon transmission coefficient
α	Temperature Coefficient of resistance
c	Speed of light
C	Heat capacity
C_0	Self heating parameter
c_e	Electron specific heat
c_{ph}	Phonon specific heat
c_v	Volumetric specific heat
d	Material thickness
D	Electron diffusivity
Δ	Energy gap
ΔP	Power variation
δ	Misfit
ΔT_C	Superconducting transition width
ΔV	Voltage variation
E	Energy
ε	Dielectric constant
ε_0	Permittivity of vacuum
f	Frequency
f_{3dB}	3 dB roll off frequency
f_{IF}	Intermediate frequency
f_{LO}	Local oscillator frequency
f_n	Noise bandwidth frequency
f_s	Signal frequency
G	Thermal conductance
G_e	Effective Thermal conductance
γ	Electron specific heat coefficient
h	Planck´s constant
η_m	Mixer gain
H_C	Critical magnetic field
J_C	Critical current density
k_B	Boltzmann´s constant

I	Current
I_C	Critical current
L	Lenght of the microbridge
L_{th}	Thermal diffusion length
λ	Wavelength
λ_L	London penetration depth
m	Mass
M	Molar mass
n	Superconducting electron density
n_a	Atomic mass density
ξ	Coherence length
P	Power
P_{IF}	Power of mixer at IF frequency
P_{LO}	Local oscillator power
P_S	Signal power
R	Resistance
R_A	Antenna resistance
R_{bd}	Boundary resistance
R_L	Load Resistance
R_0	Bolometer resistance
ρ	Resistivity
ρ_m	Mass density
T	Temperature
T_B	Bolometer temperature
T_{bath}	Reservoir temperature
T_c	Critical temperature
T_D	Debye temperature
T_e	Electron temperature
T_{IF}	Amplifier noise temperature
T_{ph}	Phonon temperature
T_{rec}	Receiver noise temperature
τ	Mixer time constant
τ_θ	Electron temperature relaxation time
τ_e	Electron cooling time
τ_{e-ph}	Electron phonon interaction time
τ_{esc}	Phonon escape time
τ_{diff}	Diffusion time
τ_{ph-e}	Phonon-electron interaction time
u	Speed of sound
V	Voltage
V_N	Noise voltage
v_F	Fermi velocity
V_{LO}	Voltage amplitude of the local oscillator
V_S	Voltage amplitude of the signal
ω	Angular frequency
ω_{IF}	Intermediate angular frequency
ω_{LO}	Local oscillator angular frequency
ω_S	Signal angular frequency
Z_0	Free space impedance

Abbreviations

Au	Gold
Al_2O_3	Sapphire
BWO	Backward wave oscilaltor
DSB	Double sideband
FET	Field effect transistor
FIB-SEM	Focused ion beam scanning electron microscope
FIR	Far Infrared
GBW	Gain bandwidth
GHz	10^9 Hz
HEB	Hot electron bolometer
HPCVD	Hybrid physical-chemical vapor deposition
IF	Intermediate frequency
InSb	Indium antimonide
LHe	Liquid helium
LN	Liquid nytrogen
LNA	Low noise amplifier
LO	Local oscillator
LSB	Lower sideband
MBE	Molecular beam epitaxy
MgB_2	Magnesium diboride
MgO	Magnesium Oxide
MHz	10^6 Hz
Nb	Niobium
Nb_3Ge	Niobium germanium
NbN	Niobium nitride
NBW	Noise bandwidth
NbTiN	Niobium titanium nitride
NEP	Noise equivalent power
PLD	Pulsed laser deposition
R_V	Responsivity
RF	Radio frequency
SD	Schottky diode
SEM	Scanning electron microscope
Si	Silicon
SiN_x	Silicon Nitride
SIS	Superconductor insulator tunnel junction
$SrTiO_3$	Strontium titanium oxide
SSB	Single sideband
TCR	Temperature coefficient of resistance
THz	10^{12} Hz
Ti	Titamium
USB	Upper sideband
$YBa_2Cu_3O_{7-x}$	Yttrium barium copper oxide

Contents

Chapter 1

Introduction

1.1 THz waves

The electromagnetic spectrum between the microwave (0.1 THz; $\lambda \sim 3\,\mathrm{mm}$) and the Infrared frequencies (10 THz; $\lambda \sim 30\,\mu\mathrm{m}$) is called the terahertz (THz) region [1]. THz waves are applied to numerous fields such as biological, and medical imaging [2], security [3], and communication applications [4] as well as Earth and Space science [5].

THz waves can penetrate through various types of materials such as, paper, plastic, ceramics, wood as well as liquids and gases, therefore can be used for non-destructive and non-invasive analysis of hidden substances and materials. THz spectroscopy is a competitive method for defence and security applications. For medical applications, THz waves are very attractive tool because of the non-ionising radiation (photon energy$\sim$meV) compared to X-Rays (photon energy$\sim$keV). Moreover one of the hopes of the medical community is the early diagnosis of diseases using THz technology. The date rate of wireless communication is less compared to the optical communication in which high data rate has been already achieved. Hence, the realisation of THz information and communication technology could be beneficial for high performance wireless communication, e.g. communication between different buildings, communication in urban areas, etc.

One-half of the total luminosity of the Universe and 98% of the photons emitted since the Big Bang fall into the terahertz range [1,5]. The exploration of the THz range leads to important information about development of galaxies, star formation and origin of the chemical elements in Space. Furthermore, THz radiation is used to explore the atmospheres of comets and planets as well as the cosmic background radiation originating in the "early years" after the Big Bang. Figure 1.1 shows the radiated energy versus wavelength from a typical star forming cloud in the galaxy [5]. Dust is also transparent at longer wavelengths therefore, in far-infrared (THz) one can see deeper into Space. However, in this frequency range there is a significant attenuation of the signal due to the absorption of the radiation in the Earth atmosphere. In order to reduce such losses, THz observatories are placed on high mountains or balloons, airplanes or even satellites in Space. Radio astronomical facilities such as the ALMA interferometer [6], the APEX telescope [7], the Herschel

Space Observatory [8], COBE [9] and many others have been used or are used to explore various aspects of the Universe (see fig:1.2).

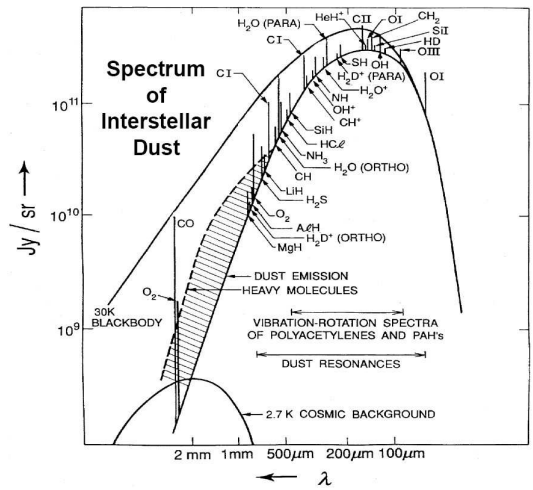

Fig. 1.1: Radiated energy versus wavelength of interstellar dust. Figure taken from: [5]

Fig. 1.2: Illustrations of several radio astronomical platforms. The Herschel Space Observatory [8], the APEX telescope [7], the ALMA interferometer [6] and COBE [9].

These THz radiation observation platforms require detectors with high sensitivity and a large bandwidth [10]. Today, heterodyne receivers used in high spectral resolution radio astronomy are based on cryogenic devices such as Superconducting-Insulator-Superconductor tunnel junctions (SIS) and superconducting hot electron bolometers (HEB) [11]. The use of those devices is motivated by the superior sensitivity and low local oscillator (LO) power requirements compared to e.g Schottky diode technology.

The choice of the THz detector is application dependent. In radio astronomy, the detector sensitivity is the main drive, hence cooled receiver are preferable whereas portable, cheaper and uncooled receivers are preferable for "terrestrial" applications.

1.2 THz detectors

Detection systems in the THz spectral range can be divided in two classes: incoherent detectors (direct) and coherent detectors (e.g. heterodyne). In the direct detection mode the total power received by the detecting devices is converted to an electrical signal (dc voltage or current). Incoherent detectors allow only signal amplitude detection without preserving the phase information (e.g. frequency) of the incoming signal. Selection of the frequency is possible if a filter is placed in front of the detector. In this case, the spectral resolution is determined by the filter bandwidth. Such detectors are suitable for studying radiation sources where high spectral resolution is not a requirement. Unlike incoherent detectors, coherent detectors preserve both the amplitude and the phase of the incoming radiation and they are used to characterize the signal with a very high spectral resolution.

Different types of detectors are employed at THz frequencies such as: Superconductor-Insulator-Superconductor (SIS) tunnel junctions and superconducting hot-electron bolometer (HEB), which are used as mixers; Golay cells, pyroelectric detectors, semiconductor bolometers mainly used in the incoherent detection mode; while Schottky diodes (SD) and field effect transistor (FET) can be employed both in the coherent and the incoherent detection mode. Figure 1.3 shows an overview of the double sideband (DSB) noise temperature versus frequency for Schottky, SIS and HEB mixers.

Schottky diodes are the most sensitive room temperature THz detectors. However, their performances degrade at frequencies higher than 1 THz (see figures 1.3 and 1.4) due to parasitic losses. Moreover, they require a large amount of local oscillator power (LO) (∼mW) [12], making it necessary to use large gas lasers as local oscillators, rather unpractical condition for space-borne observations. Their main advantages is that they have a wide IF bandwidth and they can operate in a wide temperature range and therefore they can be used when cryogenic cooling is not possible or too expensive. Such applications can be remote sensing of the Earth´s atmosphere or the study of the chemical process involved in the control of the climate, etc.

Using cooling (e.g. 4 K, liquid helium), Superconductor-Insulator- Superconductor (SIS) tunnel junctions [13] based on Nb (niobium) are the most sensitive mixers for frequencies below 1 THz. An additional advantage is their modest LO power requirement which is on the order of microwatts. The major drawback for SIS mixers is that the upper operating frequency is limited due to the superconducting energy gap frequency (700 GHz for Nb and about 1400 GHz for NbTiN) [14,15]. At frequencies beyond the gap frequency (f=2Δ/h [10]), the photon assisted tunneling is limited. Another limitation comes from the material of the tuning circuit used to compensate for the SIS junction capacitance. It is made from a superconductor, which losses increase above the energy gap with the consequence of decreasing the receiver sensitiv-

ity. Alternative materials, such as NbN and NbTiN, have been used instead of Nb to increase the operation frequency up to 1.2 THz [16].

An alternative to terahertz SIS mixers at frequency above 1.2 THz, is the superconducting hot-electron bolometer (HEB) mixer. Although HEB mixers provide a smaller IF bandwidth compared to Schottky diodes and SIS mixers, nevertheless the high sensitivity up to 5 THz [17] and the low LO power requirement ($<1\mu$W) [18], have determined the choice of HEB mixers for several ground and Space based observatories. [18].

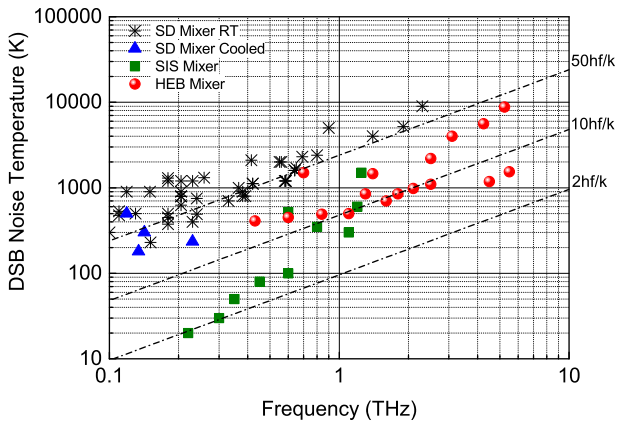

Fig. 1.3: State of the art performance of terahertz mixers. Room temperature and cooled Schottky diode mixer [10, 18–25], SIS mixer [18] and HEB mixer [17, 18].

Many "terrestrial" applications, such as THz imaging and wireless communications, require low-cost, fast and sensitive room-temperature THz detectors, operating up to several THz. In figure 1.4 the NEP as a function of the frequency is presented both for newest as well as for established technologies.

For Field Effect Transistors it is common knowledge that their application above the cut-off frequency is not possible. However if their channel can act as a resonator for plasma waves they can extend the operational frequency to several THz [26]. Silicon CMOS FETs [27] technology seems to present competitive performances, fast response and on-chip integration but as well as Schottky diodes their performances drop at higher frequency. Quite new technologies, in the transistors world, are nanowire based FETs and Graphene FETs in which very high mobility materials are used in order to see the electron ballistic transport [28, 29].

Room-temperature bolometers thermally isolated on thin membranes based on VO_x have been shown to operate at 4.3 THz [30]. Unfortunately, the discussed devices have a typical response time of several milliseconds beside the fact that the device processing is rather complicated. Free-standing bridge bolometers [31] based on thin films coupled with planar antenna have shown a high sensitivity, but like membrane bolometers they are slow and with a device fabrication not straightforward. An alternative to all the devices discussed so far as a THz direct detector operating at room-temperature is antenna-coupled

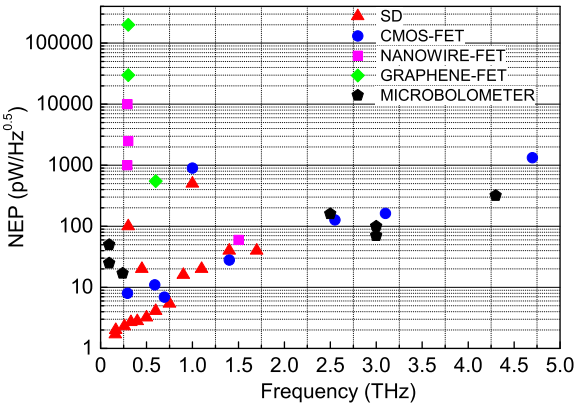

Fig. 1.4: State of the art performance of terahertz direct detectors at room-temperature. Schottky diode [32–37],CMOS-FET [27, 38], Graphene-FET [29, 39], Nanowire-FET [28, 40], Microbolometer [30, 31, 41–44].

bolometer supported substrate. The advantages of supported substrate bolometers are: quite straightforward fabrication, cheap technology and large array can be made. The discussed devices are know to be very sensitive at cryogenic temperature, however in this work it has been demonstrated that they can be sensitive as well as fast even at room-temperature.

1.3 Motivation of the thesis

This thesis addresses the following scientific objectives:

- **I**ncreasing the gain bandwidth (GBW) and the noise bandwidth (NBW) of HEB mixers beyond the presently achieved (3-4 GHz with NbN thin films) utilizing MgB_2 films. This without sacrificing the low noise performances.

- **D**evelopment of fast (ns response time) and sensitive (NEP less than $nW/Hz^{0.5}$) room-temperature bolometer for the THz frequency range.

Phonon-cooled HEB mixers made of ultrathin 3-4 nm NbN film have demonstrated superior performance over other type of mixers at frequencies above 1.2 THz [10, 17, 45]. The gain bandwidth was 3-4 GHz for 3-4 nm film [18] which is good enough for many radio astronomy applications. Further reduction of the NbN film thickness (less than 3-4 nm) leads to a drastic reduction of the critical temperature which acts towards the reduction of the GBW [46]. Therefore, increasing the GBW of phonon-cooled NbN HEB mixers beyond the presently achieved 3-4 GHz seem to be unrealistic. A possible method to extend the gain bandwidth is to use diffusion-cooled HEB mixers, where an extra electron cooling path occurs by out-diffusion of the electrons in to the contact pads. A gain bandwidth as large as 1.7 GHz and 6.5 GHz has been

demonstrate for Nb [47] and NbN HEB [48] mixers respectively. However, such HEBs require to be extremely short, as well as special treatment of the contact pads [49]. Therefore, it is rather difficult to achieve a repeatable and reliable fabrication process. Still, there is a need to increase the IF bandwidth[1] even further in order for example to measure several molecular lines simultaneously. Thanks to shorter electron-phonon interaction time (3 ps at 39 K [50]) compared to NbN (12 ps [51] at 10 K) and faster phonon escape time to the substrate, MgB_2 can provide a wider GBW for phonon-cooled HEB mixers. Moreover the higher critical temperature of MgB_2 compared to NbN makes it a very attractive device from a system perspective. In this thesis, new type of MgB_2 HEB mixers are explored with respect to low noise performances as well as gain bandwidth and fabrication methods (Paper [A]-[D]) with the overall goal to demonstrate better THz receivers for future Space instrumentations.

The second part of this thesis is devoted to room-temperature THz detection using $YBa_2Cu_3O_{7-x}$ microbolometers. $YBa_2Cu_3O_{7-x}$ is known to be a high Tc superconductor with a critical temperature as high as 92 K in the bulk [52]. In theory, the expected GBW is 140 GHz for $YBa_2Cu_3O_{7-x}$ HEB mixers considering an electron-phonon interaction time of 1.1 ps [53]. However, the $YBa_2Cu_3O_{7-x}$ crystal structure is rather complicated, and hence the deposition of very thin films with a high critical temperature is very challenging. As direct detectors at 77 K $YBa_2Cu_3O_{7-x}$ microbolometers have shown a flat responsivity up to 1.6 THz and a response time of 1 ns [54]. Moreover due to a rather high room-temperature coefficient of resistance makes $YBa_2Cu_3O_{7-x}$ films very suitable for THz detection and the room temperature resistivity is very suitable for integration with the majority of planar THz antennas. In combination with the high sensitivity, speed and simple fabrication process, the $YBa_2Cu_3O_{7-x}$ is a strong candidate for room-temperature THz microbolometers. In this thesis room-temperature $YBa_2Cu_3O_{7-x}$ microbolometers were studied with respect to the responsivity, the noise, the speed and the fabrication techniques (Paper [E]-[G]) with the overall goal to demonstrate better THz detectors which can be used for example to achieve a greater frame rate in a THz camera.

1.4 Thesis overview

The thesis is structured in 5 chapters. Chapter 1, gives an introduction to THz detection and existing technologies for radio astronomy, Space science and THz sensing. Moreover the motivation of this research is presented. Chapter 2 concerns the detailed description of bolometer working principles, direct and heterodyne detection, their figures of merit and basics of superconductivity. The material growth and bolometer fabrication process is described in Chapter 3. The experimental results of MgB_2 and $YBa_2Cu_3O_{7-x}$ microbolometers are given in Chapter 4 and Chapter 5, respectively. Finally, a summary of this

[1] For broadband line survey. One practical reason why large gain bandwidth is desiderate is that, in this way, it is possible to reduce the observation time. For example if a spectrum of several gigahertz as to be measured, this implies that the local oscillator has to be shifted several times. However, if a detector has large gain bandwidth the number of times that the local oscillator is shifted is reduced, and hence the observation time is reduced. Another reason is due to the Doppler shifts of a molecular lines within the gas cloud.

research and a description of future outlook are discussed.

Chapter 2

Background

In this chapter the bolometer operation and the main figure of merits which determine the bolometer performance are presented. Two ways to detect radiation, direct and heterodyne detection, are presented and discussed. Finally, basics of superconductivity and overview of properties of magnesium diboride and yttrium barium copper oxide superconductors are given.

2.1 Bolometer basics

In general, detection indicates an extraction of a specific information from an external solicitation. The term detector is used to describe a component which extracts a particular information from the radiation.

A bolometer is a thermal detector that is used to measure power of the incident electromagnetic radiation. In a thermal detector, the incident radiation is absorbed to change the material temperature, and the resultant change in some physical property is used to generate an electrical output. Usually, a bolometer is a thin slab of material whose impedance is temperature dependent. The bolometer can be made of superconducting, semiconducting, intermetallic or metals materials [55, 56]. Figure 2.1 shows schematically the temperature dependence of resistance of different material types used for making bolometer. A simplified schematics of a bolometer which consists of an absorber with heat capacity C and at temperature T_B which is in thermal contact with a reservoir at temperature T_{bath} via thermal conductance G_e is given in figure 2.2. The absorber is heated up by the incoming radiation. The temperature change is measured by the attached thermometer, exhibiting a temperature dependent resistance R(T). The thermometer is biased electrically e.g. in a constant current mode or voltage mode, and consequently the change in resistance results in a change of the voltage or the current across the thermometer. In a microbolometer the absorbing element in itself is made of a material whose the electrical resistance is a function of the temperature. Thus, the absorber is used as a thermometer.

The values of the heat capacity C and the thermal conductance G_e have influence on the bolometer performance, such as the voltage responsivity of the device to the absorbed radiation and the bolometer response time.

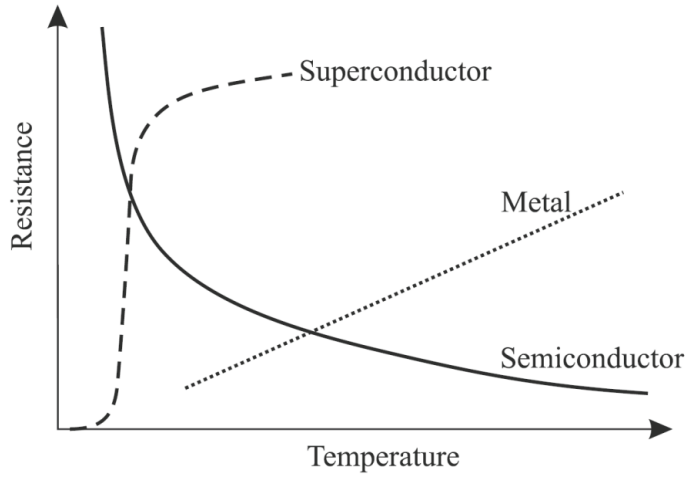

Fig. 2.1: Schematic temperature dependence of resistance of three bolometer material types. Resistances are not in scale. [57].

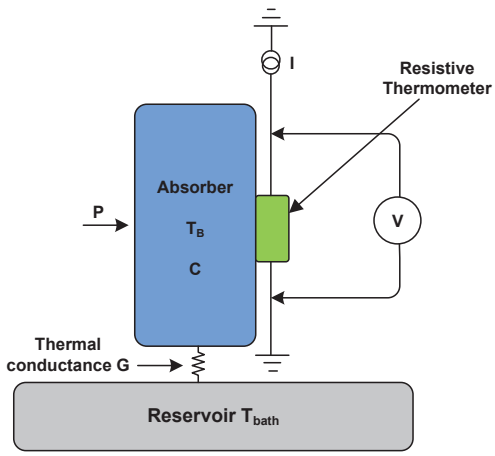

Fig. 2.2: Schematic of a composite bolometer which consists of an absorber with a heat capacity C and a thermometer. The bolometer is thermally coupled to a reservoir with temperature T_{bath}. The thermal coupling between the bolometer and the resorvoir is described by the thermal conductance G.

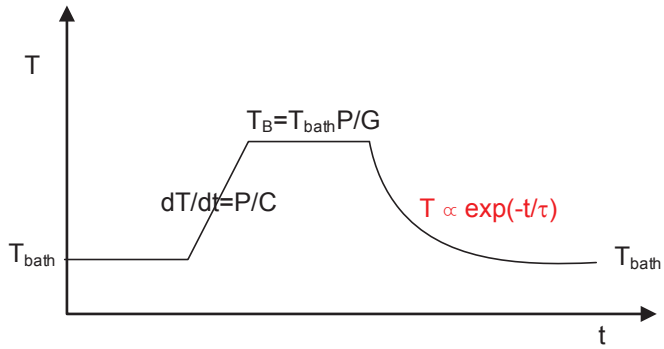

Fig. 2.3: Schematic representation of the bolometer working principle. The bolometer time constant $\tau = C/G_e$.

A bolometer that absorbs the incoming radiation can be described using a time varying power balance equation.

$$C\frac{dT_B}{dt} + G_e(T_B - T_{bath}) = P(t) \tag{2.1}$$

Where P(t) is the power absorbed which rises the temperature in the bolometer above the reservoir temperature (T_{bath}). Equation 2.1 is valid in the limit of (T_B-T_{bath})$\ll T_{bath}$. It is assumed that the heating in the bolometer is uniformly distributed[1]. In the steady state, the dT_B/dt=0 and the T_B-T_{bath}=P/G_e. When the power is absorbed, the temperature T_B of the absorbing element initially increases with time at a rate dT_B/dt=P/C and approaches a limit value of T_B=T_{bath}+P/G_e. When the bolometer is no longer irradiated the equation 2.1 can be written as:

$$C\frac{dT_B}{dt} + G_e(T_B - T_{bath}) = 0 \tag{2.2}$$

Solving equation 2.2 yields to:

$$T_B(t) = T_{bath} + \frac{P}{G_e}e^{-t/(C/G_e)} \tag{2.3}$$

The ratio $\tau \equiv C/G_e$ is the bolometer response time and it determines how fast the bolometer can relax to its equilibrium state. When the bolometer is no longer irradiated the bolometer temperature T_B relaxes back to the temperature of the thermal bath T_{bath} (see figure2.3). For a fixed thermal coupling coefficient a bolometer with a smaller heat capacity relaxes faster than a bolometer with a larger heat capacity. Similarly for a fixed heat capacity the thermal coupling coefficient determine how fast the heat is transferred from the bolometer body to the thermal bath. Bolometer with a larger G_e relaxes faster to the initial temperature state.

[1]For steady state heat flow. The equilibrium heat balance equation become: P=G_e(T_B-T_{bath}) assuming that T_B-$T_{bath}$$\ll T_{bath}$. The non-equilibrium heat balance equation become: P=A(T_B^n-T_{bath}^n). For each particular case n shall be defined separately, however for two objects with smooth surfaces n=4

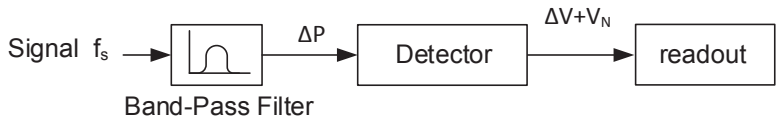

Fig. 2.4: Schematic of a direct detector.

2.2 Bolometer as a direct detector

A bolometer can detect radiation in two different ways: direct detection (incoherent detection) and heterodyne detection (coherent detection). In this section, the direct detection mode and the main figures of merit will be presented.

Figure 2.4 is a schematics of a direct detector. The bolometer responds to the total power of the radiation. If the RF signal (f_s) is amplitude modulated[2], the output voltage is measured using a lock-in amplifier or a voltmeter or a low noise amplifier etc. Direct detectors do not provide frequency discrimination hence, frequency selection can only be obtained if a filter is placed in front of the detector. Important figures of merit that characterize the performance of a bolometer as a direct detector are: the responsivity (R_V), the response time (τ) and the noise equivalent power (NEP).

2.2.1 Responsivity

The voltage responsivity is defined as the ratio between the voltage variation to the RF power absorbed into the detector.[3]

$$R_V = \frac{\Delta V}{\Delta P} \tag{2.4}$$

In order to understand which parameters influence the responsivity of the bolometer a more careful analysis of the equation 2.1 has to be done. Assuming that the bolometer absorbs power which changes periodically in time[4] (see eq.2.5).

$$P_B = P(t) = P_0 + P_1 e^{i\omega t} \tag{2.5}$$

[2]An envelop detector takes the high frequency signal as input and provides an output which is the envelop of the input signal. AC measures the envelop while DC the total power. For 100% modulation depth AC=DC.

[3]The responsivity can be also expresses as the ratio of the current variation to the absorbed RF power. In general, the responsivity is a measure of how much power is converted in an electrical signal.

[4]Part of this section follow [55].

The temperature of the bolometer changes as:

$$T_B = T(t) = T_0 + T_1 e^{i\omega t} \tag{2.6}$$

The bolometer which is biased at a constant current I, generates electrical heat (dc heating) which can be written as [55]:

$$I^2 R(T) = I^2 \left[R(T_0) + \left(\frac{dR}{dT} \right) T_1 e^{i\omega t} \right] \tag{2.7}$$

The bolometer looses power $\overline{G}(\mathrm{T}_B\text{-}\mathrm{T}_{bath})$ to the reservoir through the thermal conductance G. It should be also noted that G in general is a function of the temperature [55] but it is here assumed to be constant for small temperature changes. The therm $\overline{G}$ is an average thermal conductance. Considering equations 2.1, 2.5, 2.6, 2.7, equating the input to the output power and taking into account the power stored in the heat capacitance, gives [55]:

$$\begin{aligned} P_0 + P_1 e^{i\omega t} + I^2 R(T_0) + I^2 \left(\tfrac{dR}{dT} \right) T_1 e^{i\omega t} = \\ = \overline{G}(T_0 - T_{bath}) + G T_1 e^{i\omega t} + i\omega C T_1 e^{i\omega t} \end{aligned} \tag{2.8}$$

Where G is the dynamical thermal conductance dP/dT at the temperature T_0. Separating the time independent and the time dependent terms of the equation 2.8 yields to [55]:

$$P_0 + I^2 R(T_0) = \overline{G}(T_0 - T_{bath}) \tag{2.9}$$

$$\frac{\Delta P}{\Delta T} = P_1/T_1 = G + i\omega C - I^2(dR/dT) \tag{2.10}$$

The time independent terms gives the constant state heat flow equation that determines the operating temperature of the bolometer [55].

The voltage response is proportional (and linear) to ΔP. The amplitude of the voltage at the read-out can be written as $\mathrm{V(t)}=\mathrm{V}_0+\mathrm{V}_1\mathrm{e}^{i\omega t}$, hence using the equations 2.4 and 2.10 the voltage responsivity can be defined as:

$$R_V = \frac{\Delta V}{\Delta P} = \frac{I \Delta R}{\Delta P} = I(dR/dT)T_1/P_1 = \frac{I(dR/dT)}{G - I^2(dR/dT) + i\omega C} \tag{2.11}$$

The responsivity is influenced by the electrothermal feedback i.e. when the resistance of the bolometer changes due to the absorbed power, the dc dissipation also changes. The result is the effective thermal conductance defines as:

$$G_e = G - I^2(dR/dT) \tag{2.12}$$

In order to characterize the bolometer (thermometer) it is important to introduce the temperature coefficient of resistance (TCR is material dependent), α, given by:

$$\alpha = \frac{1}{R} \frac{dR}{dT} \tag{2.13}$$

From equations 2.13 and 2.12 the effective thermal conductance can be written as:

$$G_e = G - I^2 R \alpha \tag{2.14}$$

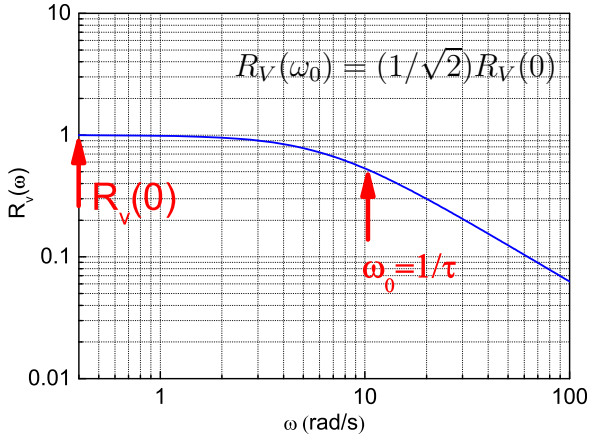

Fig. 2.5: Representation of the responsivity versus frequency

Semiconducting bolometers have a negative α resulting in G_e>G. On contrary, superconducting bolometers have a positive α hence G_e<G. By having α>0 and a current biased bolometer, can be possible that the effective thermal conductance equals to zero at a large current. The result is a very high voltage responsivity which results in an overheated device and the device will deteriorate and inevitably be destroyed. This analogous effect, called thermal runaway, occurs if the bolometer is voltage biased and α<0.

Plugging in the equation 2.14 in 2.11 the responsivity can be written as:

$$R_V = \frac{IR\alpha}{G_e(1 + i\omega\tau)} \tag{2.15}$$

Considering that $R_V(0)$=I$R\alpha/G_e$ is the responsivity at $\omega(0)$ (see fig.2.5) and taking the module of the complex of equation 2.15:

$$R_V(\omega) = \frac{R_V(0)}{\sqrt{1 + \omega^2\tau^2}} \tag{2.16}$$

The response time, τ, in the equation 2.16, determines the response rate $(1/\tau)$ of the bolometer, and as was mentioned earlier it is given by the ratio between the heat capacity and the thermal conductance[5]. At a modulation frequency smaller compared to the bolometer time constant (ω<<$1/\tau$), the responsivity $R_V(\omega)$ is proportional to $1/G_e$, hence in order to make a sensitive bolometer the thermal coupling coefficient G_e should be reduced (this is the most common operational mode for bolometers). On the other hand, when the modulation frequency is higher than $1/\tau$, the bolometer responsivity is inversely proportional to the heat capacity and it falls with the frequency

[5]The thermal feedback influences the response time τ of the bolometer. The corresponding time constant is τ=C/G_e.

($R_V(\omega) \propto 1/C\omega$)). In order to make high sensitive detector the heat capacity can be reduced in this operational mode. A trade off between a high response rate and a responsivity should be found for practical bolometric detector, since it is not possible to maximize both, simultaneously. In some applications, it is important to have both a high response rate and a high responsivity. The latter can be reached by reducing G_e, but on the other hand this will make the bolometer slower. In order to keep τ small, the heat capacity C of the bolometer body can be reduced by, for example, using low specific heat materials or by reducing the bolometer volume. For microbolometers on bulk substrate, the thermal conductance G_e is equal to the ratio between the bolometer area and the thermal boundary resistance R_{bd} (see eq.2.17) [58] if the bolometer dominant cooling is into the substrate.

$$G_e = \frac{A}{R_{bd}} \tag{2.17}$$

Therefore making bolometers smaller leads to an increase of the responsivity. The heat capacitance is given by:

$$C = V_{bol}\rho_m c_v = Ad\rho_m c_v \tag{2.18}$$

where V_{bol} is the bolometer volume, ρ_m the mass density and c_v the volumetric specific heat. Plugging in equations 2.17 and 2.18 into the response time formula (τ=C/G_e) the following equation is deduced:

$$\tau = \frac{Ad\rho_m c_v}{A/R_{bd}} = d\rho c_v R_{bd} \tag{2.19}$$

It is clear from 2.19 that the reduction of the bolometer area does not yield to a reduction of the device response rate ($1/\tau$).

The responsivity is directly proportional to the temperature coefficient of resistance, α. Thus, in order to optimize the bolometer sensitivity, the absorber should be made from a material with large TCR . Other possibilities to increase the bolometer responsivity are: placing the bolometer on a thin membrane [59] or forming free-standing bridge bolometers (see fig. 2.6) [31]. The weak thermal coupling with the reservoir (small G), results in a very high responsivity. Nevertheless, the response rate of such bolometer is very slow ($\tau \sim$ms) due to the small thermal conductance.

2.2.2 Noise

An incoherent detector provides a voltage (ΔV) proportional to the absorbed RF power and an extra noise (V_N) (see figure 2.4). The sensitivity of a direct detector is quoted in terms of noise equivalent power (NEP) which is defined as the ratio between the device voltage noise (V_N) and the responsivity (R_V). The NEP is also defined as the radiant power that produces a signal to noise ratio of unity at the output of the receiver. For sensitive detectors (low NEP), it is important to make devices with a very low output noise and a high responsivity.

A microbolometer is a thin film resistor with a high temperature coefficient of resistance. Therefore, noise process in a bolometer are the same as in a

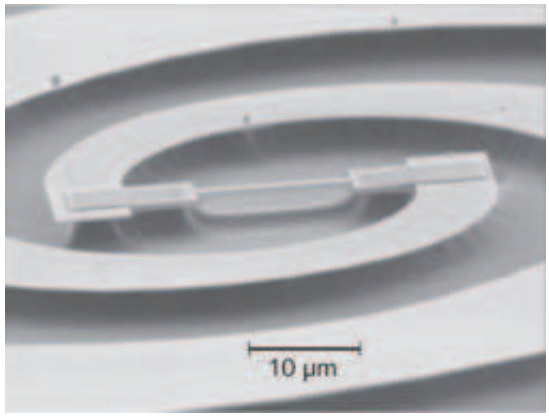

Fig. 2.6: Air bridge bolometer [31].

resistor. The noise contribution in a bolometer are: the Johnson noise (thermal noise or Nyquist noise), the phonon noise (thermal fluctuation noise) and, for biased device, the low frequency flicker noise (1/f noise).

The Johnson noise is generated by the thermal agitation of the charge carriers (usually electrons) inside an electrical conductor at thermal equilibrium, at any applied voltage. It is dependent on the device resistance (R) and the temperature (T) and it is defined as [60]:

$$V_{NJ} = (4Rk_BTB)^{0.5} \tag{2.20}$$

Where k_B is the Boltzmann´s constant and B is the bandwidth.

Fluctuations in energy in a bolometer produce a noise which is called thermal fluctuation noise or phonon noise. The thermal fluctuation noise which generates fluctuations of the temperature in the bolometer is caused by quantized carries of energy (electrons, phonons, photons or quasi-iparticles) passing from the bolometer over the thermal conductance G to the substrate. The phonon noise is directly proportional to the thermal conductance, G, the temperature and the responsivity [55] and it is given by:

$$V_{NFL} = (4k_BT^2G)^{0.5}R_V \tag{2.21}$$

The frequency dependence of this noise source follow the one of the responsivity.

The flicker noise is a result of many noise sources correlated to impurities, traps, etc; as well as resistance fluctuation which is transformed in current or voltage fluctuation. At low frequencies the flicker noise may become important. Because of its frequency dependence, the flicker noise is also called 1/f noise. The flicker noise is described by the following equation [55]:

$$V_{NF} = N_N I^x F(f) \tag{2.22}$$

where N_N term specifies the strength of the noise and the I^x indicates that the flicker noise is bias dependent. The frequency dependence of the flicker noise follows the 1/f trend: $F(f)=f^{-\gamma}$, where γ is close to 1 in most cases.

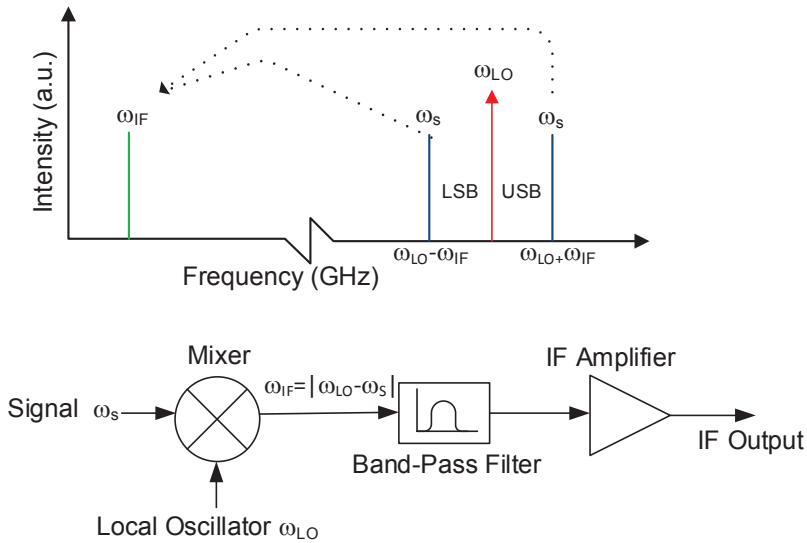

Fig. 2.7: Schematic of down-conversion in a heterodyne receiver. The mixer has two inputs ports for the local oscillator (LO) and the signal and one output port for the intermediate frequency (IF).

As discussed above, the 1/f noise can arise from many different sources so in general there are no ways to estimate it and measurements are needed.

Considering these sources of noise, for 1 Hz (post detection bandwidth), the overall noise equivalent power is calculated as [55]:

$$NEP^2 = \frac{4Rk_BT}{R_V^2} + 4k_BT^2G + \frac{N_N^2 I^{2x} F(f)^2}{R_V^2} \tag{2.23}$$

2.3 Bolometer as a heterodyne detector

In the heterdodyne detection mode the amplitude and the phase information of the incoming radiation is preserved. In this case the detecting device is used as a mixer. Figure 2.7 is a schematic of down-conversion in a heterodyne receiver. A weak signal at frequency ω_S is mixed with a strong local oscillator at frequency ω_{LO} and down converted to an intermediate frequency ω_{IF}.

If two RF signals with slightly different frequencies are applied to a bolometer, the total RF voltage across the bolometer can be written as:

$$V(t) = V_{LO}\cos(\omega_{LO}t) + V_S\cos(\omega_S t) \tag{2.24}$$

where V_{LO} and V_S are amplitudes of the voltages of the local oscillator and of the signal at the input of the mixer. The total power dissipated in the bolometer is proportional to the sum of the amplitudes squared of the voltage through the following equation:

$$\begin{aligned} P(t) \quad \propto \quad & (V_{LO}\cos\omega_{LO}t + V_S\cos\omega_S t)^2 = \\ & = +(V_{LO}\cos\omega_{LO}t)^2 + (V_S\cos\omega_S t)^2 + \\ & +2V_{LO}V_S(\cos(\omega_{LO}+\omega_S)t + \cos(\omega_{LO}-\omega_S)t) \end{aligned} \tag{2.25}$$

The bolometer cannot follow the power oscillation at $2\omega_{LO}$, $2\omega_S$ and $\omega_{LO}+\omega_S$ frequencies, if those oscillations are much larger than the bolometer response rate $(1/\tau)$. Defining $\omega_{IF} = |\omega_{LO} - \omega_S|$, the bolometer on contrary can follow the variation of the power $\propto 2V_{LO}V_S\cos(\omega_{IF})t$, if ω_{IF} is smaller than the $1/\tau$.

$$P(t) = P_{LO} + P_S + 2\sqrt{P_{LO}P_S}\cos(\omega_{IF}t) \tag{2.26}$$

Where $P_{LO}=V_{LO}^2/2R$ and $P_S=V_S^2/2R$.

As it follows from equations 2.25 and equation 2.26 the IF output at ω_{IF} can be produced by either $\omega_S = \omega_{LO}+\omega_{IF}$ (above ω_{LO}) and $\omega_S = \omega_{LO}-\omega_{IF}$ (below ω_{LO}). Those frequencies are said to belong to either the upper side band (USB) or the lower side band (LSB).

Mixers which are sensitive to USB and LSB are called double sideband (DSB). Any mixer is a double sideband mixer, nevertheless it can operates as single sideband (SSB) [61] if only the upper sideband (USB) or the lower sideband (LSB) is transmitted. All the HEB mixers discussed in this thesis are of DSB type. Important figures of merit which characterise a (bolometric) mixer are: the conversion efficiency or the gain, the gain bandwidth and the mixer noise temperature.

2.3.1 Conversion efficiency and gain bandwidth

A standard model describing performance of hot electron bolometer mixers was developed by Arams at al [62]. The model analyses the mixer (see figure 2.9) assuming that the heating is uniformly distributed in the bolometer, and therefore the all bolometer is considered to be at the same temperature. The conversion efficiency is defined as a ratio of the output power P_{IF} at IF frequency to the available signal power P_S at the input. According to the uniform heating model [62], the conversion efficiency is defined as:

$$\begin{aligned} \eta_m(\omega_{IF}) \quad = \quad & \frac{P_{IF}}{P_S} = \frac{2I^2C_0^2P_{LO}R_L}{(R_L+R_0)^2} \times \\ & \times \left(1 - I^2C_0\frac{R_L-R_0}{R_L+R_0}\right)^{-2} \times (1+\omega_{IF}^2\tau^2)^{-1} \end{aligned} \tag{2.27}$$

Where $C_0=dR/dT\times 1/G$ is the self heating parameter, P_{LO} is the local oscillator power, $R_0=V_0/I$ is the bolometer DC resistance and R_L is the IF load resistance. In the expression 2.27 the first term reflects the conversion from the incident signal power to the power dissipated in the load. The second term describes the electrothermal feedback through the IF load, what will be discussed later in the section.

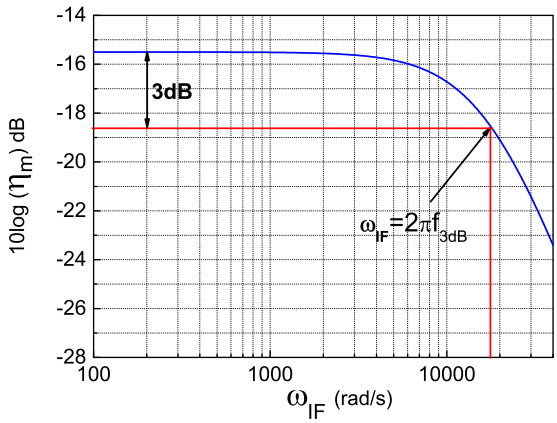

Fig. 2.8: Representation of the conversion efficiency as a function of the IF frequency.

The conversion efficiency as a function of the IF frequency is shown in figure 2.8. At $\omega_{IF} = 2\pi/(\tau)$, the mixer gain drops by a 3 dB from its value at low IF frequencies. In a simple case, when $\omega_{IF} > 2\pi/(\tau)$, the conversion efficiency keeps rolling off hence the mixers sensitivity reduces. The value $f_{3dB} = 1/\tau$ defines the mixer gain bandwidth. The gain bandwidth (f_{3dB}) is defined as the IF frequency in which the conversion efficiency drops by a factor of two from the mixer gain at zero IF frequency. The mixer gain bandwidth is expressed by the following equation and it is determined by the mixer response time, τ_θ modified by the electrothermal feedback through the IF circuit [63].

$$f_{3dB} = \frac{1}{2\pi\tau} \tag{2.28}$$

$$\tau = \frac{\tau_\theta}{1 - I^2 C_0 \frac{R_L - R_0}{R_L + R_0}} \tag{2.29}$$

τ is the electron temperature relaxation time and τ_θ is the relaxation time for I=0.

Figure 2.9 shows the equivalent circuit of a bolometric mixer connected to an IF amplifier through a capacitor C, and inductively coupled to the DC bias circuit. The bolometer is biased in its resistive state by a dc current and by the LO radiation (see figure 2.10). The capacitor does not let the dc bias current flow through the IF amplifier which follows the HEB mixer. The electrothermal feedback affects the mixer conversion gain and the time constant (see equations 2.27 and 2.29). The electrothermal feedback is referred to the response of the electrical circuit to the device thermal response. Positive and negative feedback can be distinguished, depending if the bolometer is biased in constant current or voltage mode respectively as well as on the sign of the temperature coefficient of resistance (TCR is positive for superconductor). If the bolometer is biased at constant current, a small increase of the resistance leads to an increase of the dc power dissipated (see figure 2.10). The increase

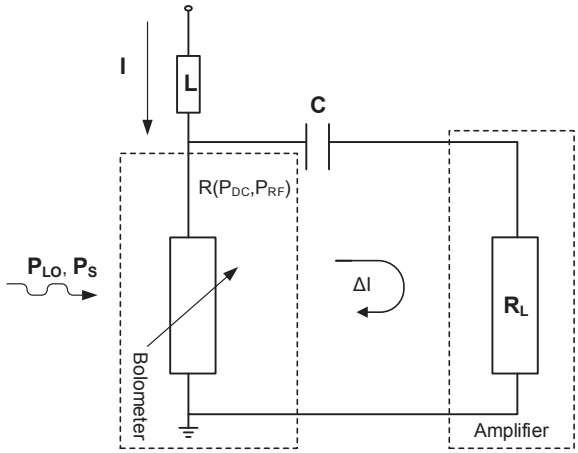

Fig. 2.9: Equivalent circuit of a bolometer mixer connected to the dc and IF circuit. The bolometer is shown as a variable resistor, connected to the IF load through the capacitor C, and inductively connected to the bias circuit.

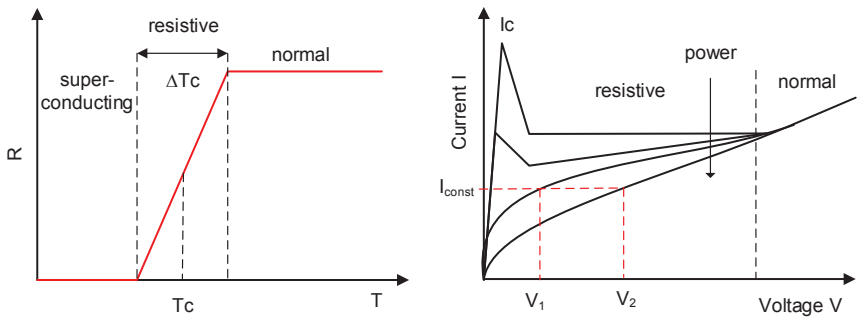

(a) (b)

Fig. 2.10: (a) Representation of R(T) characteristic of a superconducting HEB. The three states are indicated in figure. (b) Rapresentation of I(V) characteristic of a superconducting HEB. The three states are indicated in figure.

in the dc heating results in a further increase of the resistance and the results is a positive feedback. The positive feedback increases the bolometer time constant (see equation 2.29). The negative feedback occurs when the bolometer is voltage biased. An increase in resistance causes a compensating decrease of the dc dissipation and thus the time constant decreases. A small signal (P_S) added to the local oscillator causes a bolometer resistance modulation at the IF frequency and hence an IF voltage appear across the device.

The inductive element in the dc bias circuit (see fig.2.9) is a high impedance for the IF current. Thus, the IF current flows only to the load (R_L). In this case the electrothermal feedback in the bolometer is generated by the dc dissipation. This is analogous to the DC dissipation discussed before. The nature of the electrothermal feedback, in this case, is determined by the relative value of the load (which can acts as current or voltage source) respect to the bolometer resistance. The electrothermal feedback is completely suppressed when the bolometer impedance matches the IF load resistance.

2.3.2 Noise Temperature

The overall performances of a heterodyne mixer are usually expressed in term of the noise temperature at the input, determined by the ratio between the output noise and the gain of the mixer. The noise temperature of a mixer depends on whether the mixer is SSB or DSB. The mixer will down-covert noise in both sidebands frequencies, but the power of the SSB signal is one-half compared to the power of the DSB signal. Therefore, the noise temperature of a SSB mixer is twice of the DSB mixer.

In a bolometric mixer, the thermal fluctuation noise and the Johnson noise are the main sources of noise [64,65]. Temperature fluctuations in a bolometer cause resistance fluctuations which generate the thermal fluctuation noise. The output thermal fluctuation noise temperature in a bolometer is given by [66]:

$$T_{FLn,out}(\omega_{IF}) = I^2 C_0 \frac{dR}{dT_e} T_e^2 \frac{4R_L}{(R_0+R_L)^2} \left(1 - I^2 C_0 \frac{R_L - R_0}{R_L + R_0}\right)^{-2} (1+\omega_{IF}^2 \tau^2)^{-1} \tag{2.30}$$

The Johnson noise, $T_{Jn,out}$ is equal to the noise which an ordinary resistor at a temperature, T_e delivers into a load R_L.

$$T_{Jn,out} = T_e \frac{4R_0 R_L}{(R_0+R_L)^2} \left(1 - I^2 C_0 \frac{R_L - R_0}{R_L + R_0}\right)^{-2} \tag{2.31}$$

The mixer output noise temperature is a sum of the thermal fluctuation noise and the Johnson noise.

$$T_{out}(\omega_{IF}) = T_{FLn,out}(\omega_{IF}) + T_{Jn,out} \tag{2.32}$$

The DSB mixer noise temperature, referred to the receiver input is given by:

$$T_m(\omega_{IF}) = \frac{T_{out}(\omega_{IF})}{2 \times \eta_m(\omega_{IF})} \tag{2.33}$$

Here η_m is the single sideband conversion efficiency.

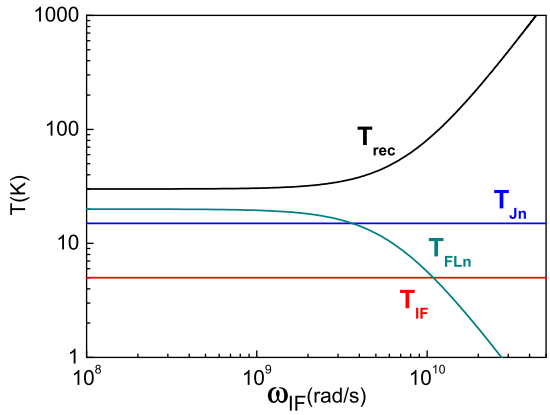

Fig. 2.11: Representation of the noise contributions in a receiver. The plot is based in a qualitatively analysis.

.

The receiver noise temperature is defined as the sum of the mixer noise temperature and the IF chain noise temperature as follows:

$$T_{rec}(\omega_{IF}) = \frac{(T_{FLn,out} + T_{Jn,out} + T_{IF})}{\eta_m(0)}(\omega_{IF}^2\tau^2) \tag{2.34}$$

Figure 2.11 shows a representation of the noise contributions in a receiver. The noise bandwidth can be expressed by the equation 2.35 and it is defined as an IF where T_{rec} rises by a factor of two.

$$f_n \approx f_{3dB}\sqrt{\frac{T_{FLn,out} + T_{Jn,out} + T_{IF}}{T_{Jn,out} + T_{IF}}} \tag{2.35}$$

As it follows the noise bandwidth is larger than the gain bandwidth [67], and this difference increases if the thermal fluctuation noise increases over the other noise sources (the Johnson noise and the IF noise).

Figure 2.12 is a representation of the experimental setup used in chapter 4 with the noise contributions. In order to understand the sensitivity of an HEB mixer it is very important to estimate the losses and the noise added by all the various parts of the setup. For a cascade of components each with a gain and a noise temperature referred to the input, the equivalent noise temperature of the chain is given by the Friis equation [68]:

$$T_{eq} = T_1 + \frac{T_2}{\eta_1} + ... + \frac{T_n}{\eta_1 \times ...\eta_{n-1}} \tag{2.36}$$

Using equation 2.36, for the receiver setup depicted in figure 2.12, the equivalent receiver noise temperature is given by:

$$T_{eq,rec} = T_{opt} + \frac{T_m}{\eta_{opt}} + \frac{T_{IF}}{2 \cdot \eta_m \cdot \eta_{opt}} \tag{2.37}$$

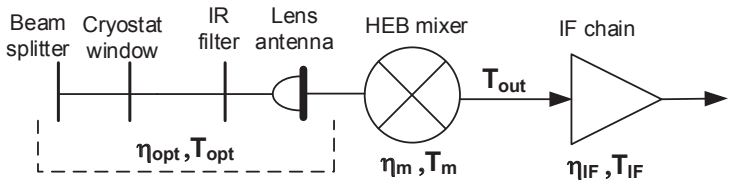

Fig. 2.12: Schematics of a heterodyne receiver (HEB as a mixer). Noise temperature and gain of the optical and electrical component are indicated.

Where T_{opt} and η_{opt} are the noise temperature and the gain of the optics while T_{IF} is the noise temperature of the IF amplifier. The quantitative analysis of the losses in the beam splitter, in the cryostat window, and in the IR filter will be presented in Paper [D].

2.4 Hot Electron Bolometer mixers

Hot Electron Bolometer (HEB) mixers using semiconductors (InSb) were invented in the early 1970s [62, 69], however development of superconducting versions of this basic concept has lead to the most sensitive mixers at frequencies in the terahertz region. Hot electron bolometer mixers are a thin superconducting strip on a dielectric substrate coupled between contact pads (see fig.2.13). Compared to direct detectors, in which the bolometer is at a temperature close to that of the substrate, in the HEB mixers electrons are heated up much above the substrate. Superconducting HEBs can be integrated with any planar antenna (i.e. logarithmic spiral or twin-slot antenna) as well as with waveguides [70]. A HEB, operating as a mixer, is cooled down below its critical temperature. At low temperature ($T<T_c$), the thermal coupling between free electrons and phonons in the superconducting bridge is weak while the electron-electron interaction is strong. If a photon with an energy $\hbar\omega$ (LO power) is absorbed in the HEB it breaks a Cooper pair or excites a normal electron (quasi-particle). The excited electron looses its energy by emitting a phonon which dependent on the photon energy ($\hbar\omega > 2\triangle$) may have sufficient energy to break other Cooper pairs. The excited electrons share their energy with other electrons via electron-electron interaction. It results in a rise of the electron temperature above the temperature of phonons. At the maximum HEB sensitivity point the electron temperature is close to the T_C.

There are two of cooling processes which determine the electron temperature relaxation time and consequently the gain bandwidth of an HEB mixer. These mechanisms are: electron diffusion from the HEB to contact pads (for very short HEBs) and electron scattering on phonon (phonon cool-

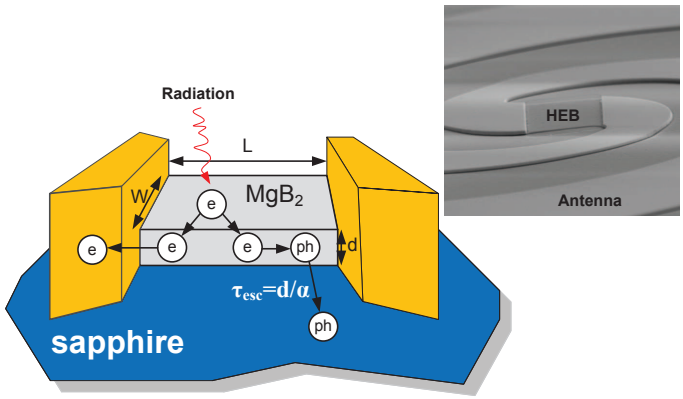

Fig. 2.13: Simplified picture of a superconducting Hot Electron Bolometer with phonon and electron diffusion cooling mechanisms. The SEM image shows a HEB integrated with a spiral antenna.

ing). If the length of the microbridge is shorter than the thermal diffusion length $L_{th}=(D\tau_e)^{1/2}$ of the superconducting material, the cooling mechanism is deminated by outdiffusion of the electrons to the contact pads within a time, $\tau_{diff}=(L^2/\pi^2 D)$. HEB mixers based on this principle are called diffused-cooled [49]. If the length of the microbridge, L is larger of the thermal diffusion length, L_{th} cooling by phonons dominates. These mixers are called phonon-cooled. Figure 2.13 shows a picture of an HEB with a representation of the electron diffusion and phonon cooling mechanism. In phonon-cooled HEB mixers [18] the electron temperature relaxation time, τ_θ is determined by the electron-phonon interaction time, τ_{e-ph}, the phonon-electron interaction time, τ_{ph-e}, the phonon escape time, τ_{esc} and the reverse flow of the phonons from the substrate to the to the film (see also 2-T model in chapter 4) . The electron-phonon interaction time is determined by the film internal structure as well as by the temperature, T [71]:

$$\tau_{e-ph} = A \times T^{-\mu} \tag{2.38}$$

The value of μ has been reported between 1 and 4 for various materials [72]. The phonon-electron interaction time is related to the electron-phonon interaction time:

$$\frac{c_e}{\tau_{e-ph}} = \frac{c_p}{\tau_{ph-e}} \tag{2.39}$$

c_e and c_{ph} are the electron and the phonon specific heats which are dependent on the temperature of the film ($c_e \propto$T and the phonon heat capacity below the Debye temperature $c_{ph} \propto T^3$). τ_{esc} is the escape time of the phonons from the HEB to the substrate which is dependent on the film thickness d, the speed of sound u and the film/substrate acoustic phonon transmission coefficient β.

$$\tau_{esc} = \frac{4d}{\beta u} \tag{2.40}$$

In order to prevent long response time and hence accumulation of heat in the phonon subsystem of the film, the phonon escape time has to be made much

shorter than the phonon-electron interaction time. In this way the energy transferred to the phonon subsystem is quickly removed from the film and transferred to the substrate. In the low-temperature limit, if the electron specific heat, c_e is much larger than the phonon specific heat, c_{ph}, the electron temperature relaxation time,τ_θ, is given by [73, 74]:

$$\tau_\theta = \tau_{e-ph} + \frac{c_e}{c_{ph}}\tau_{esc} \tag{2.41}$$

For an opposite situation, when $c_{ph} \geq c_e$, the relation of the τ_θ to τ_{esc} ,τ_{e-ph} and τ_{ph-e} is much more complex and it will be discussed in chapter 4.

If the HEB sizes is smaller than the phonon mean free path in the substrate then the phonon back flow from the substrate into the HEB can be neglected.

In conclusion, for a fast response of the phonon-cooled HEB mixer it is required to use thin films ($\tau_{esc} \propto d$) with a higher critical temperature (see equation 2.38). On the other hand the critical temperature decreases for thinner film thickness, which mostly occurs due to the large number of defects of the first layer of the film. An optimum between these two parameters must be found to maximize the gain bandwidth.

2.5 Basics of superconductivity and material choice

This section concerns the basics of the superconductivity with focus on the important parameters for superconducting HEB mixers.

Two basic properties of a superconductor, commonly cited are: the perfect diamagnetism and the zero resistance to a dc current. At a certain temperature called the critical temperature, T_c, the resistance of a superconductor drops to zero and remains zero at all temperatures below T_c. At $T<T_c$ conduction electrons from pairs, called Cooper pairs which carry current (supercurrent) without any resistance. Cooper pairs are also responsible for the perfect diamagnetism in the superconductors known as the Meissner effect.

Based on behaviour in magnetic filed, superconductors are divided in two classes. Type-I exhibits positive superconductor-normal interface energy while type-II negative interface energy [75].

Type-I is a perfect diamagnet. In fact below a the critical magnetic field, H_c, there is no penetration of the flux in the superconductor except for a thin layer of λ_L through which the field exponentially decays [75]:

$$\lambda_L = \left(\frac{\varepsilon_0 m c^2}{n e^2}\right)^{1/2} \tag{2.42}$$

Where n is the superconducting electron density. Above the critical field the material is driven to the normal state.

Type-II superconductors have more complex magnetic properties. There are two critical fields for such type of superconductors, H_{c1} and H_{c2}. For $H<H_{c1}$, the superconductor expels the magnetic flux as for Type I. For magnetic field is in the range $H_{c1}<H<H_{c2}$ some magnetic fluxes are trapped and

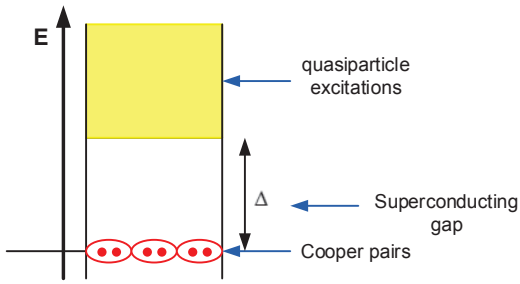

Fig. 2.14: Energy diagram of a superconductor

both the superconducting and the normal phases coexist. At H>H_{c2} the material becomes totally normal.

The energy gap, Δ, the London penetration depth, λ_L and the coherence length, ξ, together with the critical temperature and the critical magnetic fields are important parameters which characterize a superconductor.

In the BCS theory, the energy gap Δ is related to the critical temperature [75]. It separates the energy level of the ground state (Cooper pairs level) and the energy levels of the quasiparticle excitations (see fig.2.14).

$$\Delta(0) \propto k_B T_c \tag{2.43}$$

The minimum energy to break the Cooper pairs and create two quasiparticles is 2Δ.

The coherence length, ξ, is related to the Fermi velocity and the energy gap of the superconducting material and it is also related to the size of the Cooper pair [75].

$$\xi = \frac{\hbar v_F}{2\Delta} \tag{2.44}$$

The ratio between the penetration depth and the coherence length is an important parameter which determines if the superconductor is a type-I or a type-II.

$$k = \frac{\lambda_L}{\xi} \tag{2.45}$$

More precisely, $0 < k < 1/\sqrt{2}$ gives a type-I superconductor whereas if $k > 1/\sqrt{2}$ gives a type-II superconductor [75].

In this work two types of superconductors were used. Magnesium diboride and yttrium barium copper oxide were investigate as materials of choice for THz detection at cryogenic and room-temperature, respectively. Magnesium diboride was used as superconducting material for THz HEB mixers development. Despite yttrium barium copper oxide is known as high a Tc superconductor, in this thesis, it was used as material for THz detection from normal state up to the room-temperature.

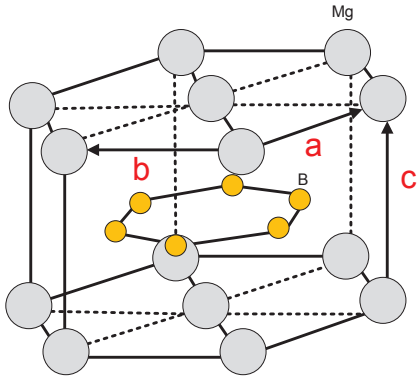

Fig. 2.15: MgB_2 crystal structure. The magnesium atoms show an hexagonal layer, while the boron atoms a graphite like honeycomb layer [76] .

The superconductivity in magnesium diboride (MgB_2) was discovered by Akimitsu´s group in 2001 [76]. Since then researchers have placed large attention for this new material. MgB_2 is a conventional intermetallic compound superconductor (a not cooper-oxide based superconductor) with the highest critical temperature (39 K in the bulk) that has been reported so far (23 K for Nb_3Ge [77]). The crystal structure of the MgB_2 is shown in figure 2.15. It consists of a Mg plane containing just magnesium and a B plane containing just boron, which are layered alternatively along the c axis. X-ray diffraction spectrum indicates a hexagonal crystalline structure, where the lattice constants are: a=b=0.3086 nm and c=0.3524 nm [78]. MgB_2 is a conventional BCS superconductor with Cooper-pairs formed via electron-phonon interaction. Study of the MgB_2 electron properties revealed a double conduction band structure with different energy gaps, $\Delta(0) \sim 2$ meV and $\Delta(0) \sim 7$ meV [79].

When a superconductor material is chosen for the fabrication of a HEB mixers fundamental parameters must be taken into consideration such as the critical temperature, the electron phonon interaction time, the thickness, the acoustic coupling between the film and the substrate, etc. As it was previously discussed important figure of merit for mixing are: the conversion efficiency, the IF bandwidth and the noise temperature. A low noise temperature and a low LO power requirements determined the choice of HEB mixer for the Herschel space observatory. However, HEB mixers made of NbN films exhibit a limited gain bandwidth to only 3-4 GHz in very thin films (3-4 nm) [80]. Further reduction of the NbN film thickness leads to a drastic reduction of the critical temperature which weakens the electron-phonon interaction time. In order to increase the gain bandwidth of HEB mixers a solution is to search for materials with a faster response.The high critical temperature of MgB_2 film (39 K in the bulk) [76], makes it very attractive to replace NbN with MgB_2, aiming for better performances. Considering equation 2.40, it is apparent that a larger gain bandwidth can be achieved using very thin films. However, thinner films usually have a critical temperature much lower than in bulk which will effect the electron phonon interaction time and so the device speed. It has been demonstrated that even thin MgB_2 films (7.5 nm) can exhibit a

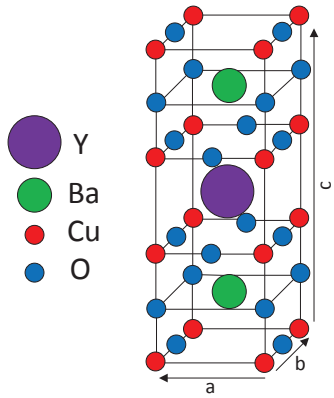

Fig. 2.16: $YBa_2Cu_3O_7$ crystal structure. [86].

critical temperature as high as 34 K [81]. Furthermore, using time domain spectroscopy, the electron-phonon interaction time has been measured to be 3 ps in a thin film MgB_2 on a silicon substrate [50] which is shorter compared to NbN film. Indeed in thin NbN films the electron-phonon interaction time has been measured to be 12 ps at 10 K [51] whereas the escape time was 40 ps [80].

Other film parameters that one should take into consideration for the HEB mixer design are: the film's speed of sound and the acoustic matching film/substrate. By choosing a substrate with a better matching the escape time can be reduced. It has been reported that in MgB_2 films, the speed of sound is very similar to substrates which are very common for terahertz detectors (Si, MgO and Al_2O_3) and higher than in NbN films [82–85]. Considering the higher critical temperature (even for ultrathin films) and shorter electron-phonon and phonon escape times in MgB_2 films compared to NbN film, HEB mixers based on MgB_2 can be faster than NbN HEB mixers. Concerning the mixer sensitivity films with a higher critical temperature might have higher noise and will require a higher local oscillator power. Mixers characteristics must be balanced in order to optimize the performance of the MgB_2 HEB mixers.

Yttrium barium copper oxide ($YBa_2Cu_3O_{7-x}$) has been made the material of choice that has been used in this work for room-temperature THz detection. $YBa_2Cu_3O_{7-x}$ is known to be a high temperature superconductor. Superconductivity in $YBa_2Cu_3O_{7-x}$ was discovered in 1987 and it is class II superconductor with a critical temperature as high as 92 K in the bulk material [52]. Its discovery was considered to be a breakthrough since the critical temperature was very well above the boiling point of the liquid nitrogen. The crystal structure of $YBa_2Cu_3O_{7-x}$ is a stuck of three cubic pirovskites cells. As it is possible to see from figure 2.16, each pirovskite contain Y or Ba at the center of the cell while the Cu atoms are in the corner and oxygen is placed in the middle between two Cu atoms. Oxygen content has very important role in order that YBCO becomes a superconductor. When x=1 the YBCO is insulator with a tetragonal crystal structure. If oxygen is introduced (by reducing x) the crystal structure changes to orthorhombic and the ma-

terial become superconductor with a variable critical temperature depending on the oxygen content. For the optimal doping (x=0), the lattice parameter of the unit cell are a=0.382nm, b=0.389nm and c=1.169nm [52]. Compared to low temperature superconductors, $YBa_2Cu_3O_{7-x}$ has a very short coherence length which makes the device down scaling even more difficult. Hence, defects such us, impurities or grain boundary have a large impact in the transport properties. Another challenge for micro and nano device fabrication is the oxygen out-diffusion induced by for example a high temperature which will results in a change of superconducting proprieties dramatically. In this thesis YBCO nano-bolometers are fabricated, characterized and analyzed.

Chapter 3

MgB_2 HEB mixer and $YBa_2Cu_3O_{7-x}$ microbolometer fabrication process

The fabrication of nanometer scale devices is always challenging especially if those are made from materials which are very sensitive to the environment. Therefore, the development of reliable fabrication process is crucial in order to get high yield and high reproducibility. The high chemical instability of the MgB_2 and $YBa_2Cu_3O_{7-x}$ (YBCO) superconductors becomes a relevant issue especially for the nanostructures realization. Indeed, it has been demonstrated that MgB_2 degrades when it is exposed to the water and oxygen [87,88] while for YBCO most of the degradation comes from oxygen-out-diffusion. Moreover, one should point out that YBCO, due to its very short coherence length, is also very sensitive to defects and disorder. In this chapter, the development of MgB_2 and YBCO nanobolometers process is presented. The nanofabrication process was initially developed for MgB_2 HEBs, however later, due to the successful results, it was also applied to YBCO with some modifications.

3.1 Substrate selection and material growth

In this work MgB_2 films were grown on c-cut sapphire substrates via molecular-beam epitaxy (MBE) at NTT Basic Research Laboratories. Magnesium (Mg) and Boron (B) were evaporated using e-guns and the growth temperature measured at the backside of the substrate holder was 300 °C. The critical temperature, T_c was 25 K, 23 K and 19 K as measured in the continuous 30 nm, 15 nm and 10 nm films, respectively. More details about the film deposition are presented in [89,90].

This paragraph is focused on the YBCO growth technique. Thin YBCO films were deposited in house in a state of the art cleanroom. The deposition of YBCO thin films is not straightforward, thus because of its very compli-

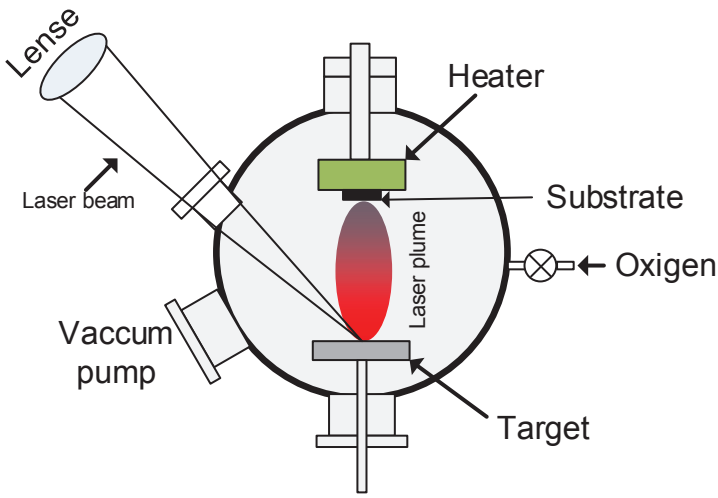

Fig. 3.1: Schematic of pulsed laser deposition (PLD)

cated crystal structure, it is rather difficult to get the correct stoichiometry in the films. Many parameters need to be optimized in order to grow epitaxial film with high-Tc. In particular, it is of extremely importance the deposition temperature and the oxygen pressure which defines the oxygen doping in the film. Thin YBCO films with a thickness of about 70 nm were deposited using pulsed laser deposition (PLD) technique. In figure 3.1 a setup of the PLD machine is shown. High power pulsed beam from Excimer KrF laser is focused inside the vacuum chamber through a lense. The target material (in this case $YBa_2Cu_3O_{7-x}$) is ablated and a plasma plume is formed depositing a thin film in the substrate. In order to grow high quality films, the substrate choice is also of extreme importance. The epitaxial growth requires matching of the film with the substrate. Hence, the better the match with regard to lattice parameters, atomic positions, crystallographic orientation, etc, the better is the epitaxial growth. However, an ideal substrate do not exist, thus some specific applications require a trade off between different substrate parameters. The YBCO film has a good lattice matching with $SrTiO_3$ (STO) and $LaAlO_3$ (LAO) substrates. Therefore, the lattice misfits (δ) of these substrates with YBCO are 2% for STO (tensile stress) and -0.7% for LAO (compressive stress) [91]. Nevertheless, the discussed substrates are not transparent to the THz radiation, moreover their dielectric constant (ϵ=277 for STO and ϵ=23 for LAO), far from the one of silicon (Si), makes them not suitable for the backside illumination of the YBCO detector at THz frequencies. In this work dual-side polished R-cut sapphire (Al_2O_3) was used as substrate material for YBCO deposition. Al_2O_3 substrate is transparent to THz radiation [92] and it has low tangent loss and a dielectric constant suitable for integration with

Table 3.1: Buffer layer deposition parameters

Parameters	CeO_2
Substrate Temperature	750 °C
Gas Pressure	0.1 mbar
Argon Flow	100 %
Oxygen Flow	25 %
RF Source Power	50 W
Target to Substrate Distance	30 mm

Si lens [91]. The drawback is that Al_2O_3 reacts chemically with YBCO, hence because of this and because of the large lattice misfit ($\delta = -9.4\%$) a buffer layer is required to accommodate the film to the substrate. In this work, CeO_2 buffer layer was used to passivate the Al_2O_3. The deposition system (DCA instrument) used in this work consisted of three chambers, two of them were dedicated to the RF sputtering of metals and oxides while the third chamber was dedicated to YBCO growth only. In-situ deposition of different materials was possible since the three chambers were connected between each other through a buffer line in which the base pressure was kept at 10^{-7} mbar.

Since the substrate cleanliness has a substantial influence on the film growth and adhesion, it is of great importance to clean it properly before start the deposition. Al_2O_3 substrate was cleaned in ultrasonic bath using warm acetone and isopropanol. Residuals of solvents were removed with deionized water and dried with nitrogen flow. At this stage the sample was mounted (with face down) in a sapphire substrate holder and transferred in the oxide chamber. CeO_2 buffer layer with a thickness of 25-30 nm was sputtered at substrate temperature (deposition temperature) of 750 °C and at gas pressure of 0.1 mbar. The oxygen pressure in the chamber was increased to 750 mbar directly after the deposition and the substrate was cooled slowly down at room temperature with a rate of 10 °C/min. Parameter details of the buffer deposition are given in table 3.1. After reaching the room-temperature, the sample was transferred inside the PLD chamber for the YBCO deposition. The YBCO was deposited at temperature ranging from 780 °C to 855 °C and at oxygen pressure of 0.6 mbar. Pulses from excimer KrF laser (wavelength 248 nm) were collimated into the rotating YBCO target with a energy density (J) of $1.6\,J/cm^2$. At this state the YBCO has a tetragonal structure which become orthorhombic when the oxygen pressure inside the chamber is increased to 860 mbar and the sample was cooled down to 550 °C and annealed for 60 minutes. The phase transition between tetragonal to orthorhombic is due to the oxygen atoms which diffuse into the film and feel the oxygen vacancies. Afterwards, the samples was transferred in the metal chamber and 20 nm $in-situ$ gold (Au) layer was deposited. The Au layer was necessary to protect the film during the bolometers patterning as well as to improve the contact resistance between the YBCO and the Au. In table 3.2, YBCO deposition parameters are given. Another important parameter, which it is listed in the table, is the target-to-substrate distance which provides proper position of the substrate in the plume to maintain the correct stoichiometry in the film.

Figure 3.2 shows the R-T curves of 70 nm YBCO films grown at different

Table 3.2: YBCO growth parameters

Parameters	YBCO
Deposition Temperature	780 °C to 855 °C
Oxygen Gas Pressure	0.6 mbar
Energy density	1.6 J/cm^2
Target to substrate distance	53 mm
Annealing Temperature	550 °C
Annealing Time	60 minutes
Annealing oxygen pressure	860 mbar

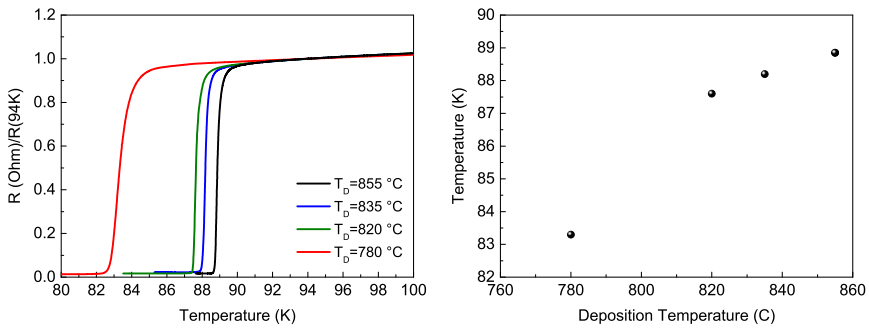

(a) (b)

Fig. 3.2: (a) Resistance (normalized to the resistance at 94 K) versus critical temperature of the YBCO films growth at different deposition temperatures. (b) YBCO films critical temperature versus deposition temperature.

deposition temperatures. As it is shown in figure 3.2(b), higher growth temperature lead to a higher critical temperature in the film. The films surface morphology (and other parameters) was not investigated in this work, however good film homogeneity can be linked to the transition width between the normal state and the superconducting state [93]. From figure 3.2(a), the good films homogeneity is confirmed by the sharp transition width which is less than 1 K even for the film with lower critical temperature. Despite the films showed good superconducting quality, they were used at room-temperature for the fabrication of THz microbolometers. Since, the YBCO films were covered by the gold, which was shunting the YBCO resistance, it was not possible to extrapolate the room-temperature coefficient of resistance (TCR). Nevertheless, based on the results of [Paper E], there was highly confidence for very similar TCR. The results of the microbolometers fabricated out of the films presented in figure 3.2 are reported in [Paper G].

3.2 UV-Lithography process

Devices with different bolometer area have been fabricated using both UV and e-beam lithography process. In this section details about the fabrication process based on the UV-lithography are presented while the one based on the e-beam lithography process is presented later in the chapter. It is important to underline that the processing (UV and e-beam lithography) was developed with the aim to reduce as much as possible the number of processing steps involved and thus to have as less as possible interaction between the films and the environment and more reproducibility. Bolometers were fabricated on 30 nm, 15 nm and 10 nm thick MgB_2 films and 70 nm thick YBCO films. As previously discussed all films were covered with 20 nm gold layer.

This section will be structured as following: the MgB_2 HEBs processing is explained and then, at the end of the section, the modifications applied for the fabrication of YBCO bolometers will be pointed out (the same will be done for e-beam lithography process). The fabrication of the MgB_2 HEBs consisted on several processing steps, as follows:

- **HEB length definition:** The first step was to define the bolometer length by using image reversal resist followed by the deposition of a Ti/Au (5 nm/350 nm) metal stack and subsequent lift-off. (see fig. 3.3 (b)).
- **Etching**: The $in-situ$ 20 nm thick gold layer over the bolometer bridge was etched via Argon ion milling. This step was quite critical, since a too short etch might leads to residues of gold over the bolometer, whereas a too long etch could damage the MgB_2 film (see fig.3.3 (c) and (d)). The ion milling parameters and the etching rate of the gold were carefully optimized to minimize any damages. Beside this, by probing test structures, adjacent to the actual bolometer area, it was possible to control the etching of the 20 nm gold layer.
- **Antenna and HEB width definition:** In this step the spiral antenna, in which the inner part corresponds to the bolometer width, and chip frames were defined using positive photoresist. The chip frames allowed to keep the bolometer short circuited once the antennas were fabricated (see fig.3.3 (e)).
- **Etching and final device:** The resist over the antenna and the chip frames was used as etching mask to protect the patterns during the etching. The thick gold layer as well as the MgB_2 film were etched down to the substrate via Argon ion milling (see fig.3.3 (e) and (f)).
- **Dicing**: In order to perform the DC and RF tests, the wafer was cut along the chip frame lines into chips of size 1.5×3.8mm.

The fabrication process sequences are shown in 3.3. Figure 3.4 shows a scanning electron microscope (SEM) image of an bolometer integrated with spiral antenna completely made using the UV-lithography, lift-off and ion milling process.

Several problems have been found during the fabrication of MgB_2 HEBs. In addition to the film degradation during processing steps, it was found that

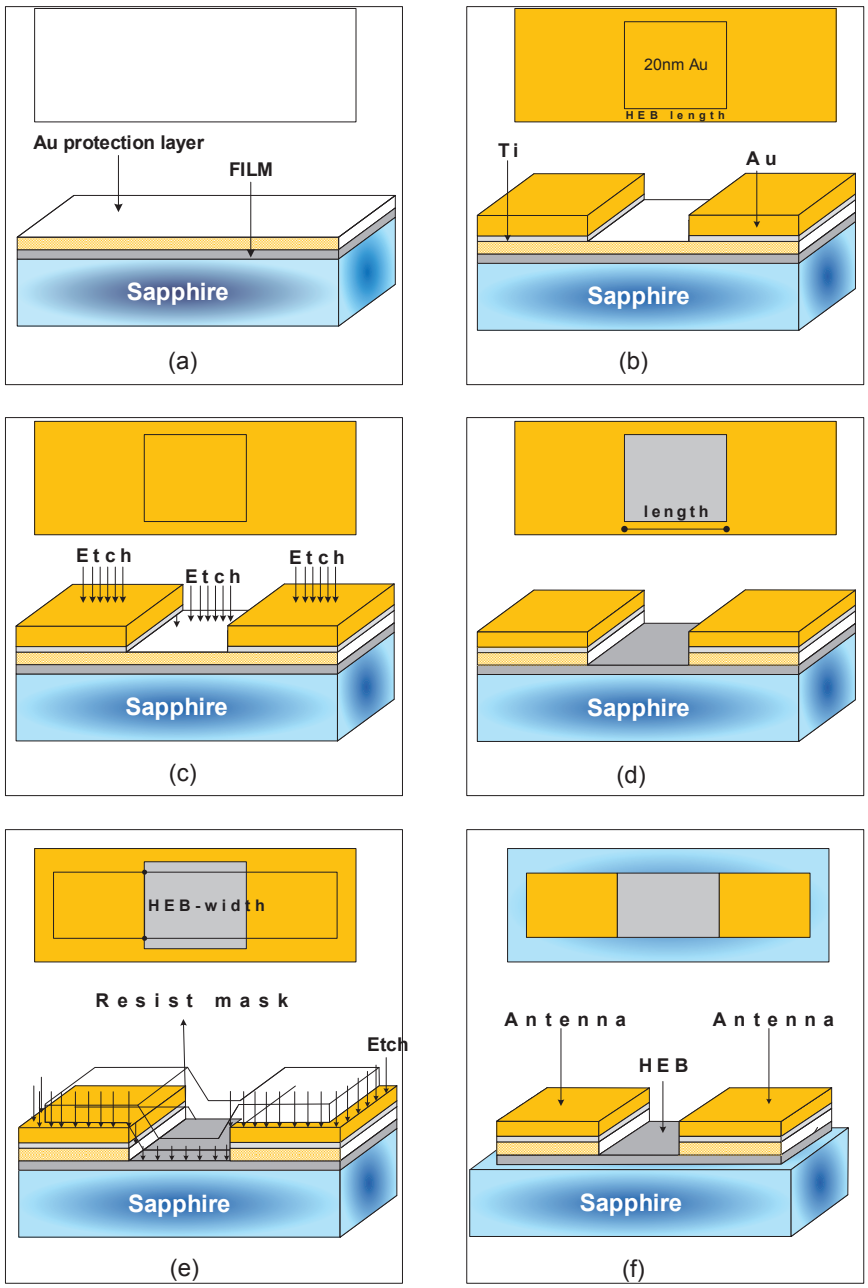

Fig. 3.3: Fabrication process sequences. (a) Wafer. (b) HEB length definition. (c-d) Etching of the thin layer of gold. (e) Antenna and HEB width definition. (e-f) Etching and final device.

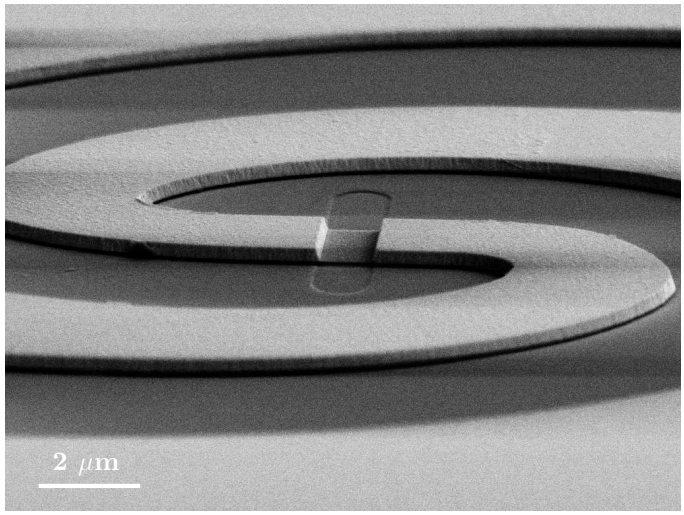

Fig. 3.4: SEM image of MgB_2 HEB integrated with spiral antenna (grey) on sapphire substrate (black)[Paper A].

the use of a carbon mask (deposited using Pulsed laser deposition and lift-off process) for defining the antenna pattern and the HEB width leaded to a low yield. After fabrication the devices showed very high impedance. Focused ion beam SEM (FIB-SEM) and SEM analysis were performed in the not working devices, revealing a physical disconnection between the bolometer and antenna pad. This is clearly visible in figure 3.5 and it was caused by the non uniformity in the carbon mask thickness along the wafer. However, these problems were solved using a resist mask, indeed the processing was more reproducible. The processing of YBCO bolometers was developed almost simultaneously with the one of MgB_2 based devices. The resist types and machines used in the cleanroom were the same. However, the order of the processing steps were different. First the antenna (the antenna inner part corresponds with the bolometer width) was defined using image reversal resist followed by evaporation of Ti/Au (5 nm/350 nm) and deposition of carbon. After lift off, the thin gold layer and the YBCO were etched in the region not protected by the carbon. After removing the carbon, a second lithography, using positive resist, was needed to define the bolometer length and the same resist was used as etching mask. The final step was to etch the thick metal stack in the region not protected by the resist (bolometer bridge) with Argon ion milling. However, this processing was quite unstable. The main problem was the last ion milling etch, indeed the etching of different metals with different thicknesses and etching rate was difficult to control and thus, not very accurate. Because of this, lately the same MgB_2 process was applied to YBCO.

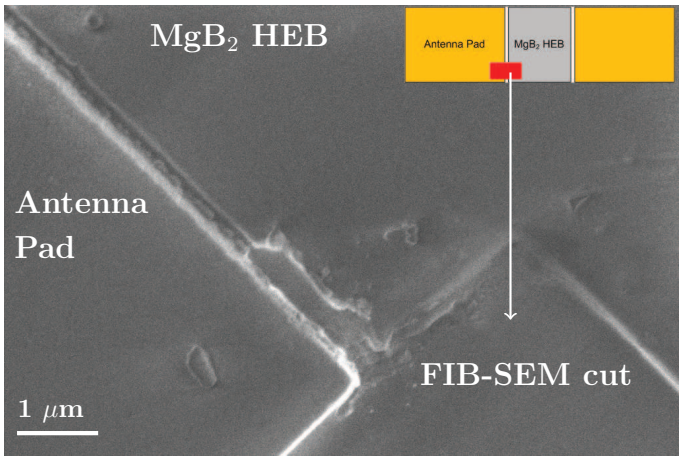

Fig. 3.5: SEM image of the HEB performed after the FIB-SEM analysis. The image clearly shows that the bolometer is disconnected from the antenna pad.

3.3 Electron beam lithography process

In order to improve the performances of both MgB_2 and YBCO bolometers submicrometer devices have been fabricated employing electron beam lithography. The local oscillator power requirement for HEB mixers scale with the bolometer area. Thus to push HEB mixers towards higher operation frequency, where the power availability is lower, smaller devices were fabricated. The device scaling was also beneficial for YBCO room-temperature bolometers, indeed great improvement of the sensitivity was observed when going to sub-micromiter sizes [Paper F,G].

The fabrication of the bolometer was done by several electron beam lithography steps and lift off process as follows:

- **Alignment marks and chip frames**: First, the alignment marks and the chip frames were fabricated. The alignment marks were needed in order to align the patterns of subsequent processing steps. The chip frames allowed to keep the bolometers short circuited once the antennas were fabricated. This avoids possible electrostatic charge that can permanently damage the devices. After the lithography, metals deposition (Ti/Au) and lift off were performed.

- **Contact pads**: The device fabrication started with the patterning of contact pads which defined the bolometer length. At this stage Ti (10nm), Au (100nm) and Ti (30nm) were deposited. The top Ti layer was used to protect the pads during the final ion milling step (see 3.6(a)).

- **Antenna**: The antennas were patterned in this step and Ti (10nm), Au (250nm) and Ti(30nm) layers were used for the metallization of the antennas. The top layer of Ti was deposited for the same purpose in the previous processing step. The center part of the antenna had an overlap with the contact pads (see 3.6(b)).

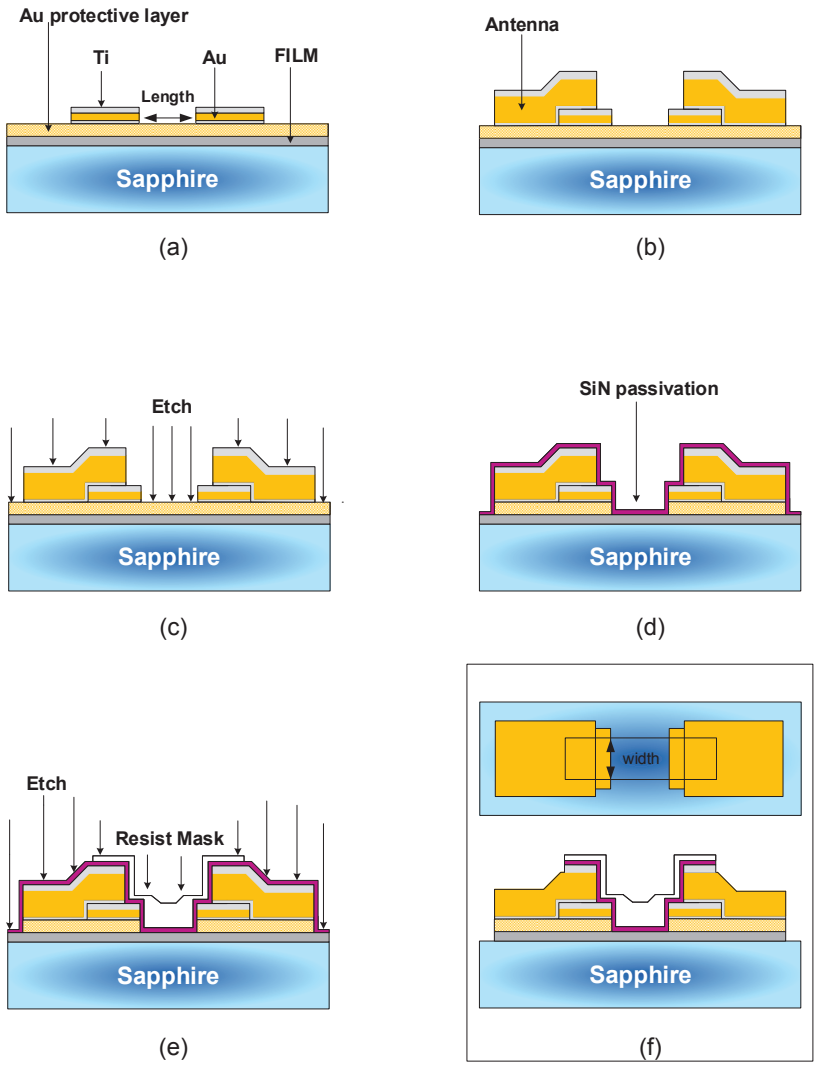

Fig. 3.6: Fabrication process sequences: (a) Contact pads. (b) Antenna. (c-d) Etching of the thin layer of gold and passivation. (e) Bolometer mask and etching. (f) Final device.

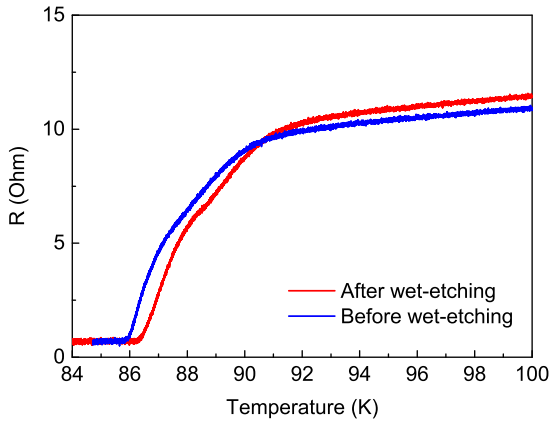

Fig. 3.7: R-T curves of an YBCO film before and after a wet-etching test.

- **Etching and passivation**: At this stage the 20 nm thick $in-situ$ Au layer was etched away using Argon ion milling. To prevent the degradation of the MgB_2 film during the rest of the processing steps, immediately after the etching, the devices were passivate by 40 nm thick SiN_x film. The SiN_x film was deposited $ex-situ$ using RF magnetron sputtering see (see 3.6(c-d)).

- **Bolometer mask and etching**: Negative e-beam resist was used as etching mask in order to define the bolometer width. Subsequently, the SiN_x passivation and MgB_2 film were etched in the regions not protected by the resist[1](see 3.6(e-f)).

Finally, a diamond saw was used to cut the wafer along the chip frame lines into chips of size 1.5×3.8mm. The fabrication process sequences are shown in figure 3.6.

The process described above was developed for MgB_2 bolometers but it was applied for the fabrication of YBCO microbolometers as well. However, this process had some issues when it was tested to fabricate YBCO nanostructure. Hence further optimization was required. Despite both the ion milling (to etch the thin layer of gold) and the RF sputtering (to deposit SiN_x passivation) were very carefully calibrated, a strong degradation of the initial quality of the film was observed in the final devices.

The devices showed better performance when they were not passivated and when the gold layer on top of YBCO was removed by wet-etching with a solution of KI:I[2] and water (just 8 s were necessary to remove 20 nm of gold). In order to be sure that the acid solution was not interacting with YBCO film a simple test was performed. The R-T curve of a continuous film was measured before and after the sample has been dipped inside the acid solution for about two minutes. The results of this experiment are shown in figure 3.7. As it

[1]The antenna was not damaged by the etch thanks to the Ti layer deposited in the first and second step.

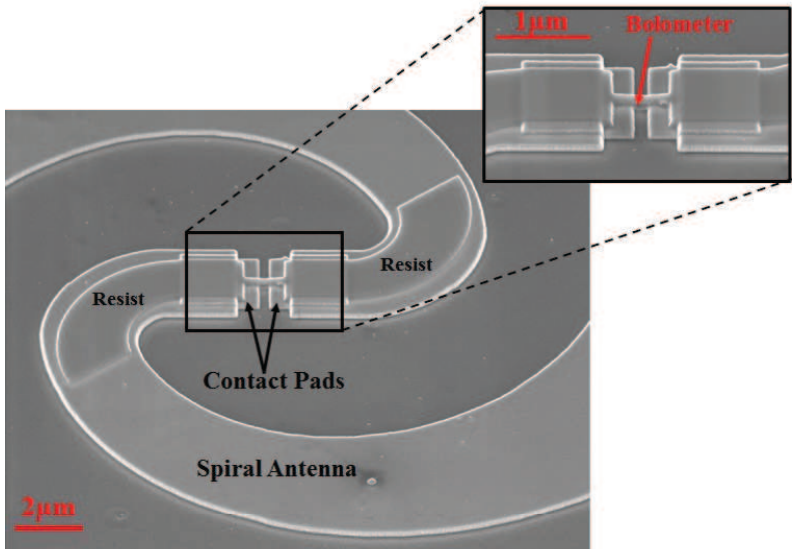

Fig. 3.8: SEM image of 300 nm^2 YBCO bolometer integrated with spiral antenna [Paper G].

is possible to see from R-T curves, no degradation of the critical temperature and the superconducting transition width was obverted indicating that the acid solution should not affect the film quality. The discrepancy between the two measured curves could be due to some uncertainty during the measurements.

Figure 3.8 shows the SEM image of a YBCO bolometer integrated with spiral antenna. In the upper right corner a magnification of the antenna inner part with the bolometer is given. The resist was left on top of the device to create a sort of passivation layer.

Chapter 4

THz characterisation of MgB_2 Hot-Electron Bolometer

In this chapter, the gain bandwidth and the noise temperature of the MgB_2 HEB mixers were studied in a number of devices with different areas and films thicknesses with a large variation of the critical temperature. The objective was to study the IF bandwidth as a function of the film thickness and the critical temperature as well as to study the noise temperature versus devices dimensions, critical temperature and local oscillator (LO) power. Experiments were mainly performed at 0.6 THz and 1.6 THz LO frequencies across various bias conditions. In order to understand the time constants which influence the electron temperature relaxation time; the gain bandwidth experimental data were analyzed using the two-temperature model (2-T model). The electron-phonon interaction time and the phonon escape time were extrapolated from the model as a function of the MgB_2 film thicknesses and the critical temperatures. From the 2-T model analysis, future device performances were predicted.

Results presented here have been published in Papers [A]-[D].

4.1 DC characterisation

In this section the dc (direct current) results are presented and discussed. Important parameters for a HEB mixer are: the normal state resistance (R_n), the critical temperature (T_C), the superconducting transition width (ΔT_C), the residual resistance (R_{res}) and the critical current density (J_C). These parameters can be obtained with dc measurements. In this case a low dc voltage (voltage bias) was applied to achieve a current of $1\mu A$ through the device. The bias voltage was controlled to keep the bias current at the fixed $1\mu A$. For T_C and ΔT_C measurements the applied bias current has to be low enough not to effect the T_C and the ΔT_C. The chosen current was much lower than the critical current of the devices discussed here.

In order to measure the resistance versus temperature curve, the device

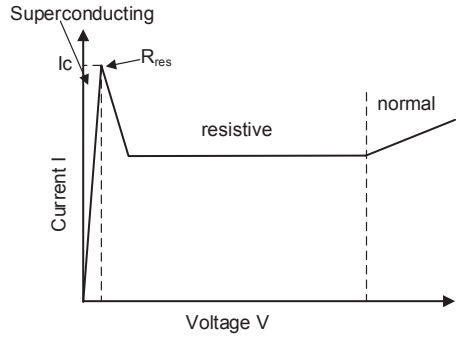

Fig. 4.1: Representation of a current versus voltage characteristic for a HEB at 4.2 K. The superconducting, resistive and normal state are shown.

.

Table 4.1: MgB_2 FILM THICKNESS (d), CRITICAL TEMPERATURE (T_c), TRANSITION WIDTH (ΔT_c), RESISTIVITY (ρ_{300}) AND RESISTANCE AT 300 K (R_{300}) [Paper C].

Device	Batch	d(nm)	Δ T_c(K)	T_c(K)	R_{300} (Ω)	$\rho_{300}(\mu\Omega \times cm)$
1	A	30	1	22	45	90
2	B	15	2	17	180	105
3	C	10	1.5	15	130	165
4	D	10	2	8.5	86	190
5	C	10	1.5	15	190	221

voltage was measured while it was cooled from the room temperature (300 K) to 4.2 K (LHe boiling temperature). At the temperature of 4.2 K, current-versus-voltage curve was recorded by swiping the voltage until the current exceeded the critical current, I_c. At this point by continuing increasing the voltage the device is first driven to the resistive state and then in to the normal state. Figure 4.1 shows a representation of a current-voltage characteristic for a HEB with the three states indicated. In this chapter devices from four batches are discussed. The film thicknesses, the critical temperature and the superconducting transition width as well as device parameters are listed in table 4.1.

As it was discussed in section 2.4, since the electron temperature relaxation time is dependent from the electron-phonon interaction time and the phonon escape time, thin films with a high T_c are preferable to get a wider gain bandwidth. While a sharp transition, (ΔT_c), between the resistive state and the superconducting state is needed for a high device gain (see equation 2.27).

Figure 4.2 shows resistance-versus-temperature curves of MgB_2 HEBs fabricated from films with thicknesses of 30nm, 15nm and 10nm. The critical temperature decreases with the MgB_2 thickness. The reduction of the critical temperature for thinner films can be possibly explained by a larger number of defects in thin films compared to thick ones. For example, devices from batches C and D made of 10 nm films show critical temperatures, T_c, of 15 K and 8.5 K,

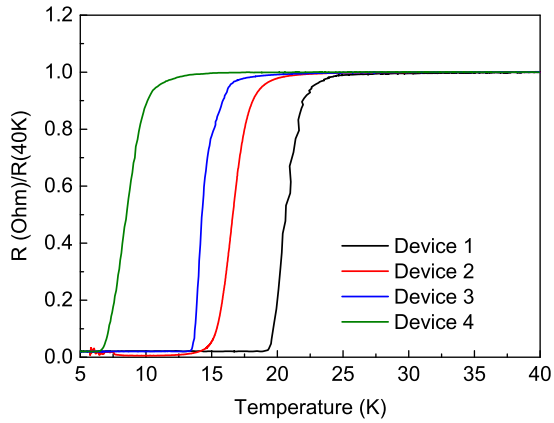

Fig. 4.2: Resistance versus temperatures curves (Normalized to the resistance at 40 K) of HEBs. Device numbers correspond to table 4.1. Device 5 is not given in the plot since it shows similar characteristic of device 3.

respectively. The lower critical temperature for batch D can be explained with the differences in the initial quality of the film. The MgB_2 room-temperature resistivity after the device fabrication ranged from $90\mu\Omega \times cm$ (30nm film) to $220\mu\Omega \times cm$ (10nm film). The sheet resistance ratio, R(300)/R(40), was approximately 1.3. The high resistivity together with the sheet resistance ratio indicate that the MgB_2 films are in the dirty limit [94]. High crystal quality of the films is linked to the film resistivity as well as to the critical current density. The high resistivity as well as the low critical current density of the fabricated devices suggest a low crystal quality of the films used in this work. I-V charac-

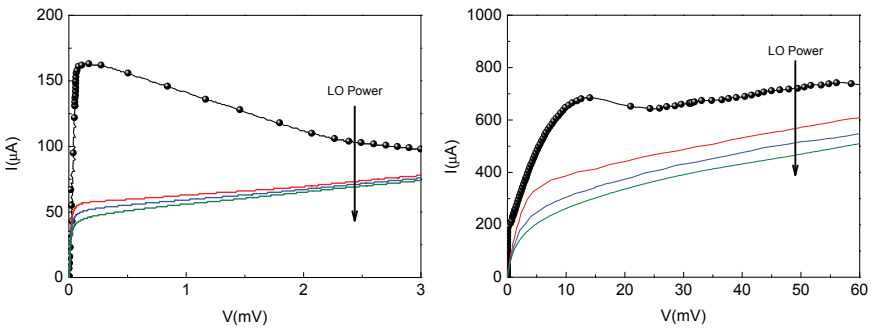

Fig. 4.3: (a) I-V curves of 1 μm × 3 μm (L×W), device 4. (b) I-V curves of 6 μm × 7 μm (L×W), device 5. HEBs at 4.2 K bath temperature, with LO power and without LO power applied.

teristics (with and without the local oscillator (LO) power applied[1]) of MgB_2 HEBs 4 and 5 with dimensions of L=1 μm × W=3 μm and L=6 μm × W=7 μm, respectively, are shown in figure 4.3. The room temperature resistance of these devices are R_4(300K)=86Ω and R_5(300K)=190Ω whereas the resistivity of the bridges are ρ_4(300K)=190$\mu\Omega \times cm$ and ρ_5(300K)=221$\mu\Omega \times cm$. The critical currents, measured at 4.2 K, were 160μA (device 4) and 650μA (device 5). The resulting critical current densities are 0.55 MA/cm^2 and 0.93 MA/cm^2, respectively.

4.2 Experimental technique for THz mixer characterisation

In this section the experimental technique used for the characterisation of the MgB_2 mixers at THz frequencies is described. The goal here was to measure the gain bandwidth and the noise temperature of a large variety of HEB mixers fabricated from different film thicknesses with different critical temperatures. A preliminary estimation of the local oscillator power requirement is also presented.

An overview of different THz sources that can be used as local oscillator will be also briefly discussed.

4.2.1 Quasi-optical Coupling

In order to couple THz radiation ($\lambda \approx 1mm - 100\mu m$) into the HEB (micrometer or nanometer dimensions) a feed antenna is needed. The antenna can be a machined waveguide or fabricated using lithographic process.

A good coupling efficiency and a well defined beam pattern is provided when using machined waveguides. The radiation is focused into a feedhorn from where it is coupled into the waveguide. The feedhorn provides an impedance transformation from the characteristic impedance of the free space to the impedance of the waveguide. The frequency range at which the waveguide can provide good coupling of the radiation to the detector that is placed across the waveguide, is defined by its geometry. The waveguide geometry is chosen in such way that the impedance mismatch between the waveguide and the detector is reduced as much as possible in order to reduce losses. Using a tunable element (called back-short), the matching can be optimized, however some losses can be still present due to air-gaps between the tunable element and the waveguide walls. The drawback of using machined waveguide is that at higher frequencies (above 1THz) waveguide machining becomes more complicated since their dimensions scale with the wavelength. Thus the fabrication of high quality waveguides becomes very challenging. Another drawback is that as the frequency scales up and the wavelength scales down the thinner and thinner substrates are required for the detector to which the radiation is coupled. To make thinner substrate a postprocessing is required which may lead to a low device yield despite the fact that device handling becomes more difficult.[2]

[1] The I-V with LO power applied where recorded during the RF measurements.

[2] The substrate shall be no thicker than $\lambda_{wg}/10$, where λ_{wg} is the wavelength in the

Planar antenna that is lithographically made and directly integrated with the device on a dialectic substrate provides a large RF bandwidth. Hence devices can be tested in a wider frequency range compared to the waveguide type. Besides, the fabrication of planar antenna is cheaper, easier, robust and more accurate especially at high frequencies and does not require postprocessing. The quasi-optical coupling was used in this work because of a larger flexibility compared to the waveguide coupling.

Antenna placed on a dielectric substrate has a fundamental property that it couples primarily into the dielectric rather than into the air. The ratio between the power transmitted into the dielectric and into the air is $\varepsilon^{3/2}$, where ε is the dielectric constant of the substrate [95]. This effect is more pronounced when a substrate with a high dielectric constant, such as Si, is used. However, a special substrate geometry is needed in order to get a high coupling efficiency (see fig.4.4). If the substrate is simply a plane wafer then any radiation from the antenna at angles larger than the critical angle[3] is trapped in the substrate. To solve this problem a dielectric lens can be used. Types of lens substrates used for receiver applications are hyperhemispherical and elliptical. The hyperhemispherical is a hemispherical lens which has an attached extension length, R/n, where R is the radius and n is the refractive index of the lens. The hyperhemisherical lens directs the beam irradiated from the integrated antenna towards the broadside direction, sharpening the pattern and increasing the gain of the integrated antenna by n^2 [95]. In this work elliptical Si lenses were used that is the beam is diffraction limited by the lens aperture and can be made very narrow. Hence it is more practical for laboratory studies since no extra optical elements are needed in contrary to the hyperhemispherical lens.

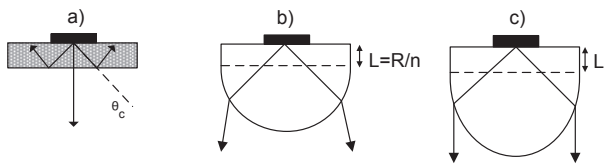

Fig. 4.4: Substrate geometries. a) Plane wafer (no substrate lens). b) Hyperhemispherical lens. c) Elliptical lens (Figure adapted from [95].)

Use of hybrid antennas could result in losses caused by the reflections of radiation at the lens/air interface as well as the losses due to the absorption in the lens material. The losses due to the reflection at lens/air interface could be reduced by placing an antireflection coating [97]. In this research, self complementary spiral antennas placed on sapphire substrates were used. Such antenna belongs to the group of antennas whose impedance is real and it is constant in a wide frequency range [70][4]. In figure 4.5 the spiral antenna

waveguide. The reason for this is that thicker substrate could perturb the waveguide modes, or allow substrate modes with the consequence of the coupling efficiency reduction.

[3] θ_c=arcosin(1/n). Where θ_c is the critical angle and n=$\sqrt{\varepsilon}$ is the refractive index.

[4] The antenna impedance is: R_A=$Z_0\sqrt{2(1+\varepsilon)}$. Where Z_0 is the impedance of the free

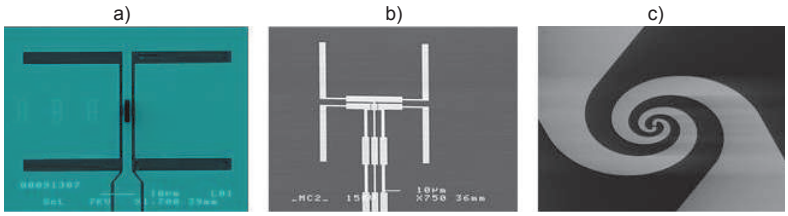

Fig. 4.5: a) Pictures of the double slot antenna [18]. b) The double dipole antenna [96]. c) The spiral antenna (Paper [C]).

along with two others commonly used for HEBs three are shown. The inner and outer diameters define the higher and lower cutoff frequencies, respectively.

4.2.2 THz sources

THz sources used in this work to measure the performances of the MgB_2 HEBs were: backward-wave oscillators at 600 GHz [98] and far infrared (FIR) gas laser at 1.6 THz [99]. Despite these sources offer quite high output power, they are also very bulky and expensive, which makes them not suitable for ground-based observatory and undesirable for space-borne applications. Nevertheless, discussed sources are convenient for laboratory set-ups where compactness is not really a requirement while high output power simplifies the local oscillator schemes and allows for large power variations.

Nowadays, intense research is ongoing in order to build high output power, compact, inexpensive and light THz sources. Figure 4.6 shows the state of the art THz sources plot, in particular the output power as a function of frequency is given. At frequencies below 100 GHz most common sources are

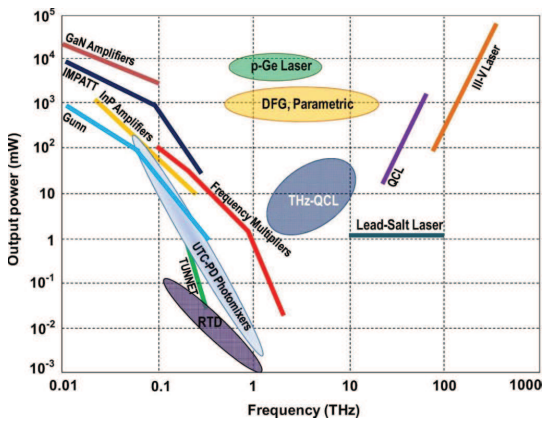

Fig. 4.6: THz sources output power as a function of the frequency [100].

oscillators, amplifiers, p-i-n diodes etc; above 10 THz QCLs, optically pumped

space.

sources are commonly used, offering high output power. In the THz region solid-state electronic frequency multipliers as well as QCLs and others such as HEMT, HBT and Gunn-diode oscillators are constantly progressing technologies. Despite all the sources discussed above are very useful for some applications, they have some limitations. For example QCLs require cooling, and they have problems with frequency instability, lifetime and bandwidth tuning, while solid-state frequency multipliers can work up to 2.7 THz [101] producing tens of microwatts of power. In conclusion, a lot of work has to be done in order to develop compact, inexpensive sources that can offer high output power at THz frequencies.

4.2.3 RF measurement setup

In order to perform RF measurements, MgB_2 HEBs were mounted on the backside of an elliptical silicon lens defining the quasi-optical setup previously described. The lenses used during all the experiments reported in this thesis were without antireflection coating[5]. The lens with the attached device was then placed in a detector block which was than fixed on the plate of a LHe vacuum cryostat as shown in figure 4.7 (4.2 K bath temperature). The cryostat has a vacuum chamber equipped with two metal heat shields: at 4.2 K and at 77 K. At the 4.2 K and 77 K shields three sheet filters (Zitex G108 IR filters) were installed. The bath temperature can be reduced to 2 K by lowering the vapor pressure above the liquid helium (LHe) using a vacuum pump. Figures 4.7 and 4.8 show the cryostat interior where THz mixer is sitting and the experimental setup used for the gain bandwidth measurements. The device gain bandwidth was measured using two backward wave oscillators (BWOs) as a signal source and a local oscillator (LO) at 600 GHz. The LO was kept at constant frequency, while the frequency of the signal was tuned. The amplitude of the signal, at each frequency point, was modulated by a mechanical chopper (chopping frequency 18 Hz). Both LO and signal beams were focused by Teflon lenses and mixed by a thin film (Mylar^{TM}) beam splitter. The mixed beam was fed into the cryostat through the window. Inside the cryostat the mixer block was connected to a broadband bias-T. Outside the cryostat two room-temperature amplifiers (0.1-12 GHz) were used to amplify the IF signal which power and frequency were then measured by a microwave spectrum analyzer. A Lock-in amplifier was used to read-out the direct detection signal via the mixer bias line, which was later used for the calibration of the signal input power (This is only valid for small variation of the signal power).

The mixers noise temperature was measured using the standard Y-factor technique with a room-temperature (290 K) and liquid nitrogen (77 K) black body load (Eccosorb sheets [102]). As a local oscillator sources both a 600 GHz BWO and 1.63 THz FIR gas laser were used. A set of cold and room temperature low noise amplifiers was used. The cold low noise IF amplifiers covering the frequency range of either 1-4 GHz or 4-8 GHz were placed in the cold plate of the cryostat and connected after the mixer via a semirigid coaxial cable. The input noise temperature of both IF amplifiers was approximately 3-10 K while the gain was approximately 30 dB. Two room-temperature amplifiers

[5] AR-coating materials are frequency dependent, and hence not so much flexibility is given during the experiment when lenses with AR-coating are used.

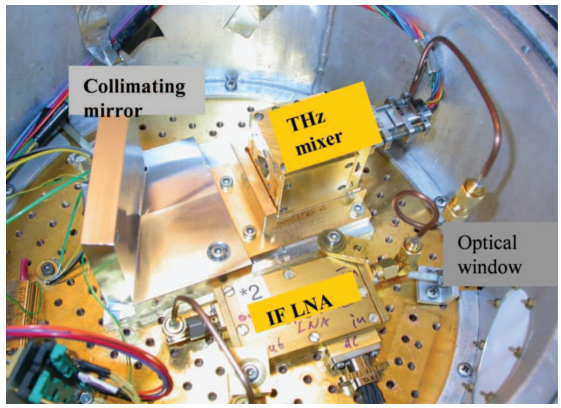

Fig. 4.7: Picture of the cryostat interior. The cryogenic low noise amplifier was disconnected for the gain bandwidth measurements (Paper [D]).

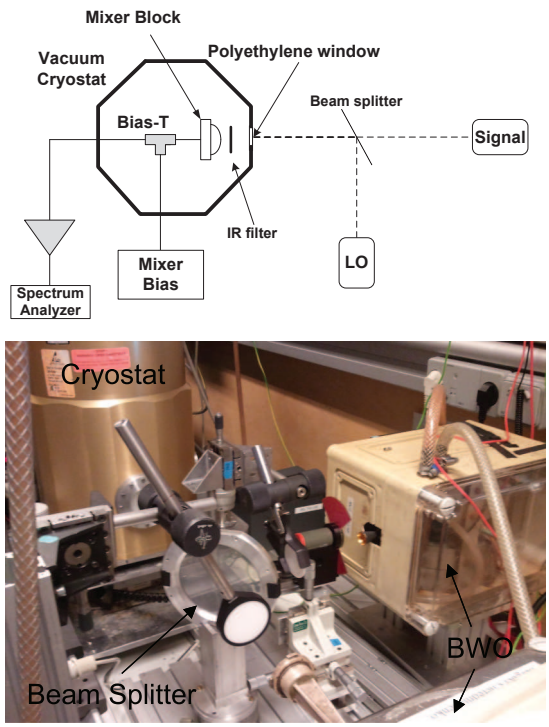

Fig. 4.8: The gain bandwidth measurement setup. Top figure: schematic representation of the setup and the cryostat interior. Bottom figure: picture of the setup with sources, optics and cryostat used.

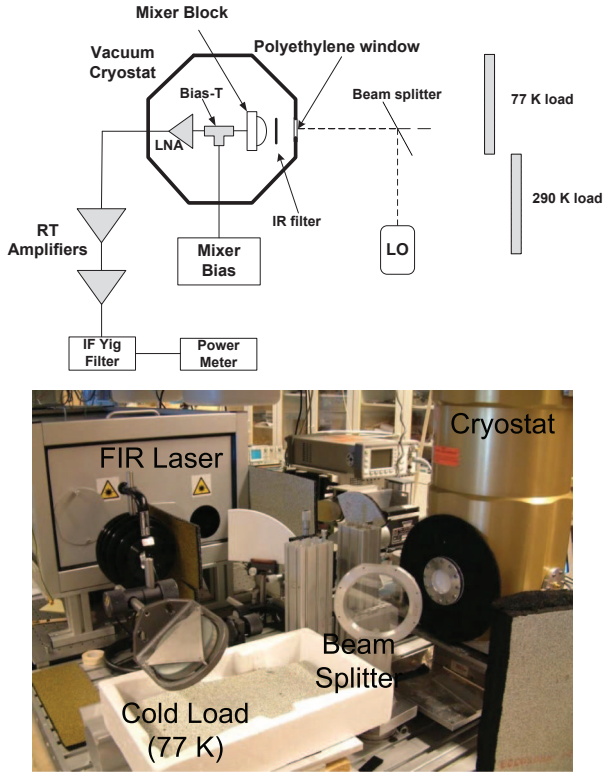

Fig. 4.9: The noise temperature measurement setup. Top figure: schematic representation of the setup and the cryostat interior. Bottom figure: FIR laser, hot and cold load optics and cryostat are visible.

outside the cryostat were used to boost the IF signal. The IF passband was set by a tunable (1-9 GHz) 50 MHz band pass filter (see fig. 4.9).

4.3 Gain bandwidth results

In chapter 2 it has been discussed that the IF gain bandwidth of phonon-cooled HEB mixers depends on several parameters such as film thickness, d, and critical temperature, T_c (see equation 2.41) as well as the speed of sound and the acoustic matching between the film and the substrate.

Since the electron-phonon interaction time is inversely dependent on critical temperature and the escape time is directly proportional to the film thickness, the objective here was to study the gain bandwidth as a function of the discussed film parameters. For this purpose, several HEBs were fabricated from different MgB_2 film thicknesses and critical temperatures. The gain bandwidth was also investigated for mixers having the same film thickness but different critical temperature. The MgB_2 film thicknesses were 30 nm, 15 nm and 10 nm while the critical temperature ranged from 22 K to 8.5 K (see table 4.2).

As it was explained in the gain bandwidth experimental setup, the IF response was measured at 600 GHz. Due to the large dimensions, mixers 1,

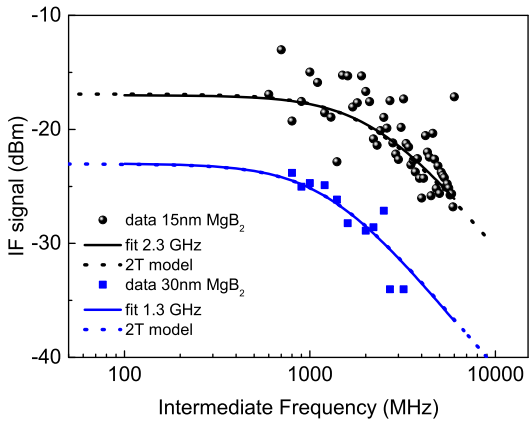

Fig. 4.10: Intermediate frequency response of MgB_2 mixers made of 15 nm (device 2) and 30 nm (device 1) MgB_2 films. Solid lines are fits to the experimental data using the single-pole Lorentzian equation. Dashed lines are results of the two-temperature model.

2 and 3 were heated to approximately 7-9 K, which is still much lower than the critical temperature of these mixers (see table 4.2). The bias voltage was optimized for the maximum IF signal (i.e. the mixer conversion gain). The IF response as a function of the intermediate frequency of the mixers fabricated from 30 nm (lower curves, device 1) and 15 nm (upper curves, device 2) MgB_2 films is given in 4.10. Figure 4.11 shows the response of HEBs fabricated from 10 nm films.[6] The response of the device 4 (see table 4.2) shown in figure 4.11(b) was obtained from the Y-factor measurements using an expression P_{IF}=(P_{300}-P_{77})×η_m, where P_{300} and P_{77} are the IF power with 300 K and 77 K load, and η_m is the mixer gain.

The IF response calibration included the coaxial cables, the bias-T and the IF amplifier. There was no isolator inside the cryostat. Due to the HEB/IF chain impedance mismatch and other parasitics in the mixer unit, the IF response was disturbed by standing waves in the long cable inside the cryostat. This explains scattering of the experimental points in figure 4.10 and 4.11(a). Data scattering was not observed for the mixer shown in figure 4.11(b) simply because the IF amplifier was mounted much closer to the mixer block during the noise temperature measurements.

In order to determine the gain bandwidth (3 dB roll-off), the least square fit of the measured IF response (after the calibration for the IF amplifier transfer function) was performed with a single-pole Lorentzian (see equation 4.1) using the IF response at zero IF frequency ($\eta(0)$) and the 3 dB gain roll-off frequency (f_{3dB}) as fitting parameters.

$$\eta(f_{IF}) = \eta(0)[1 + (f_{IF}/f_{3dB})^2]^{-1} \tag{4.1}$$

The mixer time constant, τ was obtained as τ=1/(2π f_{3dB}). As it was discussed

[6]The RF results are referred to the devices presented in the DC characterisation section.

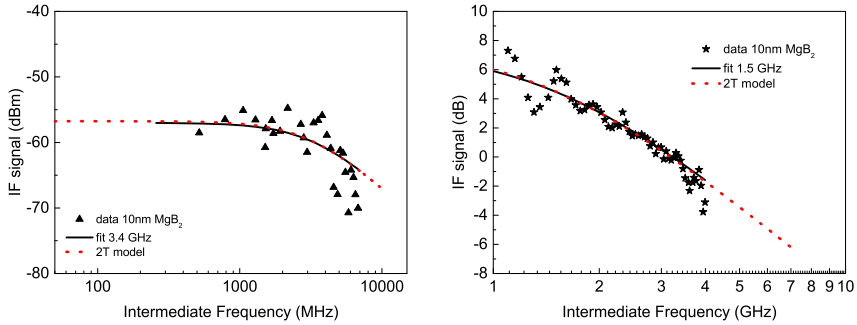

(a) (b)

Fig. 4.11: (a) Intermediate frequency response of MgB_2 mixers made of 10 nm (device 3) film. (b) Intermediate frequency response of MgB_2 mixers made of 10 nm (device 4) film.The solid and the dotted lines are the fit to the experimental data and the result of the two-temperature model.

Table 4.2: MgB_2 FILM THICKNESS (d), THE CRITICAL TEMPERATURE (T_c), THE ELECTRON-PHONON INTERACTION TIME (τ_{eph}), THE PHONON ESCAPE TIME (τ_{esc}), THE SPECIFIC HEAT RATIO (c_e/c_{ph}) AND THE MIXER TIME CONSTANT (τ). [Paper C].

Device	d(nm)	T_c(K)	$\tau_{eph}(ps)$	$\tau_{esc}(ps)$	C_e/C_{ph}	$\tau(ps)$
1	30	22	7±6	42±1	1.35	130
2	15	17	12±5	12±1	2.25	70
3	10	15	11±5	9±1	3	47
4	10	8.5	15±2	4.8±0.2	9	106

in chapter 2, the gain bandwidth depends on the HEB mixer bias point because of the electrothermal feedback that modifies the mixer time constant. The 3 dB gain roll-off frequency was 1.3 GHz and 2.3 GHz for devices fabricated from 30 nm and 15 nm film thicknesses. A GBW of 3.4 GHz was obtained for a mixer made of a 10 nm film with a T_c of 15 K. A smaller GBW, 1.5 GHz, was measured for a mixer fabricated from a film with the same thickness (10 nm) but with a lower T_c of 8.5 K. The summary of the GBW and the corresponding mixer time constant τ is given in Table 4.2.

These results clearly show dependence of the gain bandwidth on the thickness and the critical temperature of the film. In figure 4.12, the GBW and the critical temperature versus the film thickness for both MgB_2 mixers (Paper [B], Paper [C]) and NbN mixers (from the literature) are compared. The open symbols in figure 4.12(a) correspond to the GBW and critical temperature for MgB_2 mixer 4 (see table 4.2) while the solid line in the figure 4.12(a) is the fit to the experimental data. By comparing the gain bandwidth of the HEB mixers made from NbN and MgB_2 films, it is possible to see that already for 10 nm MgB_2 film a GBW as large as the one of HEB mixers made from 3.5 nm NbN have been demonstrated in this work. Thus, there is plenty of room for

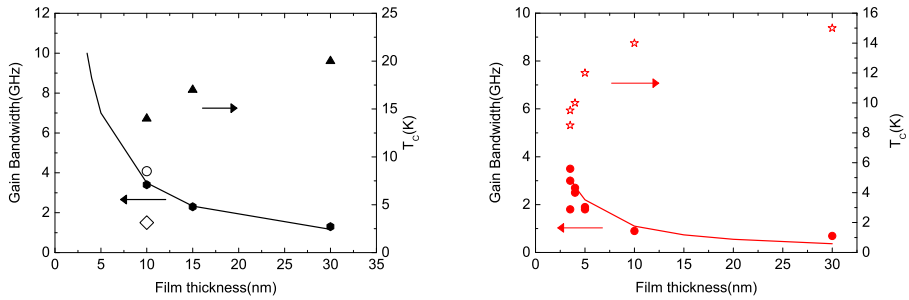

Fig. 4.12: (a) The gain bandwidth (circles) and the critical temperature (triangles) for MgB_2 HEB mixers versus the film thickness. The open circle and diamond points are the critical temperature and the gain bandwidth for mixer 4. (b) The gain bandwidth (circles) and the critical temperature (stars) for NbN HEB mixers versus the film thickness (from ref. [103]).

the improvement of the MgB_2 mixers performance.

In Paper [A], to estimate the GBW for thinner (3.5 nm) MgB_2 films, the fit for the GBW as a function of the film thickness was extrapolated using the same GBW versus thickness dependence as for thick films. A gain bandwidth as large as 10 GHz was estimated with 3.5 nm thick film, which is more than twice larger than the one for NbN film.

4.3.1 Gain bandwidth modeling

As it has been discussed and shown in the previous section the HEB response depends on several parameters, hence the study of the MgB_2 mixers made of different film thicknesses provides a good comparison of the physical parameters that determine the GBW. The two temperature (2-T) approach presented in [74] is a very good way of understanding the superconductor response on a modulation RF radiation. The discussed 2-T model has been used in the past for the modeling of the gain bandwidth for HEBs made from other materials e.g. NbN [103]. The objective here is to apply the 2-T model to MgB_2 mixers to verify that it is still valid for these new types of mixers and hence, extrapolate the time constants that influence the GBW. By knowing the time constants one can predict future devices optimization and performance.

The general approach was to apply 2-T model to the measured GBW data of MgB_2 HEBs made of 30 nm, 15 nm and 10 nm films. At a given mixer bath temperature, the LO power and the bias voltage were optimized for the largest IF signal. Under these conditions, due to the dissipation of the LO and dc power, the electron temperature, T_e, can be considered close the critical temperature, T_C. The phonon temperature, T_{ph}, was estimated to be around $0.9xT_e$ using the heat balance equations [104].

The effect of the self-heating electrothermal feedback was taken into account. According to [104] the HEB conversion gain as a function of the inter-

mediate frequency is given by:

$$\eta_{IF}(\omega) \propto 20lg\left|\frac{\eta(0)C_0}{\xi(\omega)+\frac{R_0-R_L}{R_0+R_L}C_0}\right| \tag{4.2}$$

$$\xi(\omega) = \frac{(1+j\omega\tau_1)(1+j\omega\tau_2)}{(1+j\omega\tau_3)} \tag{4.3}$$

$$\tau_3^{-1} = \tau_{esc}^{-1} + \tau_{eph}^{-1}\frac{c_e}{c_{ph}} \tag{4.4}$$

$$\begin{aligned}\tau_{1,2}^{-1} &= \frac{\tau_3^{-1}+\tau_{eph}^{-1}}{2}\times \\ &\times\left[1\pm\left(1-4\frac{(\tau_3^{-1}+\tau_{eph}^{-1})^{-2}}{\tau_{esc}\tau_{eph}}\right)^{1/2}\right]\end{aligned} \tag{4.5}$$

The electron specific heat is given by [105]:

$$c_e(T_e) = \gamma T_e \tag{4.6}$$

The published value of γ for MgB_2 is in the range from 3 to 5.5 mJ/mol K^2 [82, 106, 107]. The phonon specific heat, c_{ph} at an arbitrary phonon temperature can be calculated using the Debye approximation (eq. 4.7) [105].

$$c_{ph}(T_{ph}) = 9n_aK_B\left[\frac{T_{ph}}{T_D}\right]^3\int_0^{\frac{T_D}{T_{ph}}}\frac{e^x x^4}{(e^x-1)^2}\,\mathrm{d}x \tag{4.7}$$

Where $n_a = 3.54\times10^{22}$ cm^{-3} is the atomic mass density in MgB_2 calculated from the mass density ρ_m=2.7 g/cm^3 [82, 106] and the molar mass M=45.925 g/mol of MgB_2. The Debye temperature, T_D in MgB_2 was experimentally obtained to be in the range from 700 K to 1100 K [82, 106, 107], much larger compared to other intermetallic as well as cuprate superconductors. For the 2-T model simulations the mean values of the electron specific heat coefficient and the Debye temperature were taken into consideration.

Using the electron-phonon interaction time and the phonon escape time as fitting parameters the 2-T model was applied to the measured data. Dashed curves in figures 4.10 and 4.11 are the fits using 2-T model. In table 4.2, a summary of the electron-phonon interaction time and the phonon escape time obtained from the 2-T model as well as the specific heat ratio, obtained from equations 4.6 and 4.7 and the material parameters, are given. As expected, the phonon-escape time decreases almost proportionally with the film thickness while the electron-phonon interaction time and the specific heat ratio increases for thinner films due to the lower critical temperature.

In figure 4.13 the phonon escape time data, from this work and from the previous work [108], as a function of the film thickness are shown. Since the phonon escape time decreases with the film thickness it is clear that thin films will act towards the reduction of this time constant. Figure 4.14 shows the electron-phonon interaction time versus the temperature extrapolated for each film thickness. In the figure, data from this work (circles) and data from

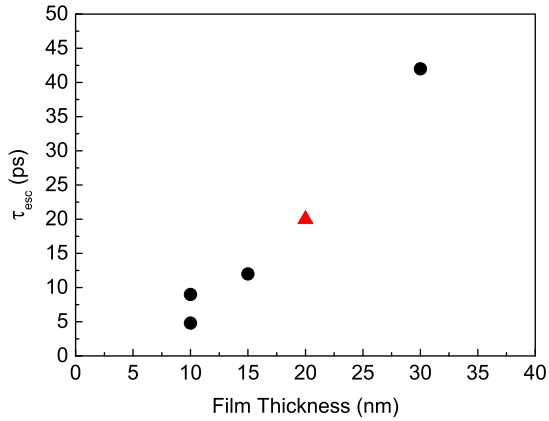

Fig. 4.13: Phonon escape time as a function of the film thickness, obtained from the gain bandwidth measurements and the 2T-model analysis. Circles: data from this work; the red triangle: from the previous work [108].

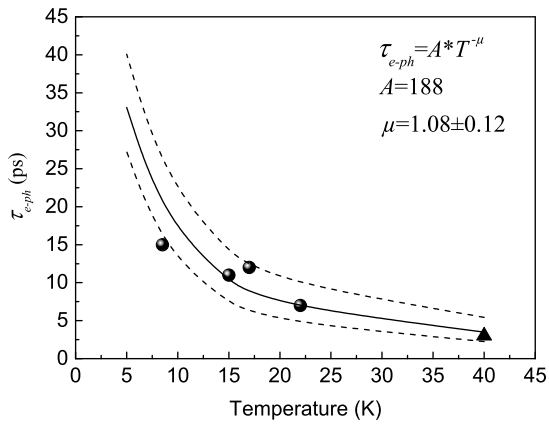

Fig. 4.14: Electron-phonon interaction time as a function of the temperature, obtained from the gain bandwidth measurements and the 2T-model analysis. Circles: data from this work; the triangle: from the literature [50]. The solid line is the fit to the data while the dashed lines show the estimated error margins.

.

the literature (triangle) are plotted together and fitted using the equation, $\tau_{e-ph} \propto T^{-\mu}$ with $\mu \approx 1.08$. In section 2.4, it was discussed that the value μ was measured for various materials in the range from 1 to 4. In this research for the first time this value was extrapolated for MgB_2 film using the 2-T model instead of rather complicated measurements. Hence, using equation $\tau_{e-ph} = 188 \cdot T^{-\mu}$ and $\mu \approx 1.08$, the electron-phonon interaction time could be estimated for various MgB_2 films with different critical temperatures.

In figure 4.15, the electron and phonon specific heat and the specific heat ratio are plotted as a function of the temperature. The specific heat ratio is another important parameter which influences the HEB relaxation time and thus the gain bandwidth (see section 2.4). In order to achieve short relaxation time (wide gain bandwidth) the electron-phonon interaction time, the phonon escape time and the specific heat ratio must be optimized.

Based on these simulations, it has been demonstrated that the 2-T model allows to analyze the experimental data for MgB_2 mixers. Therefore, this model is also valid for MgB_2 mixers. Moreover, within the 2-T analysis, it is clear from figures 4.14 and 4.15 that a larger GBW for phonon-cooled MgB_2 HEB mixers requires films with a high critical temperature T_c to minimize both the electron-phonon interaction time and the specific heat ratio. On the other hand the films must be also thin to ensure fast removal of the energy from the phonons (see 4.13).

Different GBW measured for mixers made of the same film thickness and with different critical temperature (device 3 and 4) can also be explained in the frame of the 2-T model. As it is possible to see from the Table 4.2, the electron-phonon interaction time and the specific heat ratio are larger for a device with lower critical temperature with the consequence of a larger relaxation time and smaller GBW.

In [81], using a different deposition method (HPCVD), it was reported that MgB_2 films (7.5 nm) with a critical temperature as high as 34 K can be made. Applying these films parameters to the 2-T model discussed above we obtained that a gain bandwidth as large as 13 GHz is achievable.

Following that very recently, a GBW as large as 7 GHz has been demonstrated for devices fabricated from 15 nm thick film with a T_c of around 38 K [109]. The discussed GBW is already more than twice larger than of the GBW that has been reported for NbN mixers made from 3-4 nm film 4.12(b).

These results confirmed what has been already predicted in this work for MgB_2 mixers fabricated on high quality films.

4.4 Receiver noise temperature characterisation

In order to determine the receivers noise temperature, the so called Y-factor technique was employed. The technique is based on measuring the output power of the receiver for two input loads.

Power emitted from a blackbody radiator per unit bandwidth, B, is a function of the temperature, T, of the blackbody and the frequency, f through the Callen and Welton law [110]:

$$P(f,T) = \left(\frac{hf}{e^{hf/k_B T} - 1} + \frac{hf}{2} \right) \cdot B \tag{4.8}$$

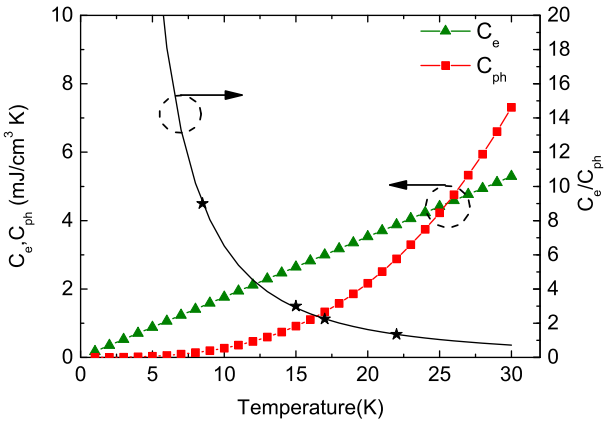

Fig. 4.15: Electron and phonon specific heats and the specific heat ratio as a function of the temperature for MgB_2. The c_e/c_{ph} ratio is plotted for the electron temperature equal to the phonon temperature. Filled circles indicate c_e/c_{ph} at the critical temperature of the films used in this work. c_e/c_{ph} are from equations 4.6 and 4.7.

.

where h is the Planck's constant.

The noise temperature of such blackbody is expressed by:

$$T^n(f,T) = \frac{P(f,T)}{k_B B} = \left(\frac{hf/k_B T}{e^{hf/k_B T} - 1} + \frac{hf}{2k_B T} \right) \tag{4.9}$$

If $hf \ll k_B T$ (Rayleigh-Jeans limit) the equations 4.8 and 4.9 can be approximated as:

$$P(f,T) = k_B T B \tag{4.10}$$

$$T^n(f,T) = T \tag{4.11}$$

The receiver output powers with a hot load, referred to the room temperature (290 K), and a cold load referred to the liquid nitrogen (77 K), are defined as:

$$P_{out,hot} = \eta k_B (T_{rec} + T(290K))B \tag{4.12}$$

$$P_{out,cold} = \eta k_B (T_{rec} + T(77K)B \tag{4.13}$$

Where η is the receiver gain. The Y factor is defined as:

$$Y = \frac{P_{out,hot}}{P_{out,cold}} = \frac{T_{rec} + T(290K)}{T_{rec} + T(77K)} \tag{4.14}$$

The double side band (DSB) receiver noise temperature then becomes:

$$T_{rec} = \frac{T(290K) - Y \cdot T(77K)}{Y - 1} \tag{4.15}$$

In figure 4.16 the DSB noise temperature versus the bias voltage and the I-V curves at different power levels are shown for a device of 10 nm film with a T_c

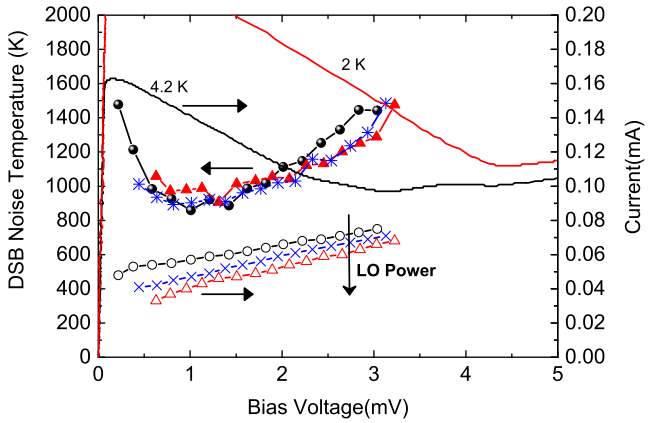

Fig. 4.16: Primary axis: DSB noise temperature as a function of the bias voltage. Secondary axis: I-V curves plotted at different LO power levels at 4.2 K. The unpumped IV at 2 K is also shown. The data in this plot are referred to device 4.

of 8.5 K (see device 4 in table 4.1). The receiver noise temperature had a broad minimum around 1 mV and 60 μA. Figure 4.17 shows the mixer noise spectra measured versus IF frequency in the range from 1 GHz to 4.5 GHz at 600 GHz LO frequency. The minimum receiver noise temperature was approximately 800 K corrected for the reflection losses at the silicon lens and including noise contributions from the LNA, the IR filter and the beam splitter. A noise bandwidth of 3 GHz was extrapolated from the fit of the measured data (solid red line fig.4.17). A 20% reduction of the receiver noise temperature was observed with the reduction of the bath temperature. Indeed, at 2 K the critical current of the device increased from 160 μA to approximately 250 μA (see figure 4.16). In order to bring the mixer to the same bias point a 50% larger LO power was needed and the noise temperature reduced as was previously discussed [73, 111]. The reduction of the noise when more LO power is applied to the HEB mixer is due to the improvement of the mixer gain at higher LO power level. It justifies the general tendency of the HEB mixers to show an improvement in performance for lower operation temperature and/or higher critical temperatures. Figure 4.18 shows the DSB noise temperature versus intermediate frequency for two devices made of the same film thickness (10 nm) but with different critical temperature (see device 4 and 5 in table 4.1). In the same plot, the noise spectra of a HEB mixer of 3-4 nm NbN film [18] is shown for comparison reason. Despite the mixer 5 was larger in size, compared to device 4, it was possible to pump it in the optimum bias (30 mV; 300 μA) point in which the noise temperature had a minimum. As it is possible to see from figure 4.18, MgB_2 HEB mixers are very close to the state of the art NbN HEB mixers even in terms of noise performance.

Another important figure of merit that characterises the HEB mixers performance is the noise bandwidth (NBW). It was already discussed in chapter 2 that the NBW is defined as an IF frequency corresponding to the noise temperature rise by a factor of 2. The noise bandwidth (NBW) appeared to be

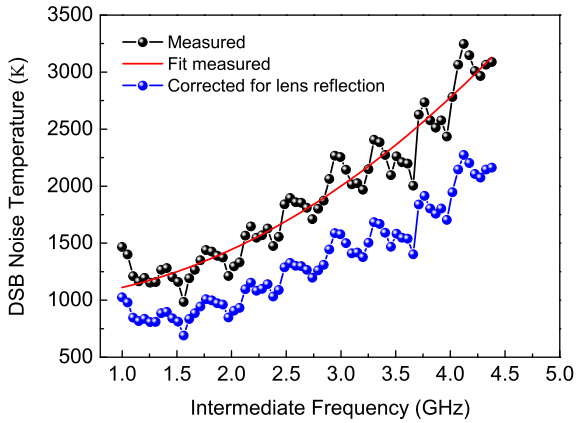

Fig. 4.17: Receiver DSB noise temperature versus IF frequency at 4.2 K (device 4). The 3 GHz receiver noise bandwidth extrapolated from the fit (solid red line).

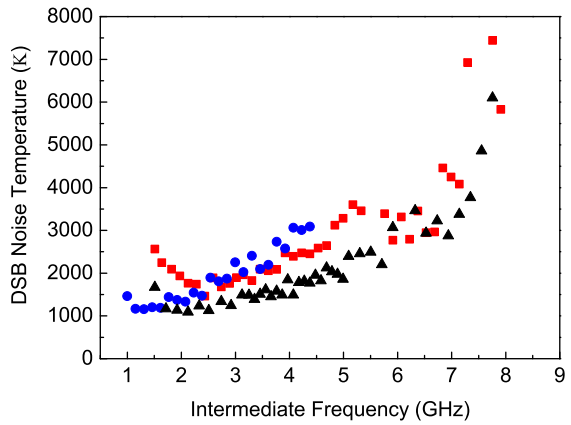

Fig. 4.18: DSB noise temperature versus intermediate frequency. Black triangles: NbN HEB mixer at 1.9 THz [18]. Blue circles: MgB_2 HEB mixer 4. Red squares: MgB_2 HEB mixer 5. Bath temperature 4.2K.

.

more than twice larger in mixer 5 than mixer 4. Indeed, the NBW extrapolated from the fit to the measured data was 6.5 GHz for mixer 5 and 3 GHz for mixer 4. The reason for this is that the critical temperature of mixer 5 is larger than mixer 4, hence the gain and the noise bandwidths are also larger. This suggests that the GBW and the NBW can be further increased by using thin films with a higher critical temperature.

The noise temperature of NbN HEB mixers was reported to be sensitive to the bath temperature [18, 112], increasing almost immediately as the bath temperature rises. Thus, it was interesting to verify how sensitive are MgB_2

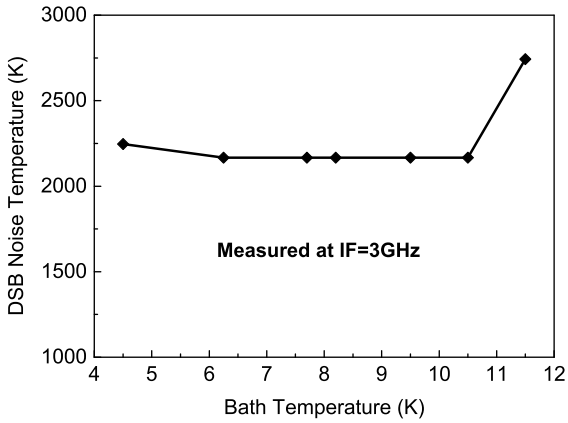

Fig. 4.19: DSB noise temperature versus bath temperature of MgB_2 mixer 5.

.

mixers to the bath temperature. The DSB noise temperature as a function of the bath temperature was measured for device 5 at IF frequency equal to 3 GHz. As it is shown in figure 4.19 the noise remains constant from 4.2 K up to 10.5 K, and rise at higher temperatures. This fact indicated that MgB_2 mixers can also work in a wider temperature range with no degradation of the performances compared to NbN mixers. Considering the high critical temperature that have been reported for thin films [81] and the results shown in figure 4.19, MgB_2 HEB mixers could open the possibility to increase the operation temperature up to 20 K or even higher enabling long term space programs.

In order to push the MgB_2 HEB mixers to higher LO frequencies, where the LO power is lower, devices were made smaller using e-beam lithography. Indeed, from the thermal balance equation 4.16, the local oscillator power is proportional to the bolometer volume and the critical temperature.

$$P = KV_{bol}(T_C^n - T_{bath}^n) \tag{4.16}$$

where K and n are material constants while V_{bol} is the bolometer volume. The receiver noise temperature, for smaller mixers, was recorded at 1.6 THz and 600 GHz, and the results of this study are presented in Paper [D]. The experiments at 600 GHz were done in order to confirm the reproducibility of the earlier results given in Paper [A] and Paper [C].

The 10 nm MgB_2 film used in this experiment was from the same batch of films which showed lower critical temperature (T_c between 8.5 K and 8.8 K). I-V curves recorded at 600 GHz with and without LO power applied are shown in figure 4.20(a). The critical current recorded at 4.2 K bath temperature was around 60 μA. Despite, the critical current increased from 60 μA to 85 μA upon cooling to 2.6 K, the noise temperature was very modest and just about 10% compared to 20% of device 4. Thus, the receiver noise temperature results are just shown for 4.2 K bath temperature. The DSB noise temperature as a function of the intermediate frequency and at LO frequency of 600 GHz and

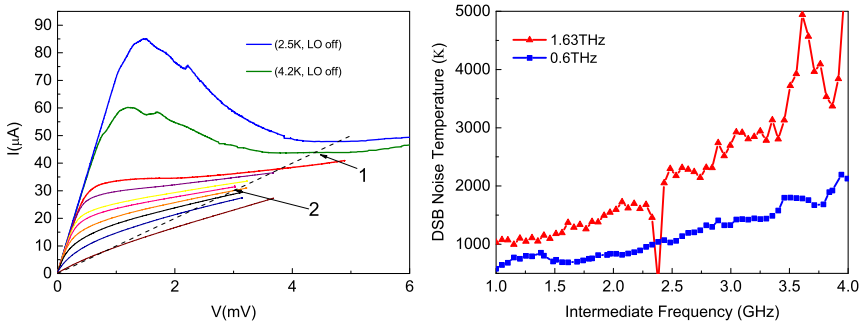

(a) (b)

Fig. 4.20: (a) I-V curves of HEB mixer fabricated in 10 nm MgB_2 with T_c of 8.8 K. LO frequency 600 GHz. The I-V at 2.5 K bath temperature is also shown while the rest of the curves were recorded at 4.2 K bath temperature. In the figure the constant resistance line is also shown. (b) DSB noise temperature at 1.6 THz and 600 GHz LO frequency and 4.2 K bath temperature.

1.6 THz is shown in figure 4.20(b). The minimum noise temperature was 700 K at 1.1 GHz IF frequency and 600 GHz LO frequency while the noise bandwidth was approximately 3 GHz. This results are very similar to what was discussed earlier in this work (see 4.17) and, hence to what was reported in the earlier publication (Paper [A]). These results indicate that low noise performances can be easily and repeatedly achieved in MgB_2 HEB mixers. The minimum DSB noise temperature recorded at 1.63 THz was almost 50% larger compared to the one recorded at 600 GHz. The reason for of this increase is unknown, yet. However, one of the possible explanation could be the contact resistance between the antenna and the bolometer,[7] which could cause extra losses at higher LO frequency.

Beside the IF bandwidth and the noise temperature study, the local oscillator power requirement estimation for this new THz mixers is also of high importance. Efficient coupling of the local oscillator power occur only at the condition $\hbar\omega > 2\triangle$. Indeed as it was discussed in 2.4, at this condition the energy gap of the MgB_2 superconductor is suppressed and thus upon application of the LO power the critical current in the HEBs is suppressed.

The absorbed LO power in the HEB mixer can be estimated using the an isothermal technique. The technique assumes that the bolometer response to the dc and to the RF power is the same [113]. By recording the unpumped and pumped I-V curves (pumped with LO) and by plotting a constant resistance line, the absorbed LO power is obtained considering the intersection points between the constant resistance line and the I-V curves as depicted in figure 4.20(a). Using this method the local oscillator power absorbed into the bolometer is then calculated using the following equation:

$$P_{LO} = V_2 I_2 - V_1 I_1 \tag{4.17}$$

[7] Which could be still existing despite the MgB_2 film was covered with $in-situ$ gold.

From figure 4.3 the absorbed power for device 4 was around 300 nW while for device 5 was around 60 μW. For the device (L=1 μm; W=1μm) in the figure 4.20(a) the absorbed power was around 200 nW. It is important to underline that the required LO power for device 5 was much higher due to the bigger bolometer area (volume ratio of 14 for the discussed devices) and higher T_c. These values of the absorbed LO power can be considered as a guideline since more detailed investigation is needed in order to estimate the LO power requirement for MgB_2 HEB mixers.

4.5 Conclusions

In conclusion, based on this research, MgB_2 HEB mixers could be the device of choice for future space mission.

The gain bandwidth was investigated with respect to the thickness and to the critical temperature of the film. Gain bandwidth of 1.3 GHz, 2.3 GHz and 3.4 GHz, corresponding to a mixer time constant of 130 ps, 70 ps and 47 ps was measured in 30 nm, 15 nm and 10 nm MgB_2 films, respectively. By fitting the gain bandwidth data with the 2-T model, the electron-phonon interaction time, the phonon escape time and the specific heat ratio were deduced for a given film thickness. It was found that the phonon escape time scaled almost proportionally to the film thickness while the electron-phonon interaction time and the specific heat ratio increased at high temperature.

For HEB mixers made from 10 nm film with a T_C of 8.5 K, the lowest noise temperature measured at 600 GHz was: 600 K and 800 K at bath temperature of 2 K and 4.6 K, respectively. For a mixer made from 10 nm film with a T_C of 15 K, a noise bandwidth as large as 6-7 GHz was obtained. At 1.6 THz, the lowest noise temperature was recorded to be 1150 K for a HEB made from 10 nm film with a T_C of 8.5 K.

The noise temperature was recorded as a function of the bath temperature for a mixer with a T_C of 15 K showing that the noise starts to rise only above 10.5 K. This indicates that MgB_2 HEB mixers can work in a wider temperature range when compared to NbN HEB mixers leading to, for example, longer space programs.

MgB_2 HEB mixers have demonstrated performances similar to the state of the art NbN HEB mixers. Improvement of the MgB_2 HEB mixers is still possible. Larger gain bandwidth can be achieved for devices fabricated in good quality thin films with a high T_C, moreover low noise performances can be easily achieved and in addition, MgB_2 film open the possibility to extend the operating temperature of the HEB mixer.

Chapter 5

Room-Temperature THz detection in $YBa_2Cu_3O_{7-x}$ bolometers

In this chapter, a concept of room-temperature THz bolometers made of $YBa_2Cu_3O_{7-x}$ film is analysed both theoretically and experimentally.

$YBa_2Cu_3O_{7-x}$ bolometers made of different film thicknesses, with a large variation of the area and the resistance were studied at room-temperature as incoherent and coherent detectors. The devices were tested across a wide THz frequency band, ranging between 0.1 THz up to 1.6 THz. These results have been published in Paper [E], [F] and [G].

In Paper [E], direct detection and mixing experiments were presented in bolometers fabricated with UV-lithography. Large improvement of the device performance was predicted for submicrometer dimensions. The predicted improvement was then confirmed in Paper [F] and in Paper [G]. In Paper [G], beside the responsivity results, a detailed study of the noise of nanometer scale $YBa_2Cu_3O_{7-x}$ bolometers is also presented.

5.1 THz direct detection

As it was discussed in chapter 1, the total power received from the detector is converted in electrical signal when the detector is used in the direct detection mode. Direct detectors preserve information of the amplitude but not the phase, and frequency selection is possible only when a filter is placed before the detector.

One of the most frequent questions is either to use a direct or a heterodyne detector. Direct detectors, compared to heterodyne, offer lower spectral resolution but at the same time they can operate in a wider spectral range and they do not require complicated configuration setup (e.g. for heterodyne detectors the LO source is a crucial component). Direct detector are usually preferable when a high spectral resolution is not a requirement.

Room-temperature direct detector offer lower sensitivity (higher NEP) when compared to cryogenic detectors, however they cost less and, thus they

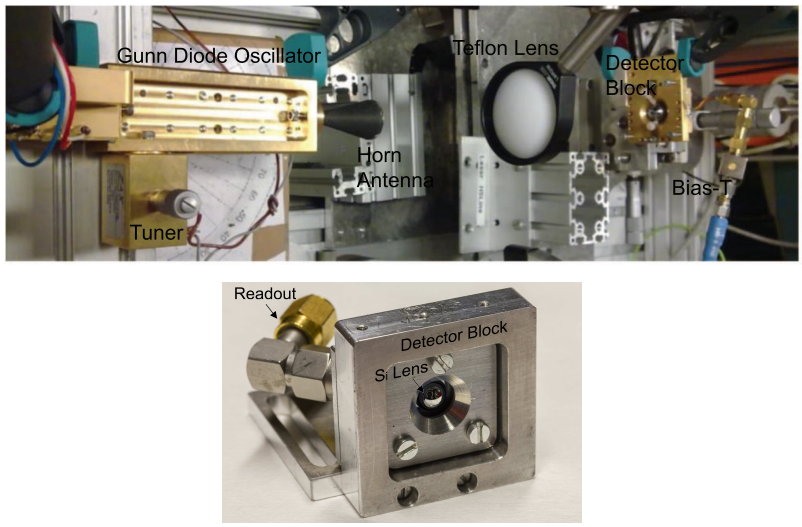

Fig. 5.1: Top figure: responsivity experiment setup at 100 GHz. In the picture, the Gunn diode oscillator with the horn antenna, the Teflon lens and the detector block with 12 mm Si lens are shown. Bottom figure: picture of the detector block with 5 mm Si lens used for the responsivity measurement at 400 GHz.

can be used when cryogenic cooling is not possible.

A comparison of some room-temperature THz direct detectors was already given in chapter 1. In this chapter, it is demonstrated that $YBa_2Cu_3O_{7-x}$ bolometers can be sensitive as well as fast at the room-temperature. The response time was measured to be much lower compared to other room-temperature bolometers (in the order of ns) allowing higher acquisition rate. $YBa_2Cu_3O_{7-x}$ bolometers integrated with a spiral antenna offer a possibility of a sensitive and fast detector with a simpler fabrication process and lower costs compared to other existing technologies. Moreover, the RF bandwidth of $YBa_2Cu_3O_{7-x}$ bolometers is just limited by the antenna, hence in principle a very wide RF bandwidth is possible for these new types of room-temperature detectors.

5.1.1 Experimental Technique

In order to investigate the $YBa_2Cu_3O_{7-x}$ bolometers three sets of measurements were performed: dc responsivity, RF responsivity and output noise.

DC measurements included current-versus-voltage (I-V) characterisation at room-temperature and the resistance versus temperature (R-T) characterisation. The discussed measurements were done in dip-stick which has the possibility to be cooled in a transport LHe or LN dewar[1].

For the RF responsivity measurements, the spiral antenna integrated YBCO bolometer (see chapter 3) were clamped on the backside of a Si lens forming the quasi-optical setup already discussed in chapter 4. As signal sources, amplitude modulated (AM) Gunn diode oscillator (at 0.1 THz), Backward Wave

[1]This setup was similar to the setup used during the dc characterization of MgB_2 HEB. But, for these experiments, the liquid nitrogen instead of the liquid helium dewar was used.

Oscillator (at 0.33 THz), multiplier based source (at 0.4 THz) and a far infrared (FIR) gas laser (at 0.7 THz and 1.6 THz) were used.

In Paper [E], the RF responsivity was measured at 0.33 THz. The source was equipped with horn antenna, and a Teflon lens was used to focus the beam into the detector. In order to calculate the RF responsivity the THz absorbed power, obtained from the isothermal technique [63], was employed in Paper [E] as well as in Paper [F]. In Paper [G], at 0.4 THz a source [37] equipped with 3.6 mm diagonal horn antenna with a directivity of 26 dB was used. The AM of the input signal up to 100 kHz was provided by using Agilent signal generator. The emitted power level from the source was measured with Erikson waveguide power meter with the same horn antenna as for the source. Both horns were placed at about 5 mm from each other giving an emitted power level of 170 μW. Just for comparison, another experiment was performed. The Erikson power meter and the source waveguides were flanged together, in this case the emitted power was measured to be 200 μW. The beam waist of the 3.6 mm horn antenna is very close to the beam waist of the detector, (mounted on 5 mm Si lens); by collocating the detector and the source at about 5 mm from each other a maximum coupling efficiency can be achieved[2]. For the RF responsivity calculations the emitted power value of 170 μW was employed referenced to the Si lens input. In order to obtain the intrinsic responsivity of the detectors optical losses have been analyzed and were used to obtain THz signal power at the detector terminals. For all RF resposivity calculations a loss coupling factor of 0.5, due to the spiral antenna polarization, as well as a transmission coefficient of 0.7 at lens-air interface were taken into consideration. The readout was done with dual phase lock-in amplifier in series with a voltage preamplifier. The DLPVA-100-BLN-S voltage amplifier had a switchable gain from 20 dB up to 100 dB an equivalent input noise voltage between 6 nV/Hz$^{0.5}$ and 700 pV/Hz$^{0.5}$ for lower and higher gain respectively. The amplifier had a switchable filter which was setting its the cut-off frequency. During the measurements the filter was fixed at 100 kHz (higher cut-off frequency) allowing to measure up to 100 kHz modulation frequency. While the gain was fixed to 80 dB lowering the noise level to approximately 730 pW/Hz$^{0.5}$. A dc block consisting of a series combination of a capacitor and a resistor was placed after the detector in order to avoid saturation of the preamplifier. The capacitor was blocking dc flowing into the amplifier while the resistor offered a real impedance load. The voltage response measured with the lock-in amplifier was multiplied by 2, which considers the peak-to-peak magnitude, and by $2^{0.5}$ originated from the lock-in rms amplitude. The obtained voltage response was then divided by the preamplifier gain.

The same lock-in amplifier and the same voltage preamplifier were used for noise measurements. The internal reference source of the lock-in was from 20 kHz up to 100 kHz.

During the whole measurements (responsivity and noise) bolometers were current biased. Current biasing was obtained using a voltage source with 10 kOhm resistor in series. The resistor in series has to be chosen much larger than the bolometer resistance. In these experiments the maximum bolometer resistance was around 900 Ohm. For the discussed setup, bolometer noise was much lower compared to when a current stabilized source was used to bias the

[2]The beam waist or beam focus is the point in which the radius of the beam is minimum.

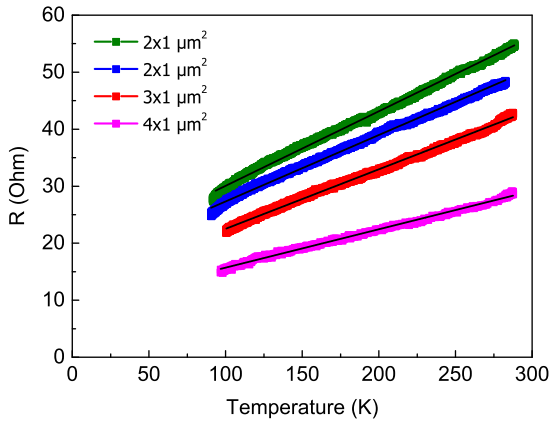

Fig. 5.2: Resistance versus temperatures curves (Paper [E]). The solid black line: linear fit used to extrapolate the temperature coefficient of resistance.

device. The reason for this could be explained by an extra noise generated by the current control feedback loop of the current source.

In figure 5.1 a picture of the experimental setup used for the responsivity measurements at 100 GHz is shown, together with the the detector blocks used during the experiments.

5.1.2 DC responsivity measurements

As it was already discussed through this thesis, $YBa_2Cu_3O_{7-x}$ is a high T_C superconductor. However, $YBa_2Cu_3O_{7-x}$ was considered as a material of choice to explore the concept of room-temperature THz bolometers for two reasons. It was noticed that at room-temperature $YBa_2Cu_3O_{7-x}$ had rather high temperature coefficient of resistance (in the range of $0.0012\,K^{-1}$ to $0.0025\,K^{-1}$) as well as a resistivity which was suitable for integration with a planar antenna. It was discussed in chapter 2 that high device responsivity is obtained using material with large temperature coefficient of resistance. Semiconductor materials offer even larger temperature coefficient of resistance compared to $YBa_2Cu_3O_{7-x}$, however those materials have very large resistivity hence they are not suitable for antenna coupled bolometers.

An easy way to estimate the bolometer RF responsivity is to measure the dc responsivity also called electrical or thermal responsivity. As it was already discussed in chapter 2, the responsivity (see eq. 2.15) is directly proportional to the bias current, I, and the temperature coefficient of resistance (TCR), α, while it is inversely proportional to the thermal conductance (G) to the substrate [114]. The TCR ($\alpha = \delta R/\delta T \cdot 1/R$) was experimental obtained by recording the R-T curves in the range between 100 K and 300 K. By linearly fitting the recorded data, and considering the device resistance at room-temperature, the TCR extrapolated for YBCO bolometers was in the range of $0.0012\,K^{-1}$ to $0.0025\,K^{-1}$(Paper [E]-[G]). In figure 5.2, an example of the resistance versus temperature curves for different device dimensions and

resistances is shown. From figure 5.2 it is possible to see that α multiplied by the device resistance hence, $\delta R/\delta T$ is temperature independent in the given range and increases with device resistance. This was not only the case for the bolometers presented in figure 5.2 but also valid for all devices studied in this work (see Paper [E] and Paper [G]). The general trend was that bolometer with high resistance showed larger dc responsivity, nevertheless if the resistance is too large then the RF mismatch between the antenna and the bolometer becomes larger leading to a reduction of the coupling efficiency.

Thermal conductance can be obtained from equation 5.1 using the recorded I-V and R-T curves of the devices (see figures 5.2 and 5.3). In order to understand if the thermal conductance was temperature dependent, the I-V curves were measured for a bolometer at several temperatures, ranging from room-temperature down to 112 K. The results reported in Paper [E] have showed that the thermal conductance is temperature independent. If the dominant heat removal from the bolometer occurs into the substrate, then the thermal conductance can be expressed by equation 2.17. Therefore, the thermal conductance is directly proportional to the bolometer area and inversely proportional to the thermal boundary resistance between the film and the substrate. For YBCO films on sapphire substrate, the thermal boundary resistance has been reported to be independent from the temperature [115]. Based on the temperature independence of thermal conductance and thermal boundary resistance, the heat removal from the YBCO bolometers occurs mainly into the substrate and heat diffusion into the contact pads is not visible.

$$G \equiv \frac{dP_{dc}}{dT} = \frac{dP_{dc}}{dR} \times \frac{dR}{dT} \tag{5.1}$$

The dissipated dc power (P_{dc}) in the current biased bolometer and the bolometer resistance can be extrapolated from the recorded I-V curves without RF power applied into the bolometer. Using this technique, the heat conductance was found to be in the range from 166 μW/K ($4 \cdot 1\mu m^2$) to 10 μW/K ($0.3 \cdot 0.5\mu m^2$) scaling down with the bolometer area, as predicted in Paper [E].

In figure 5.3 an example of the dc power versus resistance for two devices with dimensions 0.3 μm$\times$0.5 μm and room-temperature resistances of 915 Ohm and 383 Ohm is shown. By fitting the power versus resistance data, as in figure 5.3, the dP_{dc}/dR was obtained. The dR/dP_{dc} is equal to the bolometer responsivity at a bias current of 1 mA if it is expressed in Ohm/mW. For the bolometers in figure 5.3 both with dimensions $0.3 \cdot 0.5\mu m^2$ and room-temperature resistance of 382 Ohm and 915 Ohm, electrical responsivities as high as 65 V/W and 230 V/W were deduced at room-temperature and at 1 mA bias current. 230 V/W was the highest electrical responsivity deduced for $YBa_2Cu_3O_{7-x}$ supported bolometers substrate.

5.1.3 RF responsivity measurements

The RF or optical responsivity as a function of the bias current measured in a number of YBCO bolometers with different dimensions is shown in figure 5.4. As shown in figure 5.4 the RF responsivity increases with the increase of the bias current as well as with the decrease of the bolometer area. The maximum optical responsivity measured for larger ($4 \cdot 1\mu m^2$) and smaller bolometer area

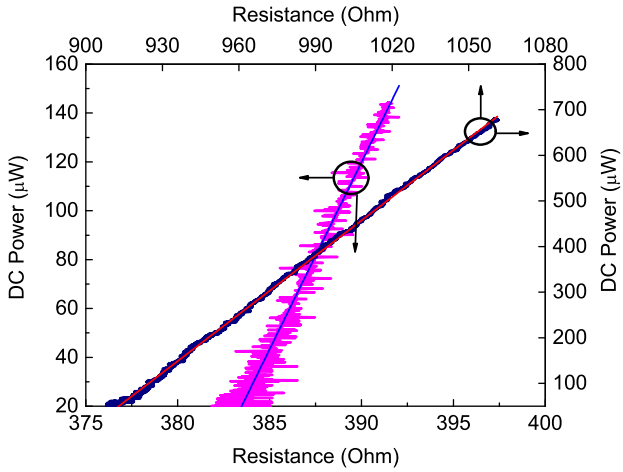

Fig. 5.3: Dissipated dc power as a function of the resistance for YBCO nanobolometers.

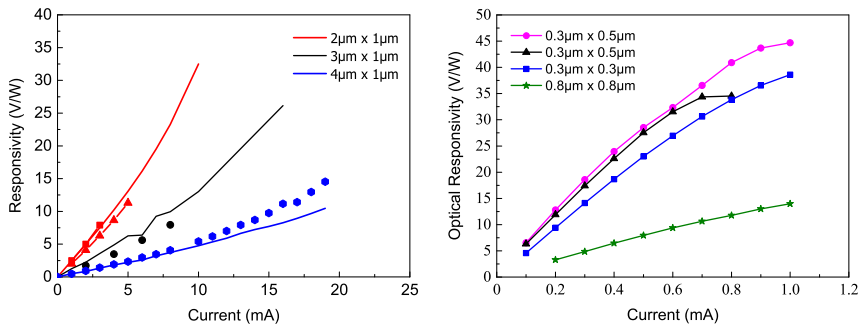

(a) (b)

Fig. 5.4: (a) Electrical (solid line) and optical responsivity measured at 0.33 THz (simbols) as a function of the bias current for YBCO bolometers made with UV-lithography (Paper [E]). (b) Optical responsivity measured at 0.4 THz and 1020 Hz modulation frequency as a function of the bias current for YBCO bolometers made with e-beam lithography. The electrical responsivity is shown in Table I of Paper [G].

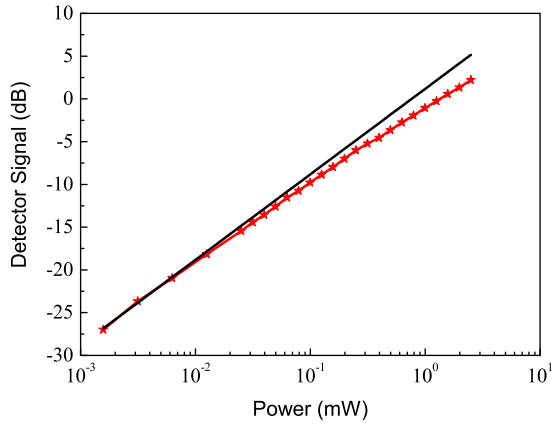

Fig. 5.5: Measured detector signal as a function of the absorbed RF power. Solid red line is a guide for the linearity behaviour.

$(0.3 \cdot 0.5\mu m^2)$ was 15 V/W and 45 V/W at 20 mA and 1 mA bias current, respectively. As expected an improvement of the optical responsivity was observed for bolometers with nanometer dimensions (see figure 5.4(b)).

For large devices (see figure 5.4(a)), the responsivity scales linearly with the bias current in a larger range of bias currents. Nevertheless, for nano-bolometers a sub-linear dependence with the bias current was observed above 0.6 mA (see figure 5.4(b)). In order to verify if the sub-linear behaviour of the responsivity with the bias current was caused by the temperature rise in the bolometer, the following experiment was conducted. Using an 100 GHz source, a high RF power (the RF power (0.7 mW) was higher than the highest dc power (0.4 mW) used for the same sample) was applied to the device. The result showed that the sub-linear regime starts at the same bias current, therefore it is not caused by an overheating of the device. Moreover, no nonlinear effect was observed for the power versus resistance curves up to the highest bias current (see figure 5.3).

A linearity investigation of the nano-bolometer $(0.3 \cdot 0.5\mu m^2)$ response was also performed. The bolometer response to the input signal power was experimentally verified up to 2.5 mW using 100 GHz source (see figure 5.5). The signal compression was 3 dB at the highest power level, and 1 dB compression point was observed for the absorbed power[3] of about 0.1-0.3 mW. The absorbed power was obtained from the bolometer voltage response and the responsivity.

It was also interesting to compare the electrical and the optical responsivity. For nano-bolometers the reduction of the optical responsivity when compared to electrical was between 20% and 70%. This reduction was mostly due to the antenna-bolometer impedance mismatch. By the calculating the mismatch loss (considering the antenna impedance to be 100 Ohm) the coupling efficiency

[3]The absorbed power was estimated from the device voltage response and the intrinsic responsivity.

Table 5.1: Optical responsivity at other frequencies. Bolometers dimensions are given in the table.

w · l(μm^2)	Optical responsivity (V/W) at 1mA	Frequency (THz)
0.3 · 0.5	4.8	1.6
0.5 · 0.5	1.8	1.6
0.5 · 0.5	4	0.7
0.5 · 0.5	9.6	0.115

was between 80% and 50% for lower and higher bolometer resistance. Better agreement was achieved when the optical responsivity was corrected for the coupling efficiency. In table 1 of the Paper [G] more details are reported, other discrepancies between the electrical and optical responsivity can be due to the uncertainty of the measurements.

The $YBa_2Cu_3O_{7-x}$ nano-bolometer optical responsivity was also measured at 1.6 THz, 0.7 THz and 0.1 THz, and the results are presented in table 5.1. For the responsivity calculation, it was assumed that all the power from the sources was coupled into the devices. Therefore, the responsivity values in the table 5.1 are in their lower limits. By comparing the responsivity at 0.7 THz with the responsivity at 0.4 THz, previously discussed, it appears that the responsivity measured at 0.7 THz is much lower than the responsivity measured at 0.4 THz at the same bias current. Thus, it is clear that not all the power from the laser was coupled into the device.

5.1.4 Noise measurements

As it was discussed in chapter 2, the noise equivalent power (NEP) (the ratio between noise voltage and responsivity) defines the sensitivity of a direct detector (see. equation 2.23). Therefore, beside the responsivity measurements, it is of high importance to characterize the detector in terms of noise[4].

The noise voltage of a large variety of YBCO bolometers was measured from 20 Hz up to 100 kHz readout frequency, and it was also verified that the voltage response was approximately flat for all devices in this frequency range (see figure 5.7(b)). In figure 5.6, the noise spectra of a 0.5 μm·0.3 μm YBCO bolometer, the 1/f noise guideline, the readout noise and the 50 Ohm load at zero bias are shown. The noise of a resistor, which had the same resistance as bolometer, was also measured in order to verify the accuracy of the experimental setup. The noise measured in the resistor test showed the theoretical predicted Johnson noise, thus the 1/f noise below 200 Hz was coming from the lock-in amplifier. It appears that bolometers at room-temperature are Johnson noise limited, while at cryogenic temperature superconducting bolometers are phonon noise limited [65]. Indeed, at cryogenic operation the device responsivity is much larger compared to the responsivity at room temperature, and hence the phonon noise becomes much larger (see equation 2.21). Moreover, at low temperature the Johnson noise is much smaller compared to the one at room-temperature (see equation 2.20).

[4]The noise contributions for a bolometer were already discussed in chapter 2, thus the reader may also refer to that chapter.

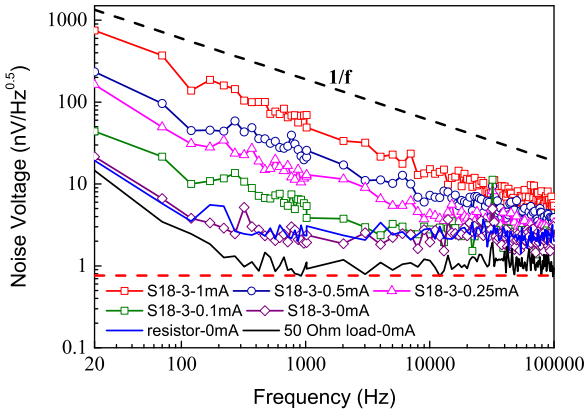

Fig. 5.6: Noise voltage as a function of the modulation frequency of 0.5 μm×0.3 μm bolometer with 270 Ohm room-temperature resistance at different bias current. In the figure, the 1/f guideline (black dashed line), the readout noise (red dashed line), the 50 Ohm load noise (black solid line) and the 270 Ohm resistor noise (blue solid line) are shown. Paper [G].

As shown in figure 5.6, the device noise voltage was measured at several bias currents. The device is 1/f noise limited across the whole frequency range up to 100 kHz when it is biased at 0.5 mA and at 1 mA. However, when the device is biased at lower bias current (0.1 mA and 0.25 mA), and for modulation frequencies larger than 4 kHz and 14 kHz the noise spectra tend to be frequency independent and the bolometer noise is determined by the thermal noise. Nevertheless, it is important to point out that in the region where the 1/f noise is dominant, the noise voltage increases proportionally to the bias current. At 1 mA bias current and at 100 kHz modulation frequency the system noise was 4-5 nV/Hz$^{0.5}$. From the I-V and R-T curves thermal conductance and the temperature coefficient of resistance were measured to be 10 $\mu W/K$ and 0.0025 K^{-1}, hence an electrical responsivity as high as 70 V/W was measured at 1 mA bias current. The system noise voltage together with the responsivity gave a system noise equivalent power of 70 pW/Hz$^{0.5}$. Therefore, the NEP for YBCO nano-bolometers (Paper [G]) is a factor of eight smaller compared to what was previously measured for larger bolometers in Paper [E]. Considering the readout noise of ∼0.73 nV/Hz$^{0.5}$, and by subtracting it from the system noise, the intrinsic bolometer noise equivalent power was calculated to be ∼50 pW/Hz$^{0.5}$.

In previous studies [116], it has been shown that the 1/f noise voltage in resistive films normalized to the dc voltage drop over the device and the film volume is more or less constant for a given material. Therefore, it was interesting to study a large variety of $YBa_2Cu_3O_{7-x}$ bolometers with different volumes. Nevertheless, in this work it was observed that the volume has no role. Figure 5.7(a) shows the noise voltage normalized by the voltage drop

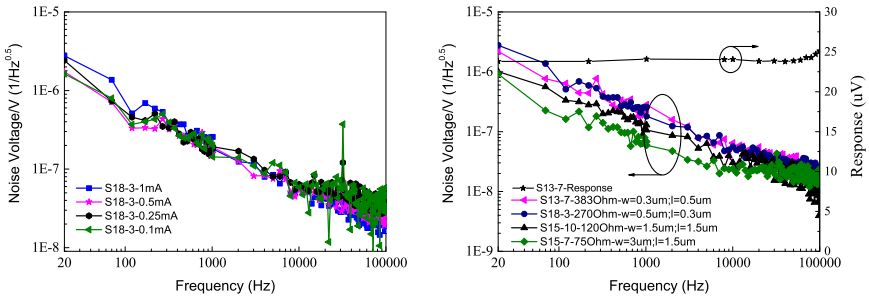

(a) (b)

Fig. 5.7: (a) Noise voltage normalized to the voltage drop over the bolometer as a function of the modulation frequency for a bolometer biased at different currents. Paper [G]. (b) Primary axis: Noise voltage normalized to the voltage drop over the bolometers as a function of the modulation frequency. Bolometers made of different YBCO films, having different resistances and dimensions. Secondary axis: Bolometer response as a function of the modulation frequency. All devices were biased at 1 mA. Paper [G].

over the bolometer as a function of modulation frequency for the same device and bias currents presented in figure 5.6. As it can be seen, curves overlap very well in whole frequency range, despite at low frequencies the absolute noise voltages differ for the currents from 0.1 mA and 1 mA. Furthermore, it was interesting to compare devices of different batches and volumes. In figure 5.7(b), the noise spectra normalized to the dc voltage of bolometers made of different films (deposited at different parameters but with the same thickness of 70 nm), with different areas and resistances, and biased at 1 mA is shown. The bolometer areas and resistances were ranging between 4.5 μm^2 to 0.15 μm^2 and between 383 Ohm and 75 Ohm. It was also noticed that in this case noise curves were almost the same for devices which differ in volume by about a factor of 30. It was also of great interest to compare the noise spectra of bolometers of two film thicknesses. 150 nm and 70 nm $YBa_2Cu_3O_{7-x}$ film thicknesses were used for this investigation. In figure 5.8, the measured noise data for bolometers with the same area (1.5 μm·1.5 μm), biased at the same current (3.3 mA), having different resistances (120 Ohm and 62 Ohm) and film thickness is presented. The ratio of the noise voltage normalized to the voltage drop over the bolometers is still the same despite the volume difference of two. As it follows from the data shown in figures 5.7 and 5.8, the value of the voltage-normalized noise voltage $(V_N/V)^2$) is constant over a large variation of bolometer volumes, geometries, thickness an resistances, and is equal to $6\times10^{-11}\times 1/f\times Hz^{-1}$. It is expected that this values can be applied for the noise estimation of any type of YBCO bolometers in the limit of 1/f noise.

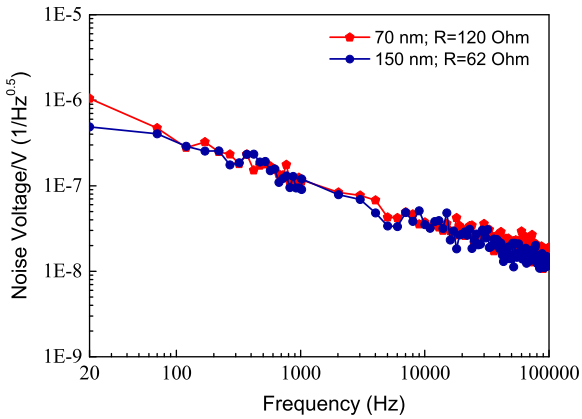

Fig. 5.8: Noise voltage normalized to the voltage drop over the bolometers for devices with different film thicknesses and same bolometer area (1.5 μm·1.5 μm). Paper [G].

5.1.5 Discussion and device optimisation

The smallest dimension for YBCO bolometer discussed in this research is 300 nm. Considering that the technological limit is not reached yet, bolometers with smaller area are still possible to fabricate in order to increase the responsivity. Furthermore, another possibility is to keep the same bolometer area but fabricating devices longer and narrower, in this way the resistance increases for a given current and, as a result the responsivity. However, the resistance cannot be too large, first of all because the mismatch loss antenna-bolometer increases and secondly because the Johnson noise will be larger for large device resistance, though a tradeoff must be found.

Equation 2.15 in the low current regime can be written as:

$$R_V = \frac{IR\alpha}{G} = \frac{\alpha V}{A} \times R_{bd} \tag{5.2}$$

Therefore, the noise equivalent power where the 1/f noise dominates can be written as:

$$NEP = \frac{V_N}{R_V} = \frac{V_N}{V}(\omega) \times \frac{A}{\alpha R_{bd}} \tag{5.3}$$

Since for $YBa_2Cu_3O_{7-x}$ bolometers the ratio of the noise voltage to the device voltage drop is approximately constant at each readout frequency, a higher device sensitivity (lower NEP) can be reached by minimizing the second term of the equation 5.3.

Concerning the device operation optimization, since both the responsivity and the noise voltage are dependent on the bias current, and the noise voltage is also a function of the modulation frequency, both responsivity and NEP (for the device of figure 5.6) are plotted as a function of the bias current with a modulation frequency as a parameter (see figure 5.9). The filled triangles

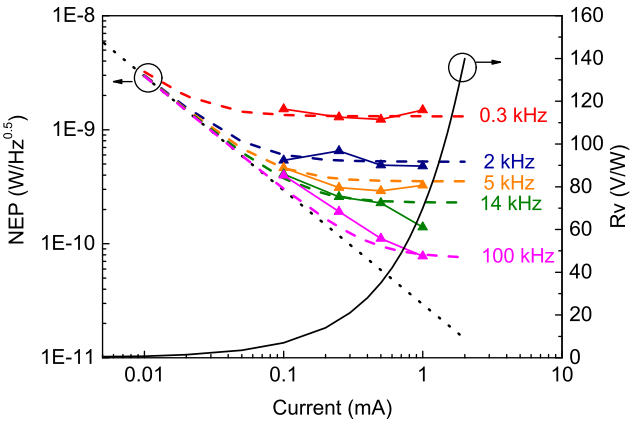

Fig. 5.9: Noise equivalent power and electrical responsivity as a function of the bias current. Responsivity as a function of the bias current (solid black line). Johnson and phonon noise (dotted black line). Experimental NEP (filled triangles). Fit to the measured data (dashed lines). Paper [G].

indicated the NEP which was obtained from the measured data. For a chosen modulation frequency the NEP was extrapolated from the noise voltage and the responsivity. The experimental data, at each modulation frequency, was fitted using the equation 5.4 showing a good agreement with the experimental data (filled triangles).

$$NEP^2 = \frac{4Rk_BT + V^2_{N-readout}}{R^2_V(I)} + 4k_BT^2G + \left(\frac{V_N}{V}(\omega) \cdot \frac{A}{\alpha R_{bd}}\right)^2 \qquad (5.4)$$

In equation 5.4, the R_V(I) is the electrical responsivity as a function of bias current which is indicated in figure 5.9 with the solid black line. The V_N/V was obtained from figure 5.7(a), while $V_{N-readout}$ is the noise of the readout circuit. The dashed black line in figure 5.9 represents the NEP limit imposed by the sum of Johnson and the phonon noise. As it is possible to notice from figure 5.9 at lower currents the NEP, for any modulation frequency, is always limited by Johnson noise, while on the contrary, as the current increases the NEP becomes 1/f noise limited. This limit is lower for higher modulation frequencies. Therefore, for the device optimization operation, if the system allows, lower NEP, and hence higher device sensitivity is reached at higher modulation frequencies.

For the bolometer optimization apart from the device area (A), already discussed before, larger TCR and thermal boundary resistance R_{bd} can allow further device optimization. Since, both the TCR and R_{bd} are material dependent, either further YBCO growth optimization or utilization of other materials will be required. Larger TCR for $YBa_2Cu_3O_{7-x}$ can be obtained by making the film thicker [117] while larger R_{bd} could be possible by modifying the interface between the film and the substrate or by choosing another

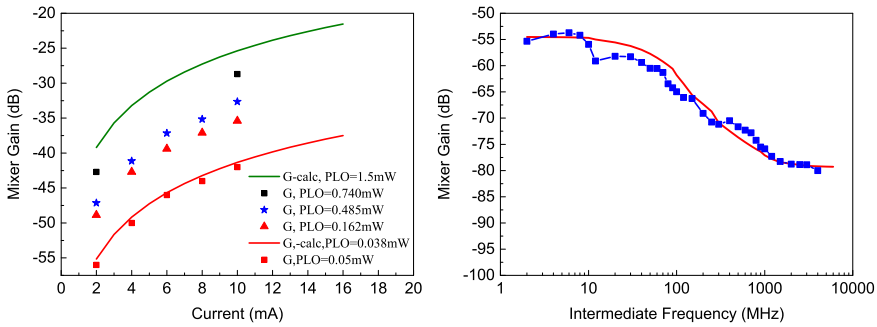

(a) (b)

Fig. 5.10: (a) Calculated (solid line) and measured (symbols) mixer gain as a function of the bias current at different LO power level for a $YBa_2Cu_3O_{7-x}$ bolometer at room-temperature ($3\,\mu m \times 1\,\mu m$). (b) Mixer signal as a function of the intermediate frequency (symbols). The solid line is a fitting curve corresponding to the response time of 2.5 ns. Paper [E].

substrate material [118]. However, large TCR and R_{bd} will make to bolometer slower but if one wants to optimize $YBa_2Cu_3O_{7-x}$ for frequency lower than 100 kHz which is much lower than than the roll-off frequency for these bolometers then the nanoseconds response time is not required.

5.2 THz heterodyne detection

Mixing experiments of $YBa_2Cu_3O_{7-x}$ bolometers at room-temperature are reported in Paper [E]. The mixer conversion gain was measured at 90 GHz using two sources one as a signal source and the other one as a local oscillator. The IF signal was amplified with low noise amplifier and measured with a spectrum analyzer.

The theory of the bolometric mixers has been already discussed in chapter 2. From equation 2.27, it is clear that both the local oscillator power and the bias current act towards a higher conversion gain. In figure 5.10(a), the calculated and the measured mixer conversion gain is shown as a function of the bias current. For all of the power levels, the total dissipated power which is the sum of the dc and and the RF power has not to exceed a maximum limit for the cautious operation of the mixers. Therefore, for the calculation of the maximum mixer gain, the maximum total dissipated power, and the maximum bias current together with the measured device parameters were used. The calculated conversion gain of a device with dimensions $3\,\mu m \times 1\,\mu m$ for LO power of 0.038 mW and 1.5 mW is shown in figure 5.10(a). The conversion gain was also measured at 100 GHz for different power levels and the results are presented in figure 5.10(a). The maximum measured mixer gain was -28 dB at 10 mA bias current and at the maximum LO power of 0.74 mW.

The bolometer response time was also discussed in chapter 2, and it is given by the ratio of the bolometer heat capacitance and the thermal con-

ductance into the substrate. It was interesting to calculate the response time considering the specific heat of $YBa_2Cu_3O_{7-x}$ films at room-temperature (400 J/kg× K [119]) and the measured thermal conductance. The response time was calculated to be 2.2 ns for the same bolometer as in figure 5.10(b).

The voltage response of an YBCO bolometer was measured at 90 GHz. The input signal from a signal generator was amplitude modulate from 10 Hz to 100 kHz. It was verified that the bolometer response was constant from 10 Hz to 100 kHz.

For higher modulation frequencies measurements, a mixing of two sources at 90 GHz was used. Using a 20 dB directional coupler the sources were coupled into the mixer. One of the two sources was used as LO at fixed frequency while the frequency of the other one was tuned to provide an IF band[5] from 8 MHz to 4 GHz. The signal was amplitude modulated for each frequency point and the voltage response was measured using a lock-in amplifier. The frequency tuning causes power variation, hence this signal from the lock-in was then used for the calibration of the power variation of the signal source.

The measured mixer gain as a function of the IF frequency is shown in figure 5.10(b). As it has been previously reported [120], the measured mixer gain has a second plateau at higher frequency (higher than 1 GHz). The lower frequency response, which is called bolometric response, is referred to the thermal conductance through the film/substrate while the second plateau at a higher frequency(in this case at frequency higher than 1 GHz) has been associated with the non-equilibrium response [120]. By fitting the measured data of figure 5.10(b) a time constant of 2.5 ns has been extrapolated for the bolometric response. The response time for $YBa_2Cu_3O_{7-x}$ bolometers was previously measured but only at low temperatures (77-90 K) [120]. In this research for the first time the response time was measured at room-temperature, showing the lowest response time reported among room-temperature bolometers.

5.3 Conclusions

In conclusion, YBCO bolometers are very promising candidates for room-temperature THz coherent and incoherent detection.

As a direct detector, a responsivity as high as 15 V/W was measured at 20 mA bias current for a $YBa_2Cu_3O_{7-x}$ bolometer area of $4\,\mu m^2$ while the minimum system noise equivalent power was 600 pW/Hz$^{0.5}$. The bolometer performance was improved when the area got scaled down. Maximum electrical and optical responsivities of 230 V/W and 45 V/W were measured for a bolometer with dimensions $0.3\,\mu$m·$0.5\,\mu$m and at a 1 mA bias current. For a bolometer with an electrical responsivity of 70 V/W the lowest system noise equivalent power was measured to be 70 pW/Hz$^{0.5}$. The noise of $YBa_2Cu_3O_{7-x}$ bolometers was investigated for a large number of devices with different areas, geometries, resistances, volumes and in different films. Results of this study showed that the 1/f noise normalized by the dc voltage drop into the bolometer is constant and equal to $(V_N/V)^2=6\times10^{-11}\times 1/f\times Hz^{-1}$. This value may be applied for the estimation of any $YBa_2Cu_3O_{7-x}$ device in the limit of 1/f noise.

[5] Two microwave amplifiers were used to cover the IF range from 8 MHz to 4 GHz.

In heterodyne detection mode the maximum mixer gain was measured to be -28 dB at 10 mA bias current and at 0.74 mW LO power. The mixer time constant was measured to be on the order of nanoseconds and the lowest reported for room-temperature bolometers.

Furthermore, improvements of YBCO bolometers are still possible since the technological limit has not been reached yet.

Chapter 6

Conclusions and future outlook

In this thesis, novel THz detectors made from magnesium diboride (MgB_2) and Yttrium barium copper oxide ($YBa_2Cu_3O_{7-x}$) films were fabricated, characterised and analysed.

Hot-electron bolometers are currently the device of choice for radio astronomical receivers for frequency above 1 THz. Using ultrathin 3-4 nm NbN films a gain bandwidth of 3-4 GHz can be routinely achieved. However, as radio astronomy advances towards higher frequencies and its tasks are getting broader and broader, mixers with even wider gain bandwidth are required, for example up to 10 GHz (as for SIS mixers).

In this hope MgB_2 hot-electron bolometer mixers were investigated with respect to the gain bandwidth and the noise temperature. The measured gain bandwidth data showed a clear inverse dependence on the film thickness and a direct dependence on the critical temperature. The widest gain bandwidth was measured to be 3.4 GHz in 10 nm MgB_2 films which is as wide as the one reported for the state of the art NbN HEB mixers (3-4 GHz) considering that MgB_2 films were more that three times thicker than NbN films (3-4 nm). Sunultanusly for such devices a noise temperature as low as 800 K and 1150 K was measure at 600 GHz and 1.6 THz. The noise temperature (T_r) was also measured to be constant up to 10.5 K on the contrary to NbN HEB mixers where T_r rises directly from 4.2 K.

Thinking about the future, using hybrid physical-chemical vapor deposition (HPCVD), MgB_2 films as thin as 7-8 nm with a critical temperature as high as 34 K have been already grown [81]. The combination of a small thickness and a high critical temperature is expected to reduce the device response time and enhance the presently achieved gain bandwidth up 13 GHz. MgB_2 hot-electron bolometer mixers might be the devices of choice for future Space missions. Due to the higher critical temperature compared to NbN, with MgB_2 films of $T_C \sim$30-40 K a possibility opens for HEB mixers to increase the operation temperature from 4 K to 20 K, where compact close-cycle cryocoolers are available, enabling long term space observation programs.

Room-temperature $YBa_2Cu_3O_{7-x}$ bolometers made on bulk substrate were studied in this work as coherent and incoherent detectors with the aim to

demonstrate a fast response rate and a high sensitivity. The minimum noise equivalent power (NEP) was measured to be 450 pW/Hz$^{0.5}$ for a device area of 4 μm^2. The thermal conductance is proportional to the bolometer area a careful analysis of the bolometer design was made in order to improve the device sensitivity. Upon minimization of the area, for a bolometer with dimensions of 0.3 μm·0.5 μm a NEP as low as 50 pW/Hz$^{0.5}$ was measured showing a much larger sensitivity. A detailed study of the noise in bolometers made of different films, having different areas, resistances and volumes, revealed that the 1/f noise can be quite precisely estimated based on the dc devices parameters. THz direct detection tests were performed in a wide frequency range from 100 GHz up to 1.6 THz showing the capability of $YBa_2Cu_3O_{7-x}$ bolometers to work well in a broad frequency range. In the heterodyne detection mode a response time as low as 2.5 ns was measured, showing the lowest response time reported among room temperature bolometers. In this thesis for the first time it was demonstrate that bolometer on bulk substrate can work at room temperature.

At frequency lower than 1 THz the most sensitive room temperature THz detectors are Schottky diodes and Si CMOS Field Effect Transistors. However at frequency higher than 1 THz their sensitivity quickly deteriorate.

$YBa_2Cu_3O_{7-x}$ THz detectors are promising candidates to cover frequencies from microwaves to at least 10 THz. Compared to other bolometers, $YBa_2Cu_3O_{7-x}$ microbolometers made on bulk substrate have shown smaller response time as well as easier, robust and low cost fabrication process. This indicates the possibility to develop far-infrared multi-pixel systems using a simpler fabrication process. However, in order to compete with more mature technologies such as CMOS a lot a studies need to be done. For example the exploration of other materials, beside $YBa_2Cu_3O_{7-x}$, can be an option for future device development.

In conclusion THz detectors based on MgB_2 and $YBa_2Cu_3O_{7-x}$ films can be promising candidate for sensing applications at cryogenic and room-temperature, further development and studies of these new technologies will be required.

Chapter 7

Summary of appended papers

This chapter presents a summary of the appended papers and a short description of my contribution for each paper.

Paper A

Low noise MgB_2 terahertz hot-electron bolometer mixers

In this paper the noise temperature was measured using standard Y-factor technique with hot and cold load. As noise temperature as low as 800 K was measured at 600 GHz for a device fabricated in 10 nm MgB_2 film with a critical temperature of 8.5 K. In this paper it was demonstrate that this new class of HEBs have similar noise temperature with state of the art NbN HEB and thus there is a large prospective that MgB_2 HEBs could be the device of choice for new space missions.

My contribution was: Mask design, process developing, device fabrication and characterisation. Writing of the paper. The MgB_2 material was grown by NTT Basic Research laboratories, Japan.

Paper B

Investigation of MgB_2 HEB mixer gain bandwidth

Preliminary gain bandwidth data for HEBs made on different MgB_2 film thickness are reported. Mixing experiment were manly done at 600 GHz showing a clear dependence of the GBW with the film thickness and competitive performance with the state of the art NbN HEBs.

My contribution was: Mask design, process developing, device fabrication and characterisation. Writing of the paper. The MgB_2 material was grown by NTT Basic Research laboratories, Japan.

Paper C

Study of IF bandwidth of MgB_2 phonon-cooled Hot electron bolometer mixers

In this paper a detailed analysis of the GBW measured data using the 2-T model was presented. From the model the electron-phonon interaction time, the escape time and the electron and phonon specific heat ratio were extrapolated as a function of the MgB_2 film thicknesses and critical temperatures. It was also demonstrated that for a device fabricated in 10 nm film with a critical temperature as large as 15 K the gain bandwidth was measured to be 3.4 GHz and the noise bandwidth (NBW) 6.5 GHz. The noise temperature was measured as a function of the bath temperature showing a constant noise up to 10 K. This indicate that MgB_2 HEBs can work in a wider temperature range compared to NbN HEBs.

My contribution was: Mask design, process developing, device fabrication and characterisation and modelling. Writing of the paper. The MgB_2 material was grown by NTT Basic Research laboratories, Japan.

Paper D

MgB_2 Hot-Electron Bolometer Mixers at Terahertz Frequencies

In this paper MgB_2 bolometer were fabricated using electron beam lithography. The fabricated devices did not show any degradation of the initial quality of the MgB_2 film used. Mixing experiments were performed in a variety of devices fabricated over a time period of two years. The minimum noise temperature was measured to be 700 K and 1150 K at 600 GHz and 1.6 THz LO frequencies. In this paper it was demonstrated that low noise performances can be achieved with large repeatability.

My contribution was: Mask Design, process developing, most of the device processing and measurements. The MgB_2 material was grown by NTT Basic Research laboratories, Japan.

Paper E

A Room Temperature Bolometer for Terahertz Coherent and Incoherent Detection

In this paper novel room-temperature bolometers made of $YBa_2Cu_3O_{7-x}$ were investigated as coherent and incoherent detectors. Devices made with UV-lithography showed a responsivity as large as 15 V/W and a noise equivalent power as low as, NEP=450pW/$Hz^{0.5}$. Mixing experiment showed a nanoseconds response time. In this paper discussions of further devices optimisation are also given.

My contribution was: Helping with the process development and some measurements.

Paper F

Fast Room Temperature THz Bolometers

In this paper $YBa_2Cu_3O_{7-x}$ bolometers were fabricated with e-beam lithography showing an overall improvement of the performance when going to nanometer sizes. Measurements were done at 100 GHz and 400 GHz. The maximum optical responsivity was measured to be 90 V/W at 100 GHz referred to the bolometer absorbed power. The Noise equivalent power was as low as 200 pW/Hz$^{0.5}$.

My contribution was: Mask design, material growth, process developing, device fabrication and characterisation. Writing of the paper.

Paper G

Low Noise Nanometer Scale Room-Temperature $YBa_2Cu_3O_{7-x}$ Bolometers for THz Direct Detection.

Room-temperature $YBa_2Cu_3O_{7-x}$ bolometers were investigated as direct detector in the frequency range between 100 GHz up to 1.6 THz. Several devices were fabricated in different films, having different volumes, resistances and geometries. The maximum electrical and optical responsivity was measured to be 230 V/W and 45 V/W at 1m A bias current, respectively. The lowest noise equivalent power was measured to be 50 pW/Hz$^{0.5}$. The noise voltage normalized by the voltage drop in the bolometer was found to be $(V_N/V)^2 = 6 \times 10^{-11} \times 1/f \times Hz^{-1}$ for a given modulation frequency and independently from the device volumes, geometries, resistance and films used. Thus it was concluded that for $YBa_2Cu_3O_{7-x}$ bolometer the 1/f noise can be estimated quite precisely based on the dc parameters. Future devices optimisation are also discussed.

My contribution was: Mask Design, material growth, process developing, device fabrication and characterisation. Writing of the paper.

Acknowledgment

During this time I have worked with a number of people with in some way or another have made important contribution to my work. First of all, I am indebted to my supervisor Assoc. Prof. Sergey Cherednichenko whom knowledge, guidance and advices have been very important to me. I would like to say thanks to him for pushing me in the right direction and for his support during the whole PhD study period. Thank to my examiner and co-supervisor Professor Jan Stake for his support and for giving me the possibility to start this path at the Terahertz and Millimetre Wave Laboratory. Many special thanks to Vladimir Drakinskiy for the fruitful discussions, for his advices and help in the process lab as well as for the nice chats during cafe break and for proofreading the thesis.

Hiroyuki Shibata and Professor Yasuhiro Tokura from NTT Basic Research Laboratories, are acknowledged for the material growth and for proofreading the papers.

Thanks to all my colleagues at Terahertz and Millimetre Wave Laboratory for the friendly atmosphere that has been created, and for the cakes that we have been eating together in five years. Special thanks to my colleague Evgenii Novoselov for the fruitful collaboration and for proofreading the thesis. Thanks to my office mate Aleksandra Malko for the nice squash games and for proofreading the thesis. Kiryl Kustanovich is acknowledged for the time dedicated in proofreading the thesis.

I want to thank all the staff of the Nanofabrication Laboratory, in particular: John Halonen, Henrik Fredriksen, Kaija Matikainen, Mahdad Sadeghi, Bengt Nilsson and Dr. Alexei Kalaboukhov.

Special thanks to my big family and friends for their love and support especially during these years far from home. Finally, I owe everything to my beloved fiancé Giuseppe for his encouraging and infinite support and patience. To you and my family I dedicate this thesis.

This work was financially supported by the European Research council (ERC), the Swedish Research Council (VR) and the Swedish National Space Board.

Bibliography

[1] P. Siegel, "Terahertz technology," *IEEE Transactions on Microwave Theory and Techniques*, vol. 50, no. 3, pp. 910–928, mar 2002.

[2] ——, "Terahertz technology in biology and medicine," *IEEE Transactions on Microwave Theory and Techniques*, vol. 52, no. 10, pp. 2438–2447, oct 2004.

[3] H.-B. Liu, H. Zhong, N. Karpowicz, Y. Chen, and X.-C. Zhang, "Terahertz spectroscopy and imaging for defense and security applications," *Proceedings of the IEEE*, vol. 95, no. 8, pp. 1514–1527, Aug 2007.

[4] J. Federici and L. Moeller, "Review of terahertz and subterahertz wireless communications," *Journal of Applied Physics*, vol. 107, no. 11, 2010.

[5] T. Phillips and J. Keene, "Submillimeter astronomy," *Proceedings of the IEEE*, vol. 80, no. 11, pp. 1662–1678, Nov 1992.

[6] A. Wootten and A. Thompson, "The Atacama Large Millimeter/Submillimeter Array," *Proceedings of the IEEE*, vol. 97, no. 8, pp. 1463 –1471, aug. 2009.

[7] J. Kumagal, "Space mountain submillimeter radio telescopes," *IEEE Spectrum*, vol. 42, no. 12, pp. 12 – 14, dec. 2005.

[8] D. Doyle, G. Pilbratt, and J. Tauber, "The Herschel and Planck Space Telescopes," *Proceedings of the IEEE*, vol. 97, no. 8, pp. 1403 –1411, aug. 2009.

[9] P. Richards, "Cosmic Microwave Background experiments-past, present and future," in *Infrared and Millimeter Waves, 2007 and the 2007 15th International Conference on Terahertz Electronics. IRMMW-THz. Joint 32nd International Conference on*, sept. 2007, pp. 12 –15.

[10] H.-W. Hübers, "Terahertz Heterodyne Receivers," *IEEE Journal of Selected Topics in Quantum Electronics*, vol. 14, no. 2, pp. 378–391, march-april 2008.

[11] J. Zmuidzinas and P. Richards, "Superconducting detectors and mixers for millimeter and submillimeter astrophysics," *Proceedings of the IEEE*, vol. 92, no. 10, pp. 1597 – 1616, oct. 2004.

[12] B. Ellison, B. Maddison, C. Mann, D. Matheson, M. Oldfield, S. Marazita, T. Crowe, P. Maaskant, and W. Kelly, "First Results for a 2.5 THz Schottky Diode Waveguide Mixer," in *Seventh International Symposium on Space Terahertz Technology*, Mar. 1996, p. 494.

[13] J. R. Tucker and M. J. Feldman, "Quantum detection at millimeter wavelengths," *Rev. Mod. Phys.*, vol. 57, pp. 1055–1113, Oct 1985.

[14] D. Winkler and T. Claeson, "High-frequency limits of superconducting tunnel junction mixers," *Journal of Applied Physics*, vol. 62, no. 11, pp. 4482–4498, 1987.

[15] G. de Lange, J. J. Kuipers, T. M. Klapwijk, R. A. Panhuyzen, H. van de Stadt, and M. W. M. de Graauw, "Superconducting resonator circuits at frequencies above the gap frequency," *Journal of Applied Physics*, vol. 77, no. 4, pp. 1795 –1804, feb 1995.

[16] B. Jackson and T. Klapwijk, "The current status of low-noise THz mixers based on SIS junctions," *Physica C: Superconductivity*, no. 0, pp. 368 – 373, 2002.

[17] W. Zhang, P. Khosropanah, J. R. Gao, E. L. Kollberg, K. S. Yngvesson, T. Bansal, R. Barends, and T. M. Klapwijk, "Quantum noise in a terahertz hot electron bolometer mixer," *Applied Physics Letters*, vol. 96, no. 11, pp. 111 113–111 113–3, mar 2010.

[18] S. Cherednichenko, V. Drakinskiy, T. Berg, P. Khosropanah, and E. Kollberg, "Hot-electron bolometer terahertz mixers for the Herschel Space Observatory," *Review of Scientific Instruments*, vol. 79, no. 3, pp. 034 501 –034 501–10, mar 2008.

[19] P. Lehikoinen, J. Mallat, P. Piironen, A. Lehto, J. Tuovinene, and A. V. Räisänen, "A 119 GHz planar Schottky diode mixer for a space application," *International Journal of Infrared and Millimeter Waves*, vol. 17, pp. 807–818, 1996.

[20] P. Siegel, R. Dengler, I. Mehdi, W. Bishop, and T. Crowe, "A 200 GHz planar diode subharmonically pumped waveguide mixer with state-of-the-art performance," in *Microwave Symposium Digest, 1992., IEEE MTT-S International*, jun 1992, pp. 595–598 vol.2.

[21] B. Thomas, A. Maestrini, and G. Beaudin, "A low-noise fixed-tuned 300-360 GHz sub-harmonic mixer using planar Schottky diodes," *Microwave and Wireless Components Letters, IEEE*, vol. 15, no. 12, pp. 865–867, dec 2005.

[22] K. Hui, J. Hesler, D. Kurtz, W. Bishop, and T. Crowe, "A micromachined 585 GHz Schottky mixer," *Microwave and Guided Wave Letters, IEEE*, vol. 10, no. 9, pp. 374 –376, sep 2000.

[23] W. Bishop, K. McKinney, R. Mattauch, T. Crowe, and G. Green, "A Novel Whiskerless Schottky Diode for Millimeter and Submillimeter Wave Application," in *Microwave Symposium Digest, 1987 IEEE MTT-S International*, vol. 2, 9 1975-june 11 1987, pp. 607–610.

[24] B. Thomas, P. G. Huggard, B. Alderman, B. P. Moyna, M. L. Oldfield, B. N. Ellison, and D. N. Matheson, "Integrated Heterodyne Receivers for MM SubMM Atmospheric Remote Sensing," in *MM-Wave Products and Technologies, 2006. The Institution of Engineering and Technology Seminar on*, nov. 2006, pp. 13 –18.

[25] P. Sobis, N. Wadefalk, A. Emrich, and J. Stake, "A Broadband, Low Noise, Integrated 340 GHz Schottky Diode Receiver," *IEEE Microwave and Wireless Components Letters*, vol. 22, no. 7, pp. 366–368, 2012.

[26] M. Dyakonov and M. Shur, "Shallow water analogy for a ballistic field effect transistor: New mechanism of plasma wave generation by dc current," *Physical Review Letter*, vol. 71, pp. 2465–2468, Oct 1993.

[27] S. Boppel, A. Lisauskas, D. Seliuta, L. Minkevičius, I. Kašalynas, G. Valušis, V. Krozer, and H. Roskos, "CMOS integrated antenna-coupled field-effect-transistors for the detection of 0.2 to 4.3 THz," in *IEEE 12th Topical Meeting on Silicon Monolithic Integrated Circuits in RF Systems*, Jan 2012, pp. 77–80.

[28] M. S. Vitiello, D. Coquillat, L. Viti, D. Ercolani, F. Teppe, A. Pitanti, F. Beltram, L. Sorba, W. Knap, and A. Tredicucci, "Room-temperature terahertz detectors based on semiconductor nanowire field-effect transistors," *Nano Letters*, vol. 12, no. 1, pp. 96–101, 2012, pMID: 22149118.

[29] A. Zak, M. A. Andersson, M. Bauer, J. Matukas, A. Lisauskas, H. G. Roskos, and J. Stake, "Antenna-Integrated 0.6 THz FET Direct Detectors Based on CVD Graphene," *Nano Letters*, vol. 14, no. 10, pp. 5834–5838, 2014.

[30] A. Lee, B. Williams, S. Kumar, Q. Hu, and J. Reno, "Real-time imaging using a 4.3 THz quantum cascade laser and a 320x240 microbolometer focal-plane array," *Photonics Technology Letters, IEEE*, vol. 18, no. 13, pp. 1415–1417, July 2006.

[31] A. J. Miller, A. Luukanen, and E. N. Grossman, "Micromachined antenna-coupled uncooled microbolometers for terahertz imaging arrays," *Proceeding SPIE*, vol. 5411, pp. 18–24, 2004.

[32] L. Liu, J. Hesler, H. Xu, A. Lichtenberger, and R. Weikle, "A broadband quasi-optical terahertz detector utilizing a zero bias schottky diode," *Microwave and Wireless Components Letters, IEEE*, vol. 20, no. 9, pp. 504–506, Sept 2010.

[33] P. H. Hairui Liu, Junsheng Yu and B. Alderman, "A multichannel thz detector using integrated bow-tie antennas," *International Journal of Antennas and Propagation*, 2013.

[34] A. Semenov, O. Cojocari, H.-W. Hubers, F. Song, A. Klushin, and A.-S. Muller, "Application of zero-bias quasi-optical schottky-diode detectors for monitoring short-pulse and weak terahertz radiation," *Electron Device Letters, IEEE*, vol. 31, no. 7, pp. 674–676, July 2010.

[35] J. Hesler, L. Liu, H. Xu, Y. Duan, and R. Weikle, "The development of quasi-optical THz detectors," in *33rd International Conference on Infrared, Millimeter and Terahertz Waves, 2008.*, Sept 2008, pp. 1–2.

[36] J. Hesler and T. Crowe, "Responsivity and noise measurements of zero-bias schottky diode detectors," in *Eighteenth International Symposium on Space Terahertz Technology*, A. Karpov, Ed., 2007, p. 89.

[37] http://vadiodes.com/index.php/en/.

[38] A. Lisauskas, S. Boppel, D. Seliuta, L. Minkevicius, I. Kasalynas, G. Valusis, V. Krozer, and H. G. Roskos, "Terahertz detection and coherent imaging from 0.2 to 4.3 THz with silicon CMOS field-effect transistors," in *Microwave Symposium Digest (MTT), 2012 IEEE MTT-S International*, june 2012, pp. 1–3.

[39] L. Vicarelli, M. S. Vitiello, D. Coquillat, A. Lombardo, A. C. Ferrari, W. Knap, M. Polini, V. Pellegrini, and A. Tredicucci, "Graphene field-effect transistors as room-temperature terahertz detectors," in *Nature Publishing Group*, vol. 11, no. 10, 2012, pp. 865–871.

[40] A. Pitanti, D. Coquillat, D. Ercolani, L. Sorba, F. Teppe, W. Knap, G. De Simoni, F. Beltram, A. Tredicucci, and M. S. Vitiello, "Terahetz detection by heterostructed inas/insb nanowire based field effect transistors," *Applied Physics Letters*, vol. 101, no. 14, 2012.

[41] A. Luukanen, A. J. Miller, and E. N. Grossman, "Active millimeter-wave video rate imaging with a staring 120-element microbolometer array," *Proc. SPIE*, vol. 5410, pp. 195–201, 2004.

[42] T. Hwang, Lai, S. E. Schwarz, and D. B. Rutledge, "Microbolometers for infrared detection," *Applied Physics Letters*, vol. 34, no. 11, pp. 773 –776, jun 1979.

[43] M. Bolduc, M. Terroux, B. Tremblay, L. Marchese, E. Savard, M. Doucet, H. Oulachgar, C. Alain, H. Jerominek, and A. Bergeron, "Noise-equivalent power characterization of an uncooled microbolometer-based thz imaging camera," pp. 80 230C–80 230C–10, 2011.

[44] N. Oda, "Uncooled bolometer-type terahertz focal plane array and camera for real-time imaging," *Comptes Rendus Physique*, vol. 11, no. 7,8, pp. 496–509, 2010.

[45] M. Kroug, S. Cherednichenko, H. Merkel, E. Kollberg, B. Voronov, G. Gol'tsman, H. Huebers, and H. Richter, "NbN hot electron bolometric mixers for terahertz receivers," *IEEE Transactions on Applied Superconductivity*, vol. 11, no. 1, pp. 962–965, mar 2001.

[46] J. W. Kooi, J. J. A. Baselmans, M. Hajenius, J. R. Gao, T. M. Klapwijk, P. Dieleman, A. Baryshev, and G. de Lange, "IF impedance and mixer gain of NbN hot electron bolometers," *Journal of Applied Physics*, vol. 101, no. 4, pp. 044 511–044 511–8, feb 2007.

[47] A. Skalare, W. R. McGrath, B. Bumble, H. G. LeDuc, P. J. Burke, A. A. Verheijen, R. J. Schoelkopf, and D. E. Prober, "Large bandwidth and low noise in a diffusion-cooled hot-electron bolometer mixer," *Applied Physics Letters*, vol. 68, no. 11, pp. 1558–1560, mar 1996.

[48] I. Tretyakov, S. Ryabchun, M. Finkel, A. Maslennikova, K. N., A. Lobastova, B. Voronov, and G. Gol'tsman, "Low noise and wide bandwidth of NbN hot-electron bolometer mixers," *Applied Physics Letters*, vol. 98, no. 3, pp. 033 507–3, 2011.

[49] D. E. Prober, "Superconducting terahertz mixer using a transition-edge microbolometer," *Applied Physics Letters*, vol. 62, no. 17, pp. 2119 – 2121, apr 1993.

[50] Y. Xu, M. Khafizov, L. Satrapinsky, P. Kúš, A. Plecenik, and R. Sobolewski, "Time-Resolved Photoexcitation of the Superconducting Two-Gap State in MgB_2 Thin Films," *Phys. Rev. Lett.*, vol. 91, p. 197004, Nov 2003.

[51] K. S. Ilin, M. Lindgren, M. Currie, A. D. Semenov, G. N. Goltsman, R. Sobolewski, S. I. Cherednichenko, and E. M. Gershenzon, "Picosecond hot-electron energy relaxation in NbN superconducting photodetectors," *Applied Physics Letters*, vol. 76, no. 19, pp. 2752 –2754, may 2000.

[52] K. Fossheim and A. Sudbø, *Superconductivity Physics and Applications*. John Wiley & Sons, 2004.

[53] M. Lindgren, M. Currie, C. Williams, T. Y. Hsiang, P. M. Fauchet, R. Sobolewski, S. H. Moffat, R. A. Hughes, J. S. Preston, and F. A. Hegmann, "Intrinsic picosecond response times of YBaCuO superconducting photodetectors," *Applied Physics Letters*, vol. 74, no. 6, pp. 853–855, 1999.

[54] A. Hammar, S. Cherednichenko, S. Bevilacqua, V. Drakinskiy, and J. Stake, "Terahertz Direct Detection in $YBa_2Cu_3O_{7-x}$ Microbolometers," *IEEE Transactions on Terahertz Science and Technology*, vol. 1, no. 2, pp. 390–394, Nov 2011.

[55] P. L. Richards, "Bolometers for infrared and millimeter waves," *Journal of Applied Physics*, vol. 76, no. 1, pp. 1–24, jul 1994.

[56] S. Langley, "The bolometer," *Nature Publishing Group*, vol. 25, pp. 14–15, 1881.

[57] A. Rogalski and F. Sizov, "Terahertz detectors and focal plane arrays," *Opto-Electronics Review*, vol. 19, pp. 346–404, Sep. 2011.

[58] E. T. Swartz and R. O. Pohl, "Thermal resistance at interfaces," *Applied Physics Letters*, vol. 51, no. 26, pp. 2200–2202, Dec 1987.

[59] N. Chi-Anh, H.-J. Shin, K. Kim, Y.-H. Han, and S. Moon, "Characterization of uncooled bolometer with vanadium tungsten oxide infrared active layer," *Sensors and Actuators A: Physical*, pp. 87–91, 2005.

[60] J. B. Johnson, "Thermal Agitation of Electricity in Conductors," *Phys. Rev.*, vol. 32, pp. 97–109, Jul 1928.

[61] V. Vassilev, D. Henke, I. Lapkin, O. Nystrom, R. Monje, A. Pavolotsky, and V. Belitsky, "Design and Characterization of a 211-275 GHz Sideband Separating Mixer for the APEX Telescope," *IEEE Microwave and Wireless Components Letters*, vol. 18, no. 1, pp. 58–60, Jan 2008.

[62] F. Arams, C. Allen, B. Peyton, and E. Sard, "Millimeter mixing and detection in bulk InSb," *Proceedings of the IEEE*, vol. 54, no. 4, pp. 612–622, april 1966.

[63] H. Ekström, B. Karasik, E. Kollberg, and K. Yngvesson, "Conversion gain and noise of niobium superconducting hot-electron-mixers," *IEEE Transactions on Microwave Theory and Techniques*, vol. 43, no. 4, pp. 938–947, apr 1995.

[64] E. Gershenzon, G. Gol´tsman, I. Gogidze, Y. Gusev, A. Elantev, B. Karasik, and A. Semenov, "Millimeter and submillimeter range mixer based on electronic heating of superconductive films in the resistive state," *Superconductivity*, vol. 10, no. 3, pp. 1582–1597, 1990.

[65] J. Mather, "Bolometer noise: nonequilibrium theory," *Applied Optics*, vol. 21, pp. 1125–1129, 1982.

[66] K. Yngvesson and E. Kollberg, "Optimum Receiver Noise Temperature for NbN HEB Mixers According to the Standard Model," in *Tenth International Symposium on Space Terahertz Technology*, T. Crowe and R. Weikle, Eds., Mar. 1999, p. 563.

[67] H. Ekstrom, E. Kollberg, P. Yagoubov, G. Goltsman, E. Gershenzon, and S. Yngvesson, "Gain and noise bandwidth of NbN hot-electron bolometric mixers," *Applied Physics Letters*, vol. 70, no. 24, pp. 3296 –3298, jun 1997.

[68] D. M. Pozar, *Microwave Engineering (4nd ed)*. John Wiley&Sons, Inc.

[69] T. G. Phillips and K. B. Jefferts, "A Low Temperature Bolometer Heterodyne Receiver for Millimeter Wave Astronomy," *Review of Scientific Instruments*, vol. 44, no. 8, pp. 1009–1014, aug 1973.

[70] A. D. Semenov, H. Richter, H.-W. Hubers, B. Gunther, A. Smirnov, K. S. Il'in, M. Siegel, and J. P. Karamarkovic, "Terahertz Performance of Integrated Lens Antennas With a Hot-Electron Bolometer," *IEEE Transactions on Microwave Theory and Techniques*, vol. 55, no. 2, pp. 239 –247, feb. 2007.

[71] A. Sergeev and V. Mitin, "Electron-phonon interaction in disordered conductors: Static and vibrating scattering potentials," *Phys. Rev. B*, vol. 61, pp. 6041–6047, Mar 2000.

[72] B. Karasik, A. Sergeev, and D. Prober, "Nanobolometers for THz Photon Detection," *IEEE Transactions on Terahertz Science and Technology*, vol. 1, no. 1, pp. 97–111, sept. 2011.

[73] B. S. Karasik and A. I. Elantiev, "Noise temperature limit of a superconducting hot electron bolometer mixer," *Applied Physics Letters*, vol. 68, no. 6, pp. 853–855, feb 1996.

[74] N. Perrin and C. Vanneste, "Response of superconducting films to a periodic optical irradiation," *Phys. Rev. B*, vol. 28, pp. 5150–5159, Nov 1983.

[75] J. R. Waldram, *Superconductivity of Metals and Cuprates*. Institute of Physics Publishing, 1996.

[76] J. Nagamatsu, N. Nakagawa, T. Muranaka, Y. Zenitani, and J. Akimitsu, "Superconductivity at 39 K in magnesium diboride," *Nature*, vol. 410, no. 6824, pp. 63–64, feb 2001.

[77] J. R. Gavaler, M. A. Janocko, and C. K. Jones, "Preparation and properties of high-Tc Nb_3Ge films," *Journal of Applied Physics*, vol. 45, no. 7, pp. 3009 –3013, jul 1974.

[78] B. Cristina and Y. Tsutomu, "Review of the superconducting properties of MgB_2," *Superconductor Science and Technology*, vol. 14, no. 11, nov 2001.

[79] XXXi, "MgB_2 thin films," *Superconductor Science and Technology*, vol. 22, no. 4, apr 2009.

[80] S. Cherednichenko, P. Khosropanah, E. Kollberg, M. Kroug, and H. Merkel, "Terahertz superconducting hot-electron bolometer mixers," *Physica C: Superconductivity*, vol. 372-376, Part 1, no. 0, pp. 407–415, 2002.

[81] Z. Yuhao, L. Zhiyuan, D. Qian, L. Dongyao, W. Yinbo, Z. Yan, W. Yue, and F. Qingrong, "Ultrathin MgB_2 films fabricated on Al_2O_3 substrate by hybrid physical chemical vapor deposition with high Tc and Jc," *Superconductor Science and Technology*, vol. 24, no. 1, jan 2011.

[82] F.-Y. Li, R.-J. Wang, S.-C. Li, L.-C. Chen, J.-L. Zhu, Z.-X. Liu, R.-C. Yu, and C.-Q. Jin, "Ultrasound studies of MgB_2 superconductor under hydrostatic pressure," *Phys. Rev. B*, vol. 65, p. 132517, Mar 2002.

[83] S. Kaplan, "Acoustic matching of superconducting films to substrates," *Journal of Low Temperature Physics*, vol. 37, no. 3-4, pp. 343–365, 1979.

[84] R. J. Stoner and H. J. Maris, "Kapitza conductance and heat flow between solids at temperatures from 50 to 300 K," *Phys. Rev. B*, vol. 48, pp. 16 373–16 387, Dec 1993.

[85] A. D. Semenov, R. S. Nebosis, Y. P. Gousev, M. A. Heusinger, and K. F. Renk, "Analysis of the nonequilibrium photoresponse of superconducting films to pulsed radiation by use of a two-temperature model," *Phys. Rev. B*, vol. 52, pp. 581–590, Jul 1995.

[86] [Online]. Available: http://www.cm.ph.bham.ac.uk/research/thinfilms/thinfilms.html

[87] Y. Cui, J. Jones, A. Beckley, R. Donovan, D. Lishego, E. Maertz, A. Pogrebnyakov, P. Orgiani, J. Redwing, and X. Xi, "Degradation of MgB_2 thin films in water," *IEEE Transactions on Applied Superconductivity*, vol. 15, no. 2, pp. 224 – 227, june 2005.

[88] R. K. Singh, Y. Shen, R. Gandikota, J. M. Rowell, and N. Newman, "Effect of stoichiometry on oxygen incorporation in MgB_2 thin films," 2007.

[89] H. Shibata, T. Akazaki, and Y. Tokura, "Ultrathin MgB_2 films fabricated by molecular beam epitaxy and rapid annealing," *Superconductor Science and Technology*, vol. 26, no. 3, p. 035005, 2013.

[90] K. Ueda and M. Naito, "In situ growth of superconducting MgB_2 thin films by molecular-beam epitaxy," *Journal of Applied Physics*, vol. 93, no. 4, pp. 2113–2120, feb 2003.

[91] J. M. Phillips, "Substrate selection for high-temperature superconducting thin films," *Journal of Applied Physics*, vol. 79, no. 4, pp. 1829–1848, 1996.

[92] [Online]. Available: http://www.tydexoptics.com/products/thz_optics/thz_materials/

[93] N. Masilamani, O. Shcherbakova, S. Fedoseev, A. Pan, and S. Dou, "Effect of Substrate and Buffer Layer Materials on Properties of Thin $YBa_2Cu_3O_{7-x}$ Films," *Applied Superconductivity, IEEE Transactions on*, vol. 23, no. 3, pp. 6 601 105–6 601 105, June 2013.

[94] I. Mazin, O. Andersen, O. Jepsen, O. Dolgov, J. Kortus, A. Golubov, A. Kuz'menko, and D. M. van der, "Superconductivity in MgB_2: Clean or Dirty?" *Physical Review Letters*, vol. 89, no. 10, pp. 107 002/1–107 002/4, 2002.

[95] E. Grossman, "Lithographic antennas for submillimeter and infrared frequencies," in *Electromagnetic Compatibility, 1995. Symposium Record., 1995 IEEE International Symposium on*, Aug 1995, pp. 102–107.

[96] S. Cherednichenko, V. Drakinskiy, J. Baubert, B. Lecomte, F. Dauplay, J.-M. Krieg, Y. Delorme, A. Feret, H.-W. Hübers, A. D. Semenov, and G. N. Gol'tsman, "2.5 THz multipixel heterodyne receiver based on NbN HEB mixers," 2006.

[97] H.-W. Hübers, J. Schubert, A. Krabbe, M. Birk, G. Wagner, A. Semenov, G. Gol'tsman, B. Voronov, and E. Gershenzon, "Parylene antireflection coating of a quasi-optical hot-electron-bolometric mixer at terahertz frequencies," *Infrared Physics & Technology*, vol. 42, no. 1, pp. 41 – 47, 2001.

[98] A. Dobroiu, M. Yamashita, Y. N. Ohshima, Y. Morita, C. Otani, and K. Kawase, "Terahertz imaging system based on a backward-wave oscillator," *Applied Optics*, vol. 43, no. 30, pp. 5637–5646, Oct 2004.

[99] G. A. Blake, K. B. Laughlin, R. C. Cohen, K. L. Busarow, D.-H. Gwo, C. A. Schmuttenmaer, D. W. Steyert, and R. J. Saykally, "Tunable far infrared laser spectrometers," *Review of Scientific Instruments*, vol. 62, no. 7, pp. 1693–1700, 1991.

[100] G. Chattopadhyay, "Technology, capabilities, and performance of low power terahertz sources," *IEEE Transactions on Terahertz Science and Technology*, vol. 1, no. 1, pp. 33–53, Sept 2011.

[101] A. Maestrini, I. Mehdi, J. Siles, J. Ward, R. Lin, B. Thomas, C. Lee, J. Gill, G. Chattopadhyay, E. Schlecht, J. Pearson, and P. Siegel, "Design and Characterization of a Room Temperature All-Solid-State Electronic Source Tunable From 2.48 to 2.75 THz," *IEEE Transactions on Terahertz Science and Technology*, vol. 2, no. 2, pp. 177–185, March 2012.

[102] [Online]. Available: http://www.eccosorb.com/

[103] S. Cherednichenko, P. Yagoubov, K. Il'in, G. Gol'tsman, and E. Gershenzon, "Large Bandwidth of NbN Phonon-Cooled Hot-Electron Bolometer Mixers," in *27th European Microwave Conference, 1997.*, vol. 2, sept. 1997, pp. 972–977.

[104] Y. R.S.Nebosis, A.D. Semenov and K. Renk, "Rigorous analysis of a superconducting hot-electron bolometer mixer: Theory and comparison with experiment," in *Seventh International Symposium on Space Terahertz Technology*, mar 1996, p. 601.

[105] J. S. Blakemore, *Solid State Physics (2nd ed).* Cambridge, UK: University press, 1985.

[106] C. Wälti, E. Felder, C. Degen, G. Wigger, R. Monnier, B. Delley, and H. R. Ott, "Strong electron-phonon coupling in superconducting MgB_2:A specific heat study," *Phys. Rev. B*, vol. 64, p. 172515, Oct 2001.

[107] L. Jian-Lin, Z. Jie, C. Zhao-Jia, B. Hai-Yang, W. Yu-Peng, M. Ji-Bao, J. Duo, R. Zhi-An, C. Guang-Can, and Z. Zhong-Xian, "Low Temperature Specific Heat of Superconducting MgB_2," *Chinese Physics Letters*, vol. 18, no. 6, p. 820, 2001.

[108] S. Cherednichenko, V. Drakinskiy, K. Ueda, and M. Naito, "Terahertz mixing in MgB_2 microbolometers," *Applied Physics Letters*, vol. 90, no. 2, pp. 023 507–023 507–3, Jan 2007.

[109] D. Cunnane, J. Kawamura, B. S. Karasik, M. A. Wolak, and X. X. Xi, "Development of hot-electron THz bolometric mixers using MgB_2 thin films," *Proceeding SPIE*, vol. 9153, pp. 91 531Q–91 531Q–10, 2014.

[110] H. B. Callen and T. A. Welton, "Irreversibility and generalized noise," *Physical Review*, vol. 83, pp. 34–40, Jul 1951.

[111] W. Zhang, N. Li, L. Jiang, Y. Ren, Q.-J. Yao, Z.-H. Lin, S.-C. Shi, B. M. Voronov, and G. N. Gol'tsman, "Dependence of noise temperature of quasi-optical superconducting hot-electron bolometer mixers on bath temperature and optical-axis displacement," *Proceeding SPIE*, vol. 6840.

[112] S. Cherednichenko, M. Kroug, H. Merkel, E. Kollberg, D. Loudkov, K. Smirnov, B. Voronov, G. Gol'Tsman, and E. Gershenzon, "Local Oscillator Power Requirement and Saturation Effects in NbN HEB Mixers," in *Twelfth International Symposium on Space Terahertz Technology*, I. Mehdi, Ed., Dec. 2001, p. 273.

[113] H. Ekstrom, B. Karasik, R. Weikle, K. Yngvesson, G. Gol'tsman, E. Kollberg, and E. Gershenzon, "Mixers using superconducting nb films in the resistive state," in *23rd European Microwave Conference*, Sept 1993, pp. 787–789.

[114] P. L. Richards, J. Clarke, R. Leoni, P. Lerch, S. Verghese, M. R. Beasley, T. H. Geballe, R. H. Hammond, P. Rosenthal, and S. R. Spielman, "Feasibility of the high Tc superconducting bolometer," *Applied Physics Letters*, vol. 54, no. 3, pp. 283–285, 1989.

[115] P. R. M. Nahum, S. Verghese and K. Char, "Thermal boundary resistance for $YBa_2Cu_3O_{7-x}$ films," *Applied Physics Letters*, vol. 59, no. 16, pp. 2034–2036, Oct 1991.

[116] R. F. Voss and J. Clarke, "Flicker 1/f noise: Equilibrium temperature and resistance fluctuations," *Physical Review B*, vol. 13, pp. 556–573, Jan 1976.

[117] J. A. Greer, "High quality ybco films grown over large areas by pulsed laser deposition," *Journal of Vacuum Science & Technology A*, vol. 10, no. 4, pp. 1821–1826, 1992.

[118] C. Marshall, A. Tokmakoff, I. Fishman, C. B. Eom, J. Phillips, and M. Fayer, "Thermal boundary resistance and diffusivity measurements on thin $YBa_2Cu_3O_{7-x}$ films with MgO and $SrTiO_3$ substrates using the transient grating method," *Journal of Applied Physics*, vol. 73, no. 2, pp. 850–857, Jan 1993.

[119] P. Langlois, D. Robbes, M. L. C. Sing, C. Gunther, D. Bloyet, J. F.Hamet, R. Desfeux, and H.Murray, "Superconducting fast microbolometers operating below their critical temperature," *Journal of Applied Physics*, vol. 76, no. 6, pp. 3858–3868, 1994.

[120] O. Harnack, K. S. Il'in, M. Siegel, B. S. Karasik, W. R. McGrath, and G. de Lange, "Dynamics of the response to microwave radiation in yba2cu3o7-x hot-electron bolometer mixers," *Applied Physics Letters*, vol. 79, no. 12, pp. 1906–1908, 2001.